# Malaria parasite heme biosynthesis promotes and griseofulvin protects against cerebral malaria in mice

Manjunatha Chandana[1,2,5], Aditya Anand[1,3,5], Sourav Ghosh[1,3,5], Rahul Das [1,3], Subhashree Beura[1], Sarita Jena[1], Amol Ratnakar Suryawanshi[1], Govindarajan Padmanaban[4] & Viswanathan Arun Nagaraj [1✉]

Heme-biosynthetic pathway of malaria parasite is dispensable for asexual stages, but essential for mosquito and liver stages. Despite having backup mechanisms to acquire hemoglobin-heme, pathway intermediates and/or enzymes from the host, asexual parasites express heme pathway enzymes and synthesize heme. Here we show heme synthesized in asexual stages promotes cerebral pathogenesis by enhancing hemozoin formation. Hemozoin is a parasite molecule associated with inflammation, aberrant host-immune responses, disease severity and cerebral pathogenesis. The heme pathway knockout parasites synthesize less hemozoin, and mice infected with knockout parasites are protected from cerebral malaria and death due to anemia is delayed. Biosynthetic heme regulates food vacuole integrity and the food vacuoles from knockout parasites are compromised in pH, lipid unsaturation and proteins, essential for hemozoin formation. Targeting parasite heme synthesis by griseofulvin —a FDA-approved antifungal drug, prevents cerebral malaria in mice and provides an adjunct therapeutic option for cerebral and severe malaria.

[1] Infectious Disease Biology, Institute of Life Sciences, Bhubaneswar 751023 Odisha, India. [2] School of Biotechnology, Kalinga Institute of Industrial Technology, Bhubaneswar 751024 Odisha, India. [3] Regional Centre for Biotechnology, Faridabad 121001 Haryana, India. [4] Department of Biochemistry, Indian Institute of Science, Bangalore 560012 Karnataka, India. [5] These authors contributed equally: Manjunatha Chandana, Aditya Anand, Sourav Ghosh. ✉email: arun@ils.res.in

Malaria remains a major concern of morbidity and mortality, especially with the emerging parasite resistance to artemisinin-based combination therapies (ACTs) and mosquito resistance to insecticides[1]. According to World Health Organization (WHO), 241 million cases and 627,000 malaria deaths occurred in 2020[1]. Of the five *Plasmodium* species causing human malaria, *Plasmodium falciparum* (*Pf*) is the deadliest one responsible for more than 90% of the infections. The clinical manifestations of *Pf* malaria vary from mild (uncomplicated malaria) to severe (complicated malaria). Uncomplicated malaria is characterized by fever, headache, nausea, chills and mild anemia. Complicated malaria is categorized by the existence of at least one criterion of disease severity that includes respiratory distress, metabolic acidosis, pulmonary edema, severe anemia, jaundice, renal failure or neurological complications like impaired consciousness, convulsions etc. The typical outcome of severe malaria is multi-organ failure and/or cerebral malaria (CM) of which, CM is the most severe neurological complication with high mortality. About one-third of the patients recovering from CM show long-term neurocognitive impairments[2–4].

Our current understanding on CM comes from a few post-mortem studies of human CM (HCM) and a large number of experimental CM (ECM) studies performed in mouse models[5,6]. Although rodent parasites lack orthologs for *Pf* erythrocyte membrane protein 1 - a protein family that is transported to RBC membrane and primarily associated with parasite sequestration, the molecular mechanisms and cellular machinery underlying cerebral pathogenesis and parasite virulence are conserved[7]. There were earlier discrepancies on the extent of using ECM as a model for HCM, especially in the context of the sequestration of parasitized RBCs (pRBCs) in brain microvasculature. HCM is characterized by strong cytoadherence and dense sequestration of large numbers of pRBCs that can obstruct substantial lengths of cerebral microvasculature[8], in contrast to irregular distribution of pRBCs in ECM that seem to be mechanically trapped[9,10]. However, several studies have suggested significant analogies between HCM and ECM in terms of cerebral and neurovascular pathology. There is a consensus on increased permeability of blood-brain barrier (BBB), brain capillary occlusions, parasitized-red blood cells (pRBCs) accumulation in brain microvasculature, leukocyte infiltration, and endothelial activation with dysregulated inflammation and aberrant host-immune responses. All these lead to BBB disruption, intracerebral hemorrhages, ischemia, edema, increased intracranial pressure, axonal damage and demyelination, culminating in the dysfunction of central nervous system[5,6,11].

Cerebral pathology arises due to a complex interplay of molecular events triggered by various host- and parasite-derived factors. The synchronous growth of the asexual parasites in red blood cells (RBCs) and the associated schizogony result in the release of pathogen-associated molecular patterns (PAMPs) such as hemozoin (Hz), glycosylphosphatidylinositiol, parasite DNA and RNA, and danger-associated molecular patterns (DAMPs) such as heme, uric acid, and extracellular vesicles[12,13]. Hz and its precursor heme play a central role in CM pathogenesis[14–21]. The asexual stage parasites endocytose host hemoglobin (Hb) and digest it in the food vacuole (FV). The toxic free heme released during this process is detoxified into Hz by heme detoxification protein (HDP) that undergoes a circuitous trafficking and abundantly present in the infected RBC cytosol than parasite FVs[22]. Although the rate of HDP-mediated Hz formation is much higher, autocatalytic[23], histidine rich protein (HRP)-mediated[24] and lipid-driven mechanisms[25,26] for Hz formation have also been described. There is a positive correlation of Hz released into the circulation and phagocytosed by the circulating phagocytic cells with disease severity in children and adults[27–29]. Similarly,

plasma free heme is associated with disease severity[30,31]. Free heme is cytotoxic to endothelial cells and it can increase the expression of adhesion molecules, induce NLRP3 inflammasome and IL-1β secretion, and activate polymorphonuclear cells. The only treatment option for CM is parenteral administration of artemisinin derivatives or quinine with supportive therapies. However, the fatality due to CM remains high despite the parasite clearance[2–4,32]. The molecular mechanisms underlying CM pathogenesis need to be understood for developing adjunct therapies.

Malaria parasite synthesizes heme de novo despite the ability of asexual stages to access host Hb-heme[33]. The parasite heme pathway is compartmentalized in mitochondrion, apicoplast and cytosol, and heme is eventually synthesized in the mitochondrion. Our earlier study with *P. berghei* (*Pb*) aminolevulinate synthetase (ALAS) and ferrochelatase (FC) knockouts (KOs) generated for the first and last enzymes, demonstrated that the parasite pathway is dispensable for growth in asexual stages, but essential for the development of sporozoites in mosquitoes and pre-erythrocytic stages in liver. Moreover, FCKO parasites can utilize host Hb-heme for their survival in blood stages[34,35]. Subsequent studies in *Pf* using the KO parasites generated for ALAS, FC, apicoplast-localized porphobilinogen deaminase and cytosol-localized coproporphyrinogen oxidase, confirmed these findings with the suggestion that extracellular ALA acquired through new permeability pathways may also lead to parasite heme synthesis[36,37]. The conversion of extracellular ALA into protoporphyrin IX occurs in RBCs with the help of host enzymes, and heme is synthesized by parasite FC. Although de novo heme synthesis is non-essential and the asexual KO parasites can acquire heme/heme precursors from host RBCs and import some of the host enzymes, the parasite enzymes are expressed and heme synthesis occurs as evident from $^{13}C/^{14}C$-ALA metabolic labeling studies[34–41]. We hypothesized that the parasite de novo heme pathway should have a physiological relevance in the asexual stages. Here, we show that de novo heme induces ECM pathogenesis by regulating Hz formation in the asexual stages, thus offering an answer to a long-standing question. We further provide an adjunct therapeutic option on the basis that griseofulvin - a well-known FDA-approved drug capable of inhibiting parasite heme synthesis, can prevent ECM in mice.

Results

Heme pathway KO parasite-infected mice are protected from ECM. Our earlier work with *Pb* heme pathway KO parasites was carried out in outbred Swiss mice that do not develop ECM[34]. Here, we performed our studies in ECM-susceptible C57BL/6 inbred mouse strain by injecting 10^5 asexual stage parasites. Assessment of the peripheral blood parasitemia showed 2–3 days delay in the growth of KO parasites with respect to the WT (Fig. 1a). Importantly, about 80% of the WT-infected mice succumbed to ECM within day 10 when the blood parasitemia was around 10–30%. The WT-infected mice that escaped from ECM died of anemia on day 12–16 post-infection. In contrast, mice infected with ALASKO and FCKO parasites were protected from ECM and they died because of anemia on day 20–30 (Fig. 1b). The delay in the growth of KO parasites was associated with an early increase in the spleen weight of infected mice (Fig. 1c), suggesting a better splenic clearance. A similar delay in the growth of KO parasites and the mortality of KO-infected mice due to anemia was observed in Balb/c mice that do not develop ECM (Supplementary Fig. 1a, b). It is known that the growth of heme pathway KO parasites differs slightly with respect to the genetic background of mouse (inbred/outbred) and a similar delay in growth is also reported for other heme pathway KO
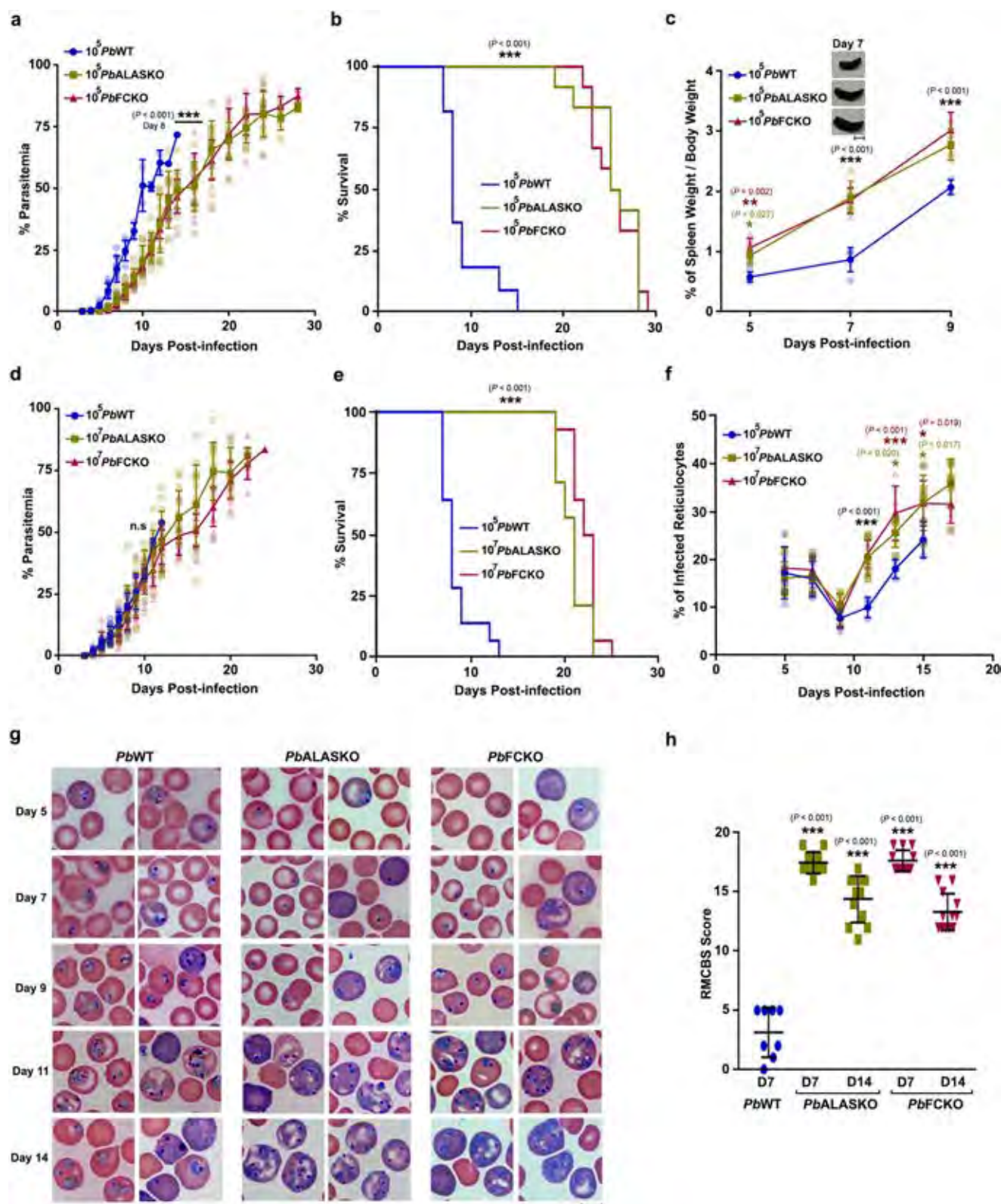
parasites[34,42,43]. To rule out the possibility that ECM protection is because of a delay in the increase in blood parasitemia, we performed growth analyses in C57BL/6 mice infected with 10^7 ALASKO/FCKO parasites. While the growth of 10^7 KO parasites in mice was comparable with 10^5 WT parasites, KO-infected mice were once again protected from ECM (Fig. 1d, e). The mortality due to anemia was delayed by 6–10 days, and KO-infected mice could sustain a higher parasitemia for a prolonged period. There were no significant differences in the reticulocyte versus mature RBC preference between WT and KO parasites in the first 9 days, the duration in which ECM mortality occurred in WT-infected mice. However, KO parasites showed significantly increased reticulocyte preference and multiple infections in the reticulocytes during the later course of infections that represent anemic phase

Fig. 1 CM protection in heme pathway KO parasite-infected mice. a Growth analysis of PbWT ($n = 10$), PbALASKO ($n = 12$) and PbFCKO ($n = 12$) parasites in C57BL/6 mice. 10^5 parasites were used to initiate PbWT and PbKO parasite infections. The data represent three different batches. (mean ± SD; ***$P < 0.001$, Two-way ANOVA). **b** Mortality curves of mice infected with PbWT, PbALASKO and PbFCKO parasites. The data represent the mice utilized for growth curve analysis (***$P < 0.001$, log-rank (Mantel–Cox) test). **c** Spleen weight of mice infected with PbWT ($n = 13$), PbALASKO ($n = 14$) and PbFCKO ($n = 14$) parasites. For each day, 3–5 mice from at least three different batches were included (mean ± SD; *$P < 0.05$, **$P < 0.01$, ***$P < 0.001$, Two-way ANOVA). Scale bar = 1 cm. **d** Growth analysis of PbWT ($n = 14$), PbALASKO ($n = 14$) and PbFCKO ($n = 14$) parasites in C57BL/6 mice. 10^5 and 10^7 parasites were used to initiate WT and KO parasite infections, respectively. The data represent four different batches (mean ± SD; n.s. not significant, Two-way ANOVA). **e** Mortality curves of mice infected with PbWT, PbALASKO and PbFCKO parasites. The data represent the mice utilized for growth curve analysis (***$P < 0.001$, log-rank (Mantel–Cox) test). **f** Percentage of infected reticulocytes in the parasitized red cells (mean ± SD; *$P < 0.05$, ***$P < 0.001$, Two-way ANOVA). The data represent six mice each for PbWT, PbALASKO and PbFCKO parasites. **g** Giemsa-stained images for peripheral blood smears prepared from tail vein blood of PbWT and PbKO parasite-infected mice. Reticulocytes could be identified by their distinct blue color. Images were captured using 100x objective. Scale bar = 5 µm. $n = 4$–6 independent experiments. **h** RMCBS score for mice infected with PbWT ($n = 8$) and PbKO ($n = 12$) parasites. PbWT data represent the mice that succumbed to ECM (mean ± SD; ***$P < 0.001$, unpaired t-test; two-sided). For (**a**, **c**, **d**, **f**), individual data points are shown with the respective light shaded colors. Source data are provided as a Source Data file.

(Fig. 1f, g). The rapid murine coma and behavioral scale (RMCBS) score of 10^5 WT parasite-infected mice that succumbed to ECM was below 5 on day 7 whereas, RMCBS score of 10^7 KO parasite-infected mice was around 17 and 14 on day 7 and 14, respectively (Fig. 1h). For all the subsequent experiments, we initiated asexual infections by injecting 10^5 WT and 10^7 ALASKO/FCKO parasites.

These results were verified with another set of independent PbKO^{Luc} parasite lines wherein, $ALAS$ and FC genes were replaced individually with GFP-luciferase (Luc)-expressing cassette containing m-cherry (Fig. 2a). The successful replacement of $ALAS$ and FC was confirmed by PCR analyses performed with DNA and RNA isolated from the respective PbKO^{Luc} parasites (Fig. 2b, c), and by examining GFP and m-cherry fluorescence (Fig. 2d). For control, c-$ssurRNA$ locus in the WT parasite was replaced with GFP-Luc-expressing cassette containing m-cherry (PbControl^{Luc}). The site-specific integrations in PbControl^{Luc} and PbKO^{Luc} parasites were also confirmed by PCR analyses (Supplementary Fig. 1c–e). In vivo bioluminescence studies showed accumulation of pRBCs in the brain of PbControl^{Luc}-infected mice, but not in the PbKO^{Luc}-infected mice (Fig. 2e) and this was confirmed by ex vivo imaging as well (Fig. 2f). The mice infected with PbKO^{Luc} parasites were protected from ECM (Fig. 2g). To rule out any off-target effect, we performed genetic complementation in PbFCKO^{Luc} by reintroducing FC (PbFCKO^{+FC}) expressed under its native promoter through stable integration (Supplementary Fig. 1f). The successful complementation of FC was verified by PCR and Western analyses (Supplementary Fig. 1g–i). PbFCKO^{+FC} parasites behaved like WT parasites and caused ECM in the infected mice (Fig. 2h–j). These data suggested that the mice infected with heme pathway KO parasites are protected from ECM.

Absence of ECM pathology in heme pathway KO parasite-infected mice. To evaluate the integrity of BBB and assess vascular leakage, Evans blue extravasation analyses were carried out. While the brain collected from WT-infected mice on day 7/8 stained intensely with Evans blue, the extravasation of Evans blue into the brain was barely detectable in KO-infected mice on day 7 and 14 (Fig. 3a). Quantification of Evans blue in the brain extracts confirmed this observation (Fig. 3b). Histopathological assessment of hematoxylin and eosin (H&E)-stained brain sections of WT-infected mice on day 7 showed intracerebral hemorrhages with extravasation of erythrocytes into the perivascular space, petechial hemorrhages, thrombosed and leukocyte-packed vessels, gross demyelination and myelin pallor. No such hallmark features of ECM could be detected in the brain sections of KO-infected mice (Fig. 3c). Immunohistochemical studies performed with the brain sections of WT-infected mice showed the extravasation of IgG in cerebral parenchyma and the presence of IgG in occluded vessels and hemorrhages, but not in

the KO-infected mice (Fig. 3d). Luminal and abluminal leukocytes, and parasite-derived Hz could be detected in the occluded vasculature of WT-infected mice. (Fig. 3e). Immunofluorescence analyses of the brain sections using Pb glyceraldehyde-3-phosphate dehydrogenase (GAPDH) and mouse CD31 antibodies showed the accumulation of parasites in CD31$^+$ vasculature and extravascular parasites in the hemorrhages of WT-infected mice, but not in the KO-infected mice (Fig. 3f). Similarly, antibodies specific for CD3 and β-amyloid precursor protein (β-APP) showed the accumulation of CD3$^+$ T cells in the cerebral vasculature (Fig. 3g) and axonal injury in the brain sections of WT-infected mice, but not in the KO-infected mice (Fig. 3h). These data suggested the absence of ECM-associated brain lesions in mice infected with heme pathway KO parasites.

Inflammatory parameters in heme pathway KO parasite-infected mice. Multiplex assays performed for mice infected with KO parasites on day 8 showed a significant decrease in the plasma levels of proinflammatory cytokines and chemokines—IL-6, TNFα, IFNγ, G-CSF, CCL3 (MIP-1α) and CCL5 (RANTES). There was also a significant increase in anti-inflammatory cytokines—IL-4, IL-10 and IL-13 (Fig. 4a). Quantitative RT-PCR analyses examining the expression of cytokines, chemokines, chemokine receptors and other key mediators of cerebral pathogenesis in the brain samples of KO-infected mice showed a substantial reduction of >1.5 fold in the transcript levels of TNFα, IFNγ, CXCL9, CXCL10, CCL2 (MCP-1), CCL5, CCL19, perforin, granzyme B, ICAM-1, p-selectin and HO-1. In particular, the decrease in IFNγ, CXCL10, CCL2, CCL5, granzyme B, ICAM-1 and HO-1 in FCKO was greater than 3-fold (Fig. 4b). Flow cytometry analyses of the leukocytes isolated from the brain samples of KO-infected mice showed significant reduction in CD3$^+$ CD4$^+$ and CD3$^+$ CD8$^+$ double positive T cells, and CD3$^+$ CD8$^+$ CD69$^+$, CD3$^+$ CD8$^+$ CXCR3$^+$, CD3$^+$ CD8$^+$ perforin$^+$, CD3$^+$ CD8$^+$ granzyme B$^+$, CD3$^+$ CD8$^+$ TNFα$^+$ and CD3$^+$ CD8$^+$ IFNγ$^+$ triple positive T cells (Fig. 4c and Supplementary Fig. 2). Western analyses for the brain homogenates of KO-infected mice showed reduction in phospho-NLRP3, phospho-NF-κB, cleaved caspase-1 and IL-1β (Fig. 4d). RNA levels of schizont membrane-associated cytoadherence protein (SMAC), skeleton-binding protein 1 (SBP1) and membrane-associated histidine-rich protein-1a (MAHRP1a) mediating sequestration and cytoadherence in Pb were comparable between WT and FCKO parasites (Supplementary Fig. 3a). Further, there was no significant difference between the in vitro cytoadherence of PbControl^{Luc}- and PbFCKO^{Luc}-pRBCs to TNFα-prestimulated mouse brain endothelial cells (Supplementary Fig. 3b, c). These data suggested that although the parasite machinery underlying cytoadherence is retained, mice infected with heme pathway KO
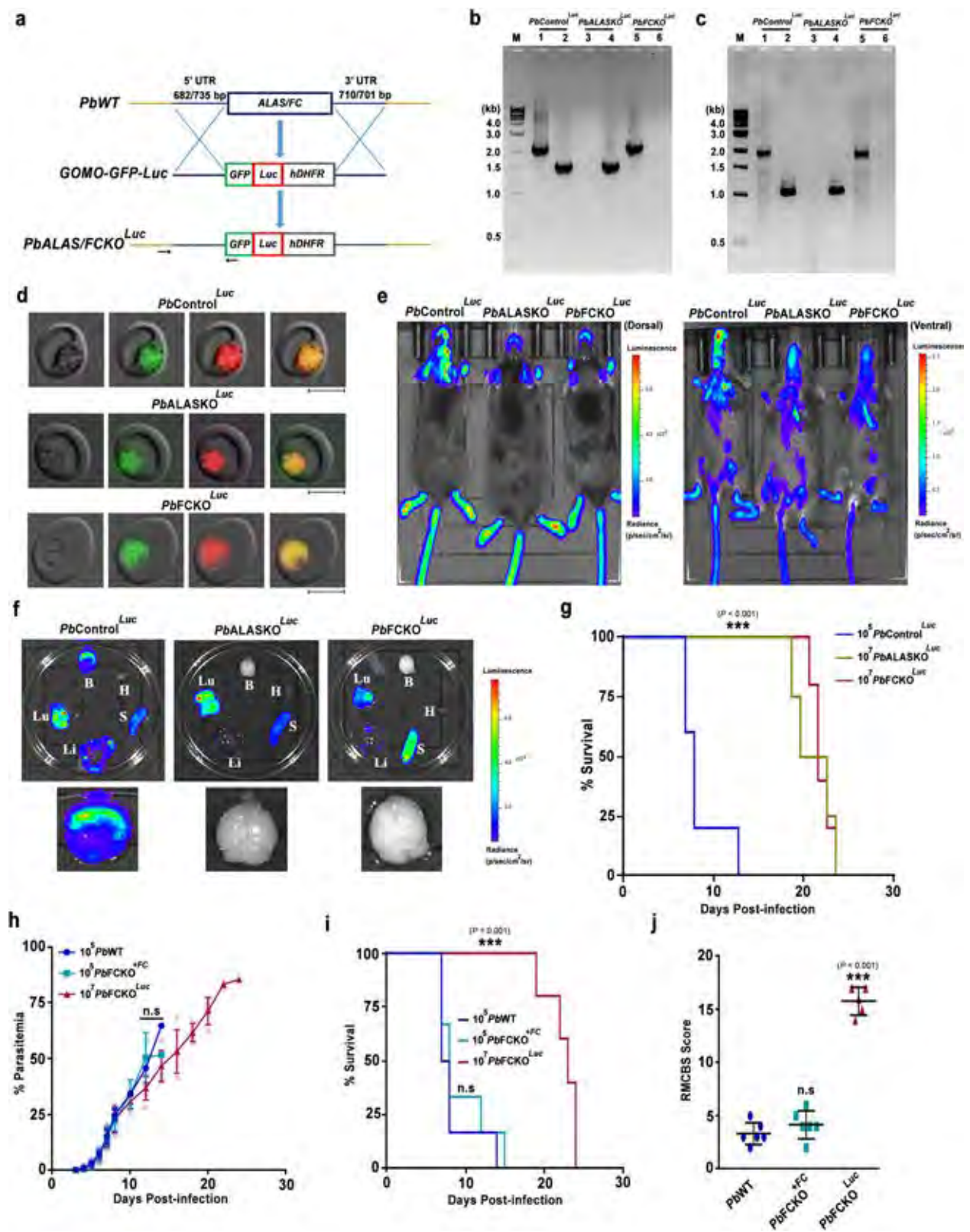
parasites show reduced in vivo sequestration due to an overall decrease in systemic and neuronal inflammation and T cell infiltration in the brain milieu.

Decreased Hz formation in heme pathway KO parasites. A substantial decrease in Hz formation was observed in the Giemsa-stained peripheral blood smears of KO parasites. This was more prominent in the asexual stages (Fig. 5a) than gametocytes (Fig. 5b), and could be readily detected in almost 60–70% of the pRBCs containing asexual stages. These findings were verified by examining Hz content in paraformaldehyde-fixed pRBCs (Fig. 5c) and Hz dynamics in live pRBCs (Supplementary Movie 1, Supplementary Movie 2 and Supplementary Movie 3). To confirm,

Fig. 2 Generation of Luc-expressing heme pathway KO parasites, in vivo bioluminescence imaging of infected mice and genetic complementation.
a Double-crossover recombination strategy to generate Luc-expressing PbALASKO (PbALASKO^{Luc}) and PbFCKO (PbFCKO^{Luc}) parasites. Black arrows represent the position of primers used for the confirmation of site-specific integration in PbKO^{Luc} parasites (data provided in Supplementary Fig. 1).
b Genomic DNA PCR confirmation for ALAS and FC deletions in PbALASKO^{Luc} and PbFCKO^{Luc} parasites, respectively. Lane M: 1 kb ladder; Lane 1, 3 and 5: ALAS product (2.11 kb); Lane 2, 4 and 6: FC product (1.54 kb). $n = 3$ independent experiments. **c** RT-PCR confirmation for ALAS and FC deletions. Lane M: 1 kb ladder; Lane 1, 3 and 5: ALAS product (1.92 kb); Lane 2, 4 and 6: FC product (1.05 kb). $n = 3$ independent experiments. **d** Live GFP and m-cherry fluorescence of PbControl^{Luc} and PbKO^{Luc} parasites. Images were captured using 100x objective. Scale bar = 5 μm. $n = 4$ independent experiments.
e Whole body bioluminescence imaging of PbControl^{Luc} and PbKO^{Luc} parasite-infected mice on day 8 post-infection. $n = 3$ independent experiments. **f** Ex vivo bioluminescence imaging of liver (Li), lungs (Lu), brain (B), heart (H) and spleen (S) of PbControl^{Luc}- and PbKO^{Luc}-infected mice. Enlarged images of brain are shown. **g** Mortality curves of mice infected with PbControl^{Luc} ($n = 5$), PbALASKO^{Luc} ($n = 4$) and PbFCKO^{Luc} ($n = 5$) parasites (***$P < 0.001$, log-rank (Mantel–Cox) test). **h** Growth analysis of PbWT ($n = 6$), PbFCKO^{+FC} ($n = 6$) and PbFCKO^{Luc} ($n = 5$) parasites in C57BL/6 female mice. The data represent two different batches (mean ± SD; n.s not significant, Two-way ANOVA). Individual data points are shown with the respective light shaded colors. **i** Mortality curves of mice infected with PbWT ($n = 6$), PbFCKO^{+FC} ($n = 6$) and PbFCKO^{Luc} ($n = 5$) parasites (n.s not significant, ***$P < 0.001$, log-rank (Mantel–Cox) test). **j** RMCBS score for mice infected with PbWT ($n = 6$), PbFCKO^{+FC} ($n = 6$) and PbFCKO^{Luc} ($n = 5$) parasites on day 7/8 post-infection. PbWT and PbFCKO^{+FC} data represent the mice succumbed to ECM (mean ± SD; n.s - not significant, ***$P < 0.001$, unpaired t-test; two-sided). Source data are provided as a Source Data file.

total Hz content of the KO parasites normalized with respect to the protein was examined and it was 20–25% of the WT (Fig. 5d). During Hz formation in the FV, heme can leach into the parasite cytosol. Free heme in the parasite lysates of the KO parasites prepared by hypotonic lysis showed around 55% decrease when compared with WT (Fig. 5e). In addition, there was a significant decrease of around 55–60% in the plasma free heme and heme/hemopexin ratio of the KO-infected mice (Fig. 5f, g). However, there were no significant differences between the plasma hemopexin levels of WT- and KO-infected mice (Fig. 5h), and there was 15–20% decrease in the plasma Hb levels that was statistically significant in case of FCKO, but not in ALASKO (Fig. 5i). The quantification of Hz load in the spleen and liver showed 40–50% decrease in the KO-infected mice (Fig. 5j, k). A similar decrease in the Hz content and free heme was observed for the KO parasites isolated from Balb/c mice (Supplementary Fig. 3d, e). These results suggested an overall decrease in the Hz synthesis of KO parasites. This was further verified by the restoration of Hz and free heme levels in PbFCKO^{+FC} parasites isolated from C57BL/6 mice (Supplementary Fig. 3 f–h) and the presence of cerebral pathogenesis in the PbFCKO^{+FC}-infected mice (Supplementary Fig. 3i–k).

Heme and Hz are associated with the function of antimalarial drugs—artemisinin and chloroquine[44,45]. Therefore, we were interested in examining the effect of α,β-arteether (artemisinin derivative) and chloroquine on FCKO-infected C57BL/6 mice in vivo. For α,β-arteether treatment, a single intramuscular dose of 1 mg/mouse or 0.4 mg/mouse was administered on day 5 post-infection when the blood parasitemia was around 5%. For chloroquine treatment, a daily dose of 25 mg/kg or 10 mg/kg was administered intraperitoneally for five consecutive days from day 5 post-infection. While 1 mg of α,β-arteether could clear the WT and FCKO parasites, 50% recrudescence was observed for 0.4 mg dosage in the WT- and FCKO-infected mice. The day of recrudescence was comparable between WT and FCKO parasites and the parasites were detectable in peripheral smears prepared on day 12 post-infection. However, the growth of FCKO parasites in mice showing recrudescence was delayed in the subsequent days and this was reflected in the mortality (Fig. 6a, b). The assessment of parasite load at the time of recrudescence on day 12 using PbGAPDH primers showed that C_t values normalized against mouse GAPDH for FCKO-infected mice were ~1.5 cycles more than WT-infected mice (Supplementary Fig. 4a–d), suggesting 3-fold less parasite load in FCKO-infected mice. In case of chloroquine, recrudescence was observed for WT and FCKO parasites with both the doses that were tested and importantly, FCKO parasites appeared 2–4 days earlier than WT (Fig. 6c, d).

This was also confirmed by performing qPCR analysis on day 13 for 25 mg/kg and day 10 for 10 mg/kg doses. In both the cases, C_t values obtained for the parasite load in FCKO-infected mice were ~4 cycles lower than WT-infected mice, suggesting 16-fold higher parasite load in FCKO-infected mice (Supplementary Fig. 4e–h). Further, one out of four and two out of four WT-infected mice died of CM in 25 mg/kg and 10 mg/kg treatment, respectively. Despite showing an early recrudescence, all the FCKO-infected mice died of anemia and their mortality was delayed in comparison to WT-infected mice (Fig. 6d). These results suggested that chloroquine sensitivity is compromised in FCKO parasites as observed by the earlier recrudescence, while α,β-arteether sensitivity remains unaltered in vivo in mice.

De novo heme is essential for the functional integrity of FV. To understand the molecular mechanisms underlying decreased Hz synthesis, we assessed pH, lipids and protein content of the FVs in FCKO parasites and compared with WT parasites. Live fluorescence imaging of pRBCs incubated with acidophilic dye LysoTracker Deep Red indicated less fluorescence in the FCKO parasites (Fig. 7a), suggesting that the pH of FCKO FV is compromised. The quantification of fluorescence signal intensities showed ~50% decrease (Fig. 7b). We examined the phospholipid content and could not find significant differences for in vitro ^{32}P-orthophosphoric acid radiolabelling of major phospholipids - phosphatidylcholine (PC), phosphatidylinositol (PI) and phosphatidylethanolamine (PE), in the total parasites and FVs of FCKO parasites (Fig. 7c, d and Supplementary Fig. 5a). Similarly, the assessment of neutral lipid content by live fluorescence imaging of pRBCs stained with BODIPY 493/503 and Nile Red did not show significant differences (Fig. 7e–h). Lipids associated with parasite Hz are reported to be abundant in monohydroxy derivatives of polyenoic fatty acids, and unsaturated glycerophospholipids induce rapid and efficient Hz formation in hematophagous insect $Rhodnius$ $prolixus$[46,47]. GC-MS analysis of fatty acid methyl esters (FAMEs) prepared from the FVs of Pb parasites indicated the presence of oleic acid (OA) as a major unsaturated fatty acid followed by arachidonic acid along with other saturated fatty acids, fatty acyl alcohols and derivatives, alkanes, etc. (Supplementary Fig. 5b and Supplementary Table 1). Malaria parasite scavenges stearic acid (SA) from plasma and converts it into OA by ER-localized Δ9-desaturase (stearoyl-CoA 9-desaturase). The cis double bond formation in OA requires heme since it utilizes the electrons transferred by cytochrome b5 from NADH cytochrome b5 reductase[48,49]. We performed in vitro ^{14}C-SA radiolabelling to assess OA synthesized by the
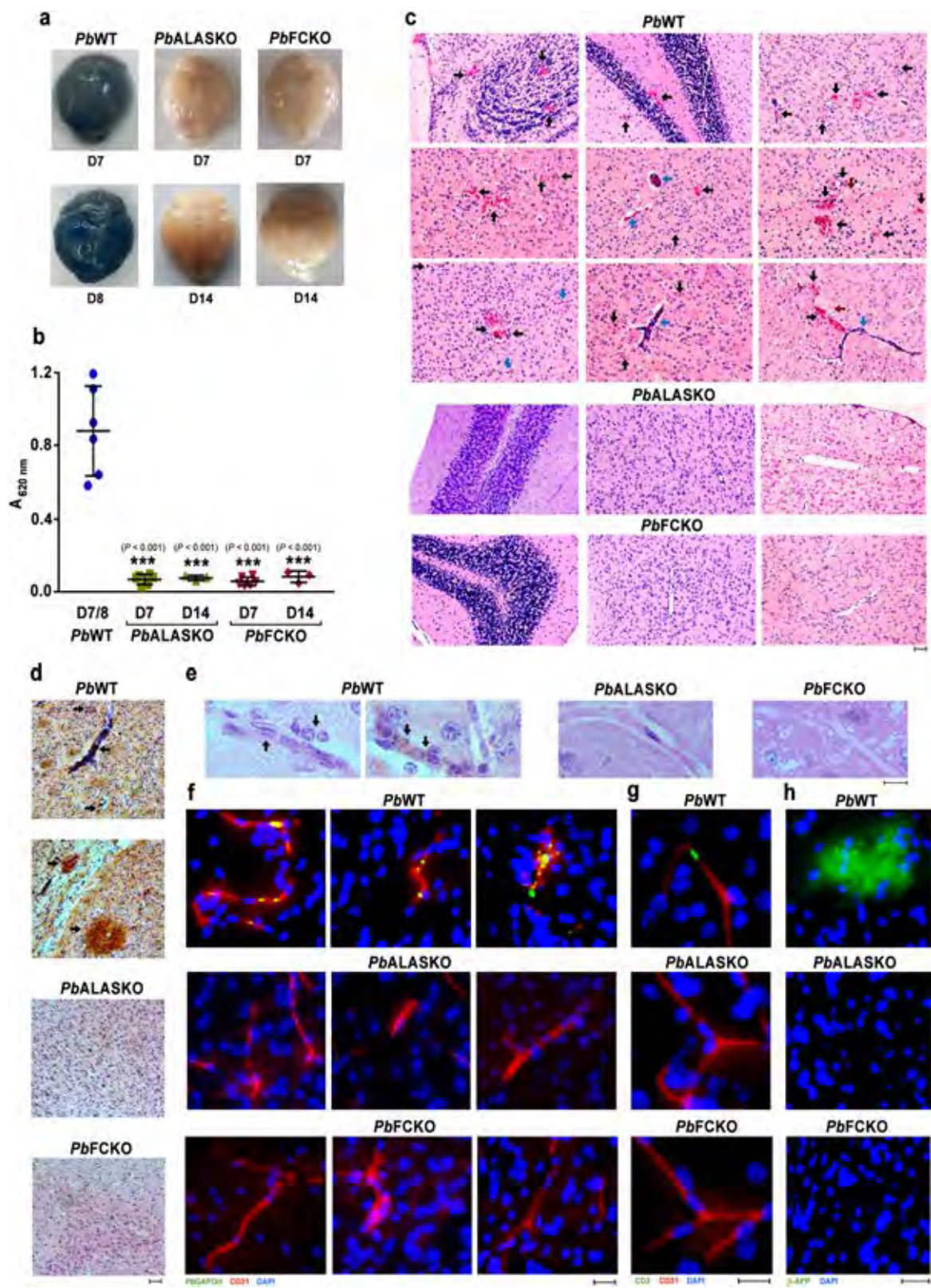
parasite. The separation of unsaturated FAMEs prepared from FCKO total parasites and FVs showed almost 80–90% decrease in the radiolabelling of OA methyl ester (OAME) in comparison to WT (Fig. 8a–c), with no significant differences in the signal intensities of SA methyl ester (SAME). The identity of the slower migrating polyunsaturated FAME (PU-FAME) that also showed a significant decrease in FVs is yet to be established and there are

no clear-cut evidences for the presence of other desaturases in the parasite. There was a significant ~50% decrease in the ^{14}C-SA radiolabelling of FCKO FVs, but not in the total parasites (Supplementary Fig. 5c).

FV proteomics is challenging due to the presence of large amounts of host Hb, Hb degradation peptides and indigenous proteases. To the best of our knowledge, there is only one report on

Fig. 3 Assessment of cerebral pathology in heme pathway KO parasite-infected mice. a Evans blue extravasation in the brain of mice infected with *Pb*WT and heme pathway *Pb*KO parasites. **b** Quantification of Evans blue in the brain samples of mice infected with *Pb*WT ($n = 6$) and heme pathway *Pb*KO ($n = 9$) parasites. (mean ± SD; ***$P < 0.001$, unpaired *t*-test; two-sided). **c** H&E staining of the brain sections prepared from *Pb*WT and *Pb*KO parasite-infected mice. Black arrows—intracerebral and petechial hemorrhages, blue arrows—thrombosed blood vessels and brown arrows—gross demyelination. Images were captured using 10x objective. Scale bar = 50 μm. $n = 3$–5 independent experiments. **d** IgG extravasation in the brain sections of *Pb*WT and *Pb*KO parasite-infected mice. Black arrows—areas showing IgG immunoreactivity. Images were captured using 10x objective. Scale bar = 50 μm. $n = 3$ independent experiments. **e** H&E staining of the brain sections indicating (black arrows) occluded vasculatures containing luminal and abluminal leukocytes, and parasite-derived Hz. Images were captured using 60x objective. Scale bar = 10 μm. $n = 3$ independent experiments. **f** Immunofluorescence analysis of parasite accumulation in the brain sections of *Pb*WT and *Pb*KO parasite-infected mice. $n = 3$ independent experiments. **g** Immunofluorescence analysis of CD3$^+$ cells in the blood vessels of *Pb*WT and *Pb*KO parasite-infected mice. $n = 2$ independent experiments. **h** Immunofluorescence analysis of β-APP staining in the brain sections of *Pb*WT and *Pb*KO parasite-infected mice. $n = 2$ independent experiments. **f**–**h** Images were captured using 20x objective. Scale bar = 20 μm. Source data are provided as a Source Data file.

Pf FV proteomics based on LC-MS/MS analysis of proteins excised from SDS-PAGE gel that identified 116 proteins excluding elongation factors and ribosomal proteins[50]. Our repeated attempts to perform differential proteomics for WT and FCKO FVs by Isobaric tags for relative and absolute quantitation (iTRAQ) were unsuccessful because of the interference from host Hb. LC-MS/MS of in-solution trypsin digested FV protein extracts solubilized with 6 M urea was successful. Around 68% of the proteins identified earlier in the total *Pf* FV proteome[50] were present in our FV preparations from *Pb*. The quality of FV preparations could be assessed by the presence of signature FV proteins such as plasmepsin IV, berghepain, aminopeptidases, subunits of vacuolar-type H$^+$ATPase (V-type H$^+$ ATPase), together with parasitophorous vacuolar (PV) proteins including exported protein 1 (Exp1), Exp2, early transcribed membrane protein, PV1, PV5 (lipocalin) etc., and Rab GTPases associated with cytostome-FV trafficking. A total number of 251 and 201 proteins could be identified for WT and FCKO FVs, respectively, and 175 proteins were common between them suggesting an overall consistency in the preparations (Fig. 8d). The peptide intensities and spectral counts were comparable between WT and FCKO FV preparations (Supplementary Fig. 6a, b). In agreement with the decreased uptake of LysoTracker Deep Red in FCKO pRBCs, none of the subunits of V-type H$^+$ATPase—a proton pump maintaining the acidic pH of FV[51] could be detected in FCKO FVs suggesting the lower abundance of these proteins. In WT FV preparations, A, B and G subunits of V-type H$^+$ATPase could be detected (Fig. 8e, Supplementary Data 1 and Supplementary Data 2). While plasmepsin IV, the only *Pb* aspartic protease involved in Hb degradation could be detected in WT and FCKO FVs, berghepain-2—a cysteine protease involved in Hb degradation[52,53] could not be detected in FCKO FVs (Supplementary Data 1 and Supplementary Data 2). qPCR analysis indicated that the RNA levels of these proteins are comparable between WT and FCKO parasites (Fig. 8f). However, Western analysis carried out for V-type H$^+$ATPase subunits B and G showed a significant decrease in FCKO FVs with not much change in the total parasites (Fig. 8g). The rest of the proteins unique for WT and FCKO FVs include proteasome subunits, ribosomal proteins, metabolic enzymes etc., (Supplementary Data 1 and Supplementary Data 2) that are not related to Hz formation and known to be present in FV preparations[50]. Further, in agreement with less Hz formation, FVs of FCKO parasites appeared paler in comparison to WT (Supplementary Fig. 6c). While iTRAQ experiments were unsuccessful in identifying the parasite FV proteins because of the interference from host Hb, they could be used to assess the host Hb accumulation in FCKO FVs. There was ~3–4 -fold increase in Hb α and β chains in FCKO FVs as quantified by iTRAQ (Supplementary Fig. 6d; Supplementary Data 3). Similar to the mutants of Hb proteolysis[52], translucent vesicles were also observed in the Giemsa-stained smears of FCKO parasites (Supplementary Fig. 6e). All these evidences suggested that the functional integrity of FCKO FVs is compromised in terms of

pH, lipid unsaturation and proteins that in turn can collectively lead to a decreased Hz formation.

Griseofulvin treatment protects mice from ECM. Griseofulvin, isolated from *Penicillium griseofulvum*, is a FDA-approved antifungal drug used to cure tinea infections. It interacts with fungal micro-tubules and disrupts spindle assembly leading to mitotic arrest. In humans, griseofulvin dosage is given to the extent of 1000 mg/day in adults and 10 mg/kg/day in children for several weeks[54–56]. It can also inhibit FC by generating N-methyl protoporphyrin IX (NMPP) through the action of cytochrome P450 enzymes[57]. It has already been shown that the malaria parasite can convert griseofulvin into NMPP[58]. Therefore, we evaluated the potential of griseofulvin in preventing ECM by treating WT-infected C57BL/6 mice from day 4 when the blood parasitemia was around 2%. A single dose of 2 mg/day (comparable with the dosage of humans) administered from day 4 and continued until day 8 showed the best protection. While ~80% of the control mice succumbed to ECM within day 10, >80% of the treated mice were protected from ECM. Similar protection was also observed for the mice treated with 1 mg dose, twice a day from day 4 to day 8 (Fig. 9a). There was also a significant delay in the mortality that occurred due to anemia. While the mortality in ECM-escaped control mice occurred within day 17, >80% of the treated mice could survive beyond day 20 with almost 50% of them surviving even beyond day 24. Interestingly, the growth curves of WT parasites in treated and untreated mice were very much comparable (Fig. 9b). We analyzed heme synthesis in griseofulvin-treated WT parasites by incubating the in vivo-treated pRBCs in vitro with ^{14}C-ALA (committed precursor of heme synthesis) for 9 h and there was around 60% decrease in the ^{14}C-labeling of free heme (Fig. 9c). Further, griseofulvin-treated mice showed less Evans blue extravasation in the brain (Fig. 9d), with the absence of intracerebral hemorrhages (Fig. 9e), lack of accumulation of parasites and CD3$^+$ T cells in the cerebral vasculature (Fig. 9f, g) and undetectable axonal injury (Fig. 9h). Giemsa-stained peripheral smears and paraformaldehyde-fixed pRBCs showed less Hz content (Fig. 9i, j). As observed for KO parasites, the total Hz content in the griseofulvin-treated parasites was around 50–60% less when compared with untreated parasites (Fig. 9k) and there was close to 60% decrease in the free heme levels (Fig. 9l). Further, the plasma levels of heme, hemopexin and Hb together with heme/hemopexin ratio of the griseofulvin-treated WT-infected mice were comparable with the KO-infected mice (Fig. 9m–p). These results suggested that griseofulvin can prevent ECM through inhibition of parasite heme synthesis.

Our next interest was to examine the potential of griseofulvin as an adjunct drug with α,β-arteether (primary artemisinin component of ACTs) in preventing ECM. The dose optimization studies performed with α,β-arteether suggested that a single intramuscular dose of 0.25 mg/mouse on day 6 when there was onset of neurological symptoms and blood parasitemia was around 10%, led to ECM in ~60–70% of WT-infected mice. ECM occurred despite the clearance of peripheral parasitemia as
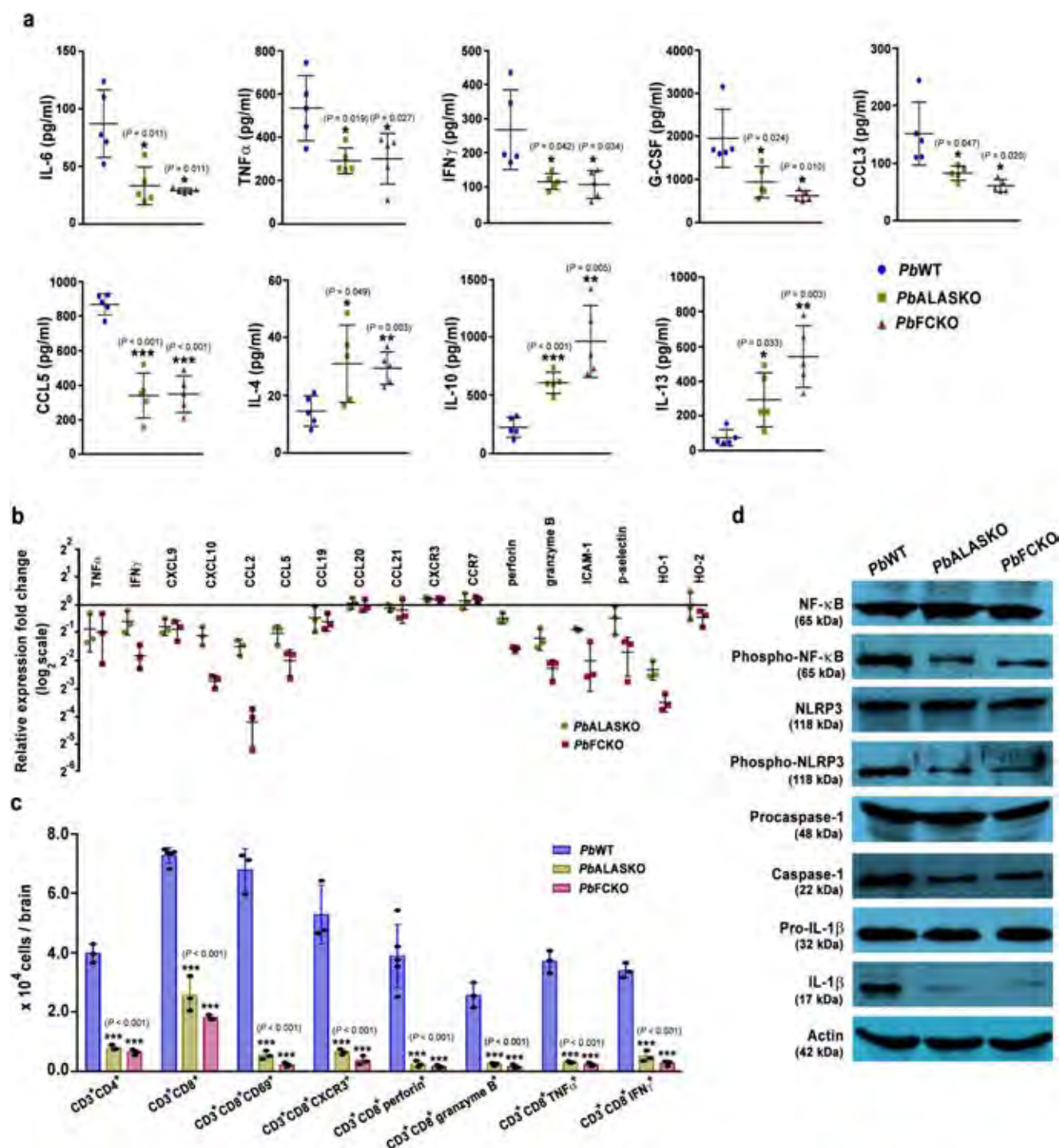
Fig. 4 Assessment of inflammatory parameters in heme pathway KO parasite-infected mice. a Plasma cytokine and chemokine levels of *Pb*WT- and *Pb*KO-infected mice ($n = 5$) (mean ± SD; *$P < 0.05$, **$P < 0.01$, ***$P < 0.001$, unpaired *t*-test; two-sided). **b** qPCR analyses of host transcripts in the brain samples of infected mice. Expression levels were normalized with mouse GAPDH. Relative expression fold changes of mRNA transcripts in the KO-infected mice with respect to WT-infected mice (mean ± SD) are shown ($n = 3$). **c** Flow cytometry analyses of T cells in the brain samples of infected mice. Mice on day 7/8 post-infection were used and the data for each cell type were obtained from at least three different mice infected with *Pb*WT or *Pb*KO parasites (mean ± SD; ***$P < 0.001$, Two-way ANOVA). Individual data points are shown as black circles. Gating strategy and representative flow cytometry plots are shown in the Supplementary Fig. 2. **d** Western analyses of brain homogenates prepared from *Pb*WT- and *Pb*KO-infected mice. 200 µg of total protein was used from the pooled brain homogenates of three different mice for *Pb*WT, *Pb*ALASKO and *Pb*FCKO. $n = 2$ independent experiments. Full-length blots are provided in the Supplementary Fig. 7. Source data are provided as a Source Data file.
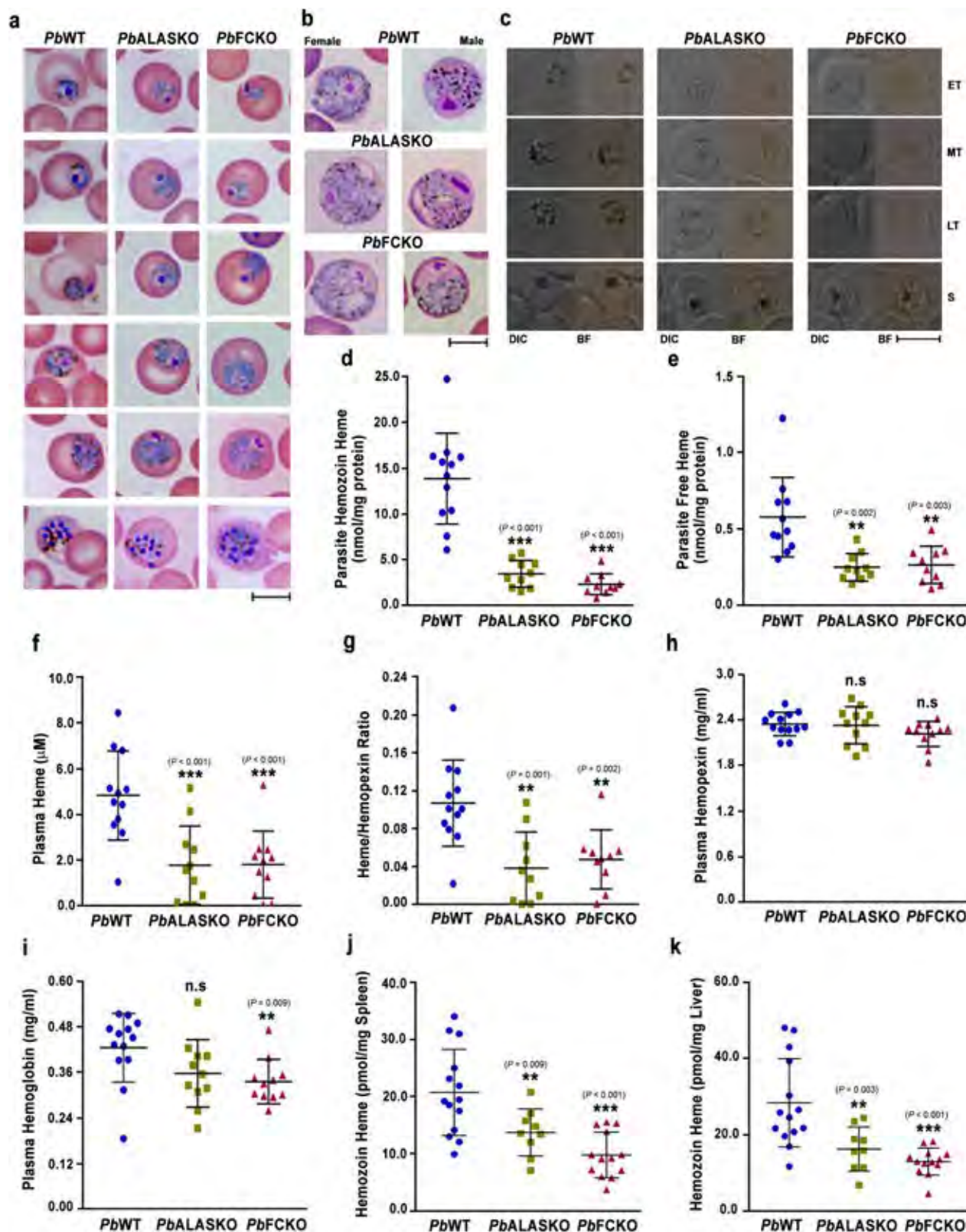
observed in the blood smears (Supplementary Fig. 6f, g). However, the inclusion of two doses of 2 mg griseofulvin at 24 h interval on day 6 and 7, post-α,β-arteether treatment, led to a complete protection of ECM (Fig. 9q). There were no significant differences in day 7 parasite load measured by qPCR analysis and in the mortality due to anemia caused by recrudescence for ECM-protected mice treated with the combination of α,β-arteether and griseofulvin in comparison with α,β-arteether alone (Supplementary Fig. 6h, Fig. 9q).

Griseofulvin treatment inhibits Hz formation in *Pf* parasites. To examine the relevance of our findings in human malaria parasite, we assessed the ability of griseofulvin to inhibit Hz

Fig. 5 Hz and heme levels in heme pathway KO parasites. a, b Bright field images of Giemsa-stained *Pb*WT, *Pb*ALASKO and *Pb*FCKO asexual stage parasites and gametocytes, respectively, showing Hz content. Images were captured using 100x objective. n = 3–5 independent experiments. Scale bar = 5 µm. **c** Hz content in differential interference contrast (DIC; left) and bright field images (right) of paraformaldehyde-fixed pRBCs containing *Pb*WT and *Pb*KO parasites. Images were captured using 100x objective. Scale bar = 5 µm. n = 3 independent experiments. **d** Hz levels in *Pb*WT (n = 12) and *Pb*KO (n = 10) parasites. **e** Free heme levels in *Pb*WT (n = 11) and *Pb*KO (n = 10) parasites. **f** Free heme levels in the plasma samples of *Pb*WT (n = 12) and *Pb*KO (n = 11) parasite-infected mice. **g** Heme/Hemopexin ratio in the plasma samples of *Pb*WT (n = 12) and *Pb*KO (n = 10) parasite-infected mice. **h** Plasma hemopexin levels of *Pb*WT (n = 13) and *Pb*KO (n = 11) parasite-infected mice. **i** Plasma hemoglobin levels of *Pb*WT (n = 13) and *Pb*KO (n = 11) parasite-infected mice. **j, k** Hz load in the spleen and liver of *Pb*WT (n = 14) and *Pb*KO (n = 9 for ALASKO; n = 13 for FCKO) parasite-infected mice, respectively. **d–k** The data represent mean ± SD (n.s not significant, **P < 0.01, ***P < 0.001, unpaired *t*-test; two-sided). Source data are provided as a Source Data file.
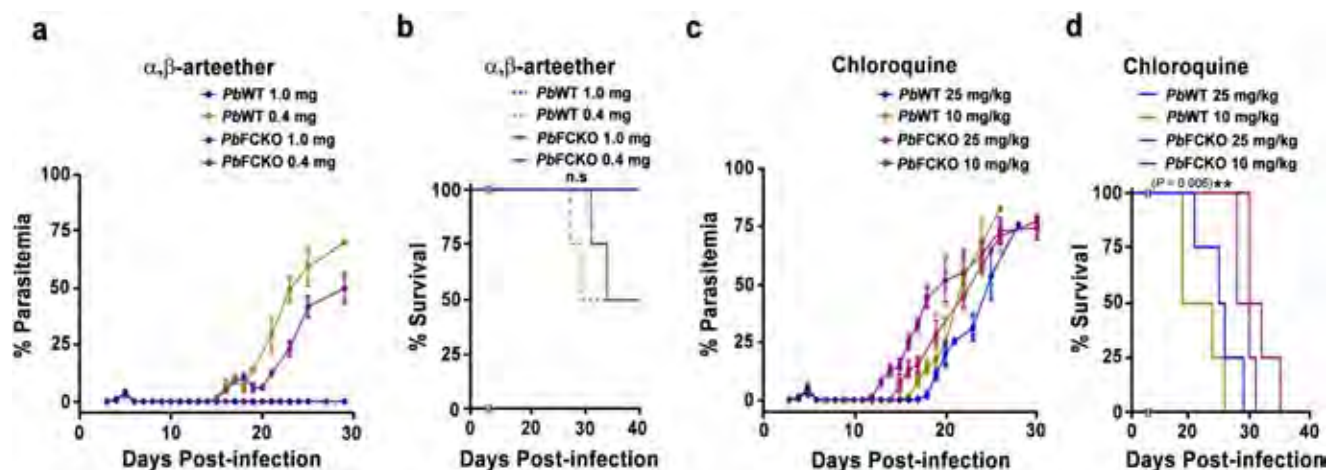
Fig. 6 Sensitivity of WT and FCKO parasites to α, β-arteether and chloroquine. a, b Blood parasitemia and mortality curves of infected mice treated with α,β-arteether, respectively. The data represent four mice for each group (n.s not significant, log-rank (Mantel–Cox) test). **c, d** Blood parasitemia and mortality curves of infected mice treated with chloroquine, respectively. The data represent four mice for each group (**P < 0.01, log-rank (Mantel–Cox) test). For (**a, c**), the data represent mean ± SD. Individual data points are shown with the respective light shaded colors. Source data are provided as a Source Data file.
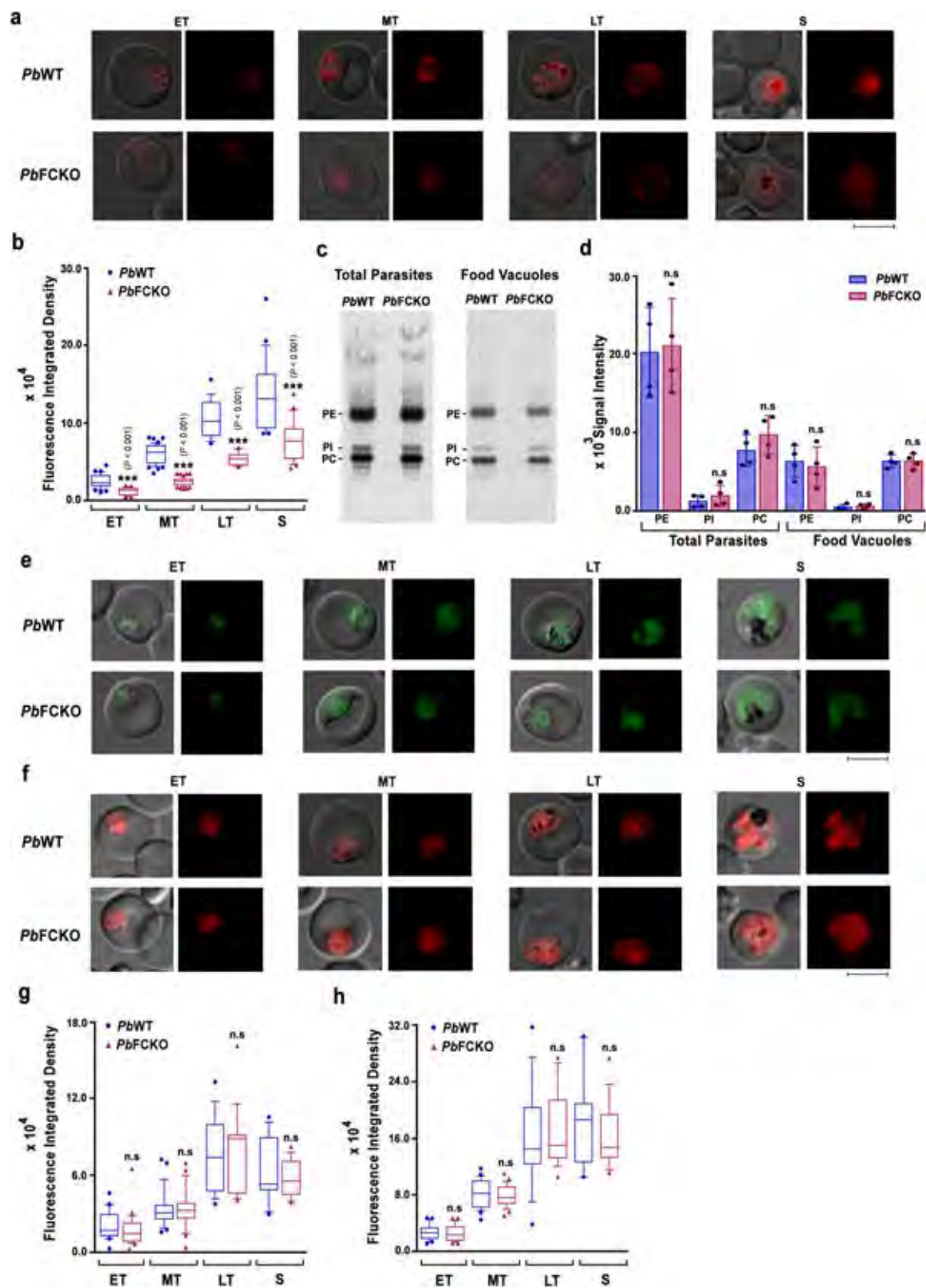
formation in *Pf*3D7 laboratory strain, artemisinin-resistant *Pf* clinical isolate from Cambodia (*Pf*Cam), multidrug-resistant *Pf* clinical isolate from Thailand (*Pf*K1) and three *Pf* clinical isolates that were collected from India (*Pf*I-1, −2 and −3). Unlike the approach of Smith *et al*[58], we did not preload the host RBCs with griseofulvin for 3 days and use them for parasite invasion, to avoid any off-target effect. We directly treated infected RBCs having *Pf* late rings and early trophozoites with griseofulvin for 72 h and examined Hz content in the schizonts of next cycle. We first performed growth analysis in *Pf*3D7 using different concentrations of griseofulvin. Even at a 1 mM concentration, griseofulvin could not inhibit 50% of the parasite growth (Fig. 10a), a pattern that was consistent with the dispensable nature of parasite heme pathway and similar to that of succinylacetone - another heme pathway inhibitor[34]. We examined the ability of girseofulvin to inhibit de novo heme synthesis by performing ^{14}C-ALA labeling at 100 and 200 µM concentrations. The mature RBCs used for culturing *Pf* parasites lack FC and do not synthesize heme. Therefore, heme labeling reflects the effect of griseofulvin on parasite de novo heme synthesis. There was almost 45 and 80% inhibition of ^{14}C-ALA incorporation into parasite heme (Fig. 10b) in comparison to 5 and 15% of parasite growth inhibition at 100 and 200 µM concentrations, respectively. More importantly, griseofulvin could inhibit Hz formation in *Pf*3D7 cultures to the extent of ~40 and 70% at 100 and 200 µM concentrations, respectively (Fig. 10c). There was also a significant decrease in free heme levels (Fig. 10d). The decrease in Hz formation could be visualized in Giemsa-stained smears prepared from infected RBCs (Fig. 10e). Griseofulvin inhibited Hz formation in all the clinical isolates that were examined (Fig. 10f).

All these evidences suggested that inhibition of de novo heme synthesis by griseofulvin affects Hz levels in human parasites as well, and griseofulvin has the potential to serve as an adjunct drug for cerebral and severe malaria in humans that needs to be evaluated in clinical trials.

Discussion

Parasite heme pathway has remained enigmatic for more than two decades and the dichotomy between de novo heme and host-heme/porphyrin acquisition pathways in the asexual stages is obscure. Here, we provide an explanation as to why asexual parasite expresses "dispensable" heme pathway enzymes and synthesizes heme despite acquiring host heme. We show that de novo heme pathway is associated with disease virulence and it induces cerebral pathogenesis by promoting Hz formation. Hz is a key malarial PAMP associated with aberrant inflammatory responses, endothelial activation promoting pRBC sequestration, T cell infiltration and neuronal apoptosis. Upon phagocytosis, Hz can induce the production of pro-inflammatory cytokines and chemokines in neutrophils, monocytes, macrophages and DCs, leading to the increased expression of ICAM-1 in endothelial cells and enhanced sequestration of pRBCs. Hz can also trigger IL-1β production by activating NLRP3 inflammasome, and augment endothelial cell damage and loss of BBB integrity. Hz can induce proinflammatory responses in endothelial cells and activate coagulation and complement pathways[12,15]. The KO parasites synthesize less Hz and mice infected with KO parasites are devoid of cerebral complications. The plasma levels of IL-6, TNFα, IFNγ, G-CSF, CCL3 and CCL5 are significantly decreased in KO-

infected mice. These cytokines and chemokines are known to be highly elevated in the serum samples of cerebral and severe malaria patients[15,59,60]. There is also a concomitant increase in anti-inflammatory cytokines such as IL-4, IL-10 and IL-13 in the KO-infected mice suggesting an over-all decrease in the systemic inflammation.

The transcript levels of TNFα, IFNγ, CXCL9, CXCL10, CCL2, CCL5 and CCL19 are low in the brain samples of KO-infected mice. CXCL9 and CXCL10 are highly induced in the brain of ECM mice and elevated levels of CXCL10 in plasma and cerebrospinal fluid predict fatal CM in humans[61]. CCL2, CCL5 and CCL19 associated with leukocyte migration are known to be

Fig. 7 Assessment of food vacuole pH, phospholipids and neutral lipids in FCKO parasites. a Live cell fluorescence imaging of LysoTracker Deep Red uptake in *Pb*WT and *Pb*FCKO parasites. **b** Quantification of fluorescence signal from various stages. *Pb*WT − 98 trophozoites and 22 schizonts; *Pb*FCKO − 95 trophozoites and 23 schizonts. ET, MT and LT early, mid and late trophozoites; S schizonts. Images were captured using 100x objective. Scale bar = 5 μm. (***$P < 0.001$, unpaired *t*-test; two-sided). **c** TLC separation of ^{32}P-orthophosphoric acid radiolabelled phospholipids for *Pb*WT and *Pb*FCKO total parasites and FVs. Half the phospholipid preparation was used for total parasites. For FVs, entire preparation was used. PC phosphatidylcholine, PI phosphatidylinositol, PE phosphatidylethanolamine. **d** Band intensities quantified (mean ± SD; n.s not significant, unpaired *t*-test; two-sided). The data represent four different experiments. Individual data points are shown as black circles. **e** Live cell fluorescence imaging of BODIPY 493/503 staining in *Pb*WT and *Pb*FCKO parasites. Images were captured using 100x objective. Scale bar = 5 μm. **f** Live cell fluorescence imaging of Nile Red staining in *Pb*WT and *Pb*FCKO parasites. Images were captured using 100x objective. Scale bar = 5 μm. **g** Quantification of the fluorescence signal from various stages for BODIPY 493/503 staining. The data represent 69 trophozoites and 15 schizonts for *Pb*WT, and 68 trophozoites and 14 schizonts for *Pb*FCKO (n.s not significant, unpaired *t*-test; two-sided). **h** Quantification of the fluorescence signal from various stages for Nile Red staining. The data represent 68 trophozoites and 14 schizonts for *Pb*WT, and 70 trophozoites and 14 schizonts for *Pb*FCKO (n.s not significant, unpaired *t*-test; two-sided). ET early trophozoites, MT mid trophozoites, LT late trophozoites, S schizonts. For (**b**, **g**, **h**), Box and whisker plots display 10th and 90th percentile as the whiskers, 25th−75th percentile as the boxes and median as the centre line. Source data are provided as a Source Data file.

induced by Hz in monocyte-derived DCs, macrophages and neutrophils[12,15,16,62]. Similar decrease was also observed in the transcript levels of ICAM-1, p-selectin, perforin, and granzyme B, the key adhesion and cytotoxic effector molecules. Low transcript levels of HO-1 in KO-infected mice might be due to less inflammation and decreased extracellular heme—the two potent HO-1 inducers[19,20]. Further, there is a decrease in the infiltration of CD8$^+$ T cells expressing early activation marker CD69, and proinflammatory and cytotoxic effector molecules such as TNFα$^+$, IFNγ$^+$, CXCR3$^+$, perforin and granzyme B that lead to endothelial leakage, BBB disruption and neuronal damage. There is also a reduction in phospho-NF-κB and NLRP3 inflammasome formation with decreased caspase-1 activation and less production of IL-1β - a key mediator of inflammation, infiltration of immune cells and neuronal apoptosis. Genetic complementation can restore Hz formation in the KO parasites and the mice infected with complemented KO parasites develop ECM.

The decrease in Hz synthesis is reflected in the reduced Hz load in the organs, and decreased free heme levels in the parasites and plasma samples of KO-infected mice. It is suggested that oxidized heme derived from host Hb release during schizont rupture contributes to free plasma heme responsible for severe malaria and CM pathogenesis[19–21]. Interestingly, plasma levels of Hb and heme scavenging proteins like hemopexin in KO-infected mice are comparable with WT-infected mice suggesting that the decreased plasma heme levels might be due to changes in parasite heme/Hz levels. While less Hz formation can be directly associated with reduced labile/free heme levels in KO parasites, the decrease in plasma free heme needs further investigations. Despite thriving in a heme-rich milieu, parasite maintains cytosolic free heme concentrations of ~1.6 μM, comparable with ~0.4–0.6 μM concentrations seen in mammalian cells[63]. It is possible that the parasite could have evolved with protein-/transporter-based mechanisms to dispose excess free heme from the cytosol and this could be the reason for reduced plasma free heme levels in KO-infected mice. For example, HRP capable of binding heme is secreted by the parasite. Altogether, our findings suggest that de novo heme in the blood stages can influence the levels of Hz and free heme—a key PAMP and DAMP associated with malaria pathogenesis.

Chloroquine acts predominantly by inhibiting host Hb-heme polymerization into Hz and it has been suggested that activation of artemisinin requires heme[44,45]. In agreement with decreased Hz formation, the sensitivity of FCKO parasites to chloroquine is compromised. In vitro chloroquine sensitivity is shown to be unaltered in heme pathway KO *Pf* cultures that are treated with chloroquine for 48 h and maintained using mature RBCs[36]. Our in vivo results with *Pb* suggest that FCKO parasites have greater propensity for recrudescence, despite their initial clearance with chloroquine is comparable to WT as observed in *Pf* cultures. It is

known that *Pb* mutant parasites defective in Hb proteolysis producing less or no Hz can survive in reticulocytes exhibiting chloroquine resistance[52]. This could be the reason behind the early in vivo recrudescence of FCKO parasites as well. Nevertheless, the in vivo sensitivity to α,β-arteether remains unaltered. Our results suggest that albeit a ~50% decrease, the host-derived labile heme present in the cytosol of FCKO parasites is adequate to activate α,β-arteether and the role of de novo heme is confined to cerebral pathogenesis.

The host Hb degradation in asexual stage parasites can release as much as ~15 mM heme[63] and therefore, utilization of host heme cannot account for almost 75% decrease in the Hz synthesis of KO parasites. Here, we show the unexpected role of de novo heme in influencing the detoxification of Hb-heme into Hz by regulating the FV integrity in asexual stages (Fig. 10g). FVs of FCKO parasites are compromised in terms of pH, lipid unsaturation and proteins associated with Hz formation. It is known that acidic pH of FV is critical for Hb digestion by proteases and subsequent Hz formation. The decrease in LysoTracker Deep Red uptake suggests that the FCKO FVs are less acidic. Our results also suggest the lower abundance of V-type H$^+$ATPase subunits and berghepain-2 in FCKO FVs. V-type H$^+$ATPase is a proton pump mainly responsible for maintaining the acidic pH of FV. Targeting V-type H$^+$ATPase activity with concanamycin A or bafilomycin A1 can lead to the alkalinisation of FV and inhibition of parasite growth[51]. *Pb* has two isoforms of berghepain—berghepain-1 and −2 of which, berghepain-1 is associated with hepatic merozoite invasion and erythrocyte tropism, and berghepain-2 seems to be involved in Hb digestion[52,53].

Further, we show reduction in OA synthesis of FCKO parasites with not much change in phospholipids or neutral lipids, suggesting an alteration in the degree of lipid unsaturation that can affect Hz formation. OA synthesis in malaria parasite is catalyzed by a heme-dependent, ER-localized, Δ9-desaturase and it does not occur in uninfected RBCs[48,49]. Our results suggest the specific role of de novo heme in OA synthesis that cannot be compensated by host Hb-heme. The levels of unsaturated fatty acids are also shown to stimulate the function of V-type H$^+$ATPase in plants[64]. The decrease in OA synthesis and lipid unsaturation can affect other cellular processes such as membrane homeostasis, protein/lipid trafficking, protein folding, cell signaling etc[65]. Many of these can collectively contribute for the loss of FV integrity and responsible for the lower abundance of V-type H$^+$ATPase subunits and berghepain-2 in FCKO FVs. Although host Hb-heme acquisition starts from late ring stages, it is possible that FV integrity and maturation depend on de novo heme. Our results provide functional insights on de novo heme that could be a miniscule in comparison with massive amounts of heme derived from host Hb. Intriguingly, we show it is the de
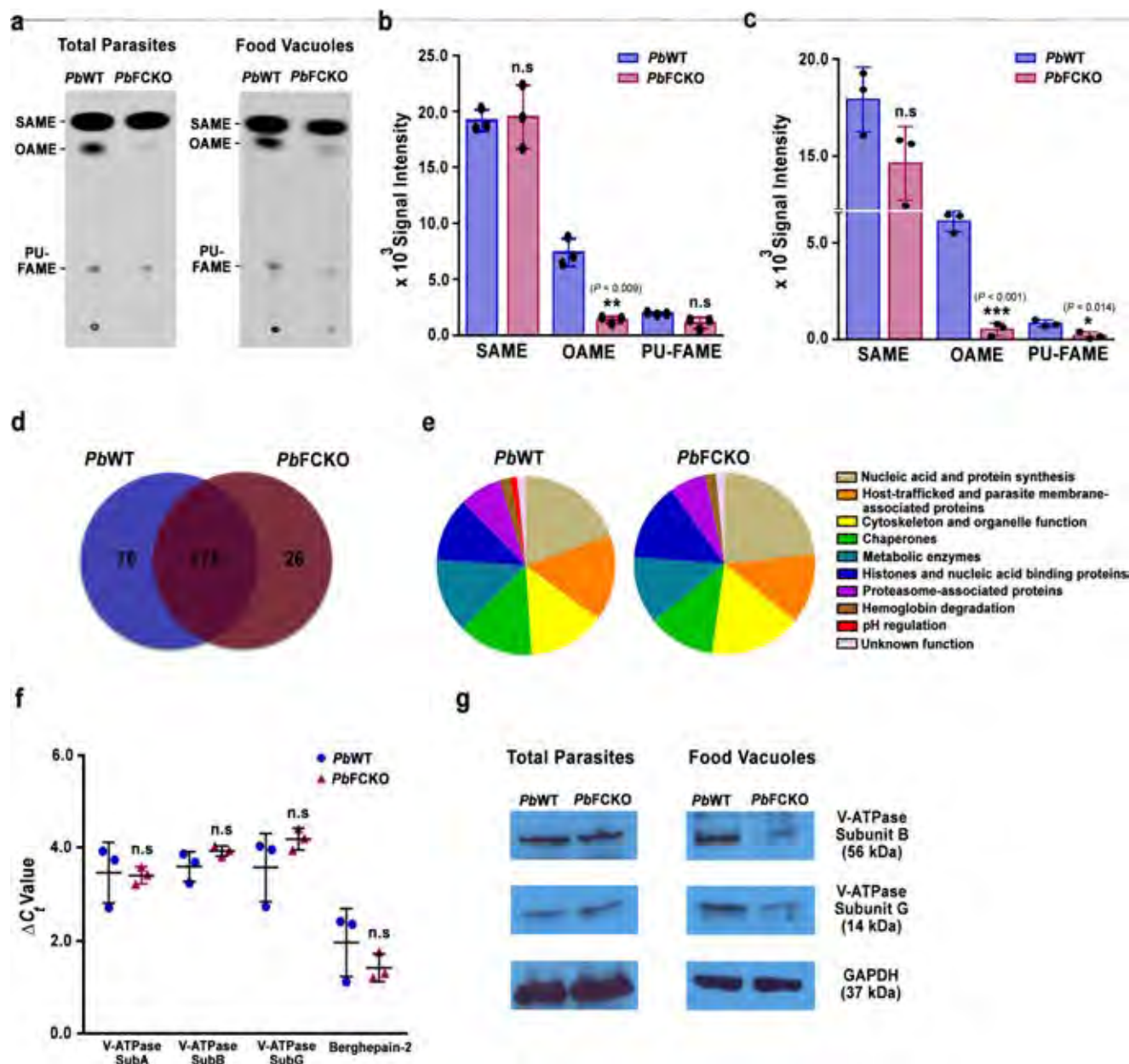
Fig. 8 Evaluation of OA synthesis and FV proteomics for WT and FCKO parasites. a TLC separation of ^{14}C-SA radiolabelled unsaturated FAMEs for *Pb*WT and *Pb*FCKO total parasites and FVs. One third of the FAME preparation used for total parasites and entire preparation used for FVs. **b, c** Band intensities quantified for total parasites and FVs, respectively (mean ± SD; n.s not significant, *$P < 0.05$, **$P < 0.01$, ***$P < 0.001$, unpaired t-test; two-sided), from three different experiments. Individual data points are shown as black circles. **d** Venn diagram of total proteins identified in the *Pb*WT and *Pb*FCKO FVs. **e** Functional classification of the proteins based on gene ontologies available at PlasmoDB and UniProt databases. Supplementary Data 1 and Supplementary Data 2 have the complete set of details related to *Pb*WT and *Pb*FCKO FV proteome analyses. Three different FV preparations of *Pb*WT and *Pb*FCKO were pooled independently to get adequate amount of protein for the proteomics analyses. **f** qPCR analysis of RNA transcripts. The ΔC_t values obtained with respect to parasite GAPDH were plotted (mean ± SD; n.s not significant, unpaired t-test; two-sided). The data represent three different preparations of RNA from WT and FCKO parasites. **g** Western analysis of V-type H$^+$ATPase subunits. The total parasite preparations represent parasite pellets pooled from two different mice. For FVs, three different FV pellets were pooled separately for WT and FCKO. These preparations were independent of those that were used for proteomics analysis. GAPDH is known to be present in FVs and therefore, used as a control for total parasite and FV preparations. ($n = 2$ independent experiments). Full-length blots are provided in the Supplementary Fig. 7. Source data are provided as a Source Data file.

novo heme that influences the detoxification of host heme into Hz and disease pathogenesis. Despite the ability of blood stage parasites to acquire host Hb-heme for survival, lack of de novo heme synthesis renders them less virulent.

It would be interesting to examine whether (i) de novo heme regulates other metabolic pathways or organellar functions and influences the trafficking mechanisms associated with host-heme

or Hb uptake and (ii) compartmentalization of de novo and Hb-heme make them functionally different. Similarly, the role of Δ9-desaturase in cerebral pathogenesis and the requirement of 'dispensable' biosynthetic heme for ER-localized cytochrome b5-dependent Δ9-desaturase activity need to be understood. Cytochrome b5 also supports minimal ETC activity and pyrimidine biosynthesis that are indispensable for asexual stages.
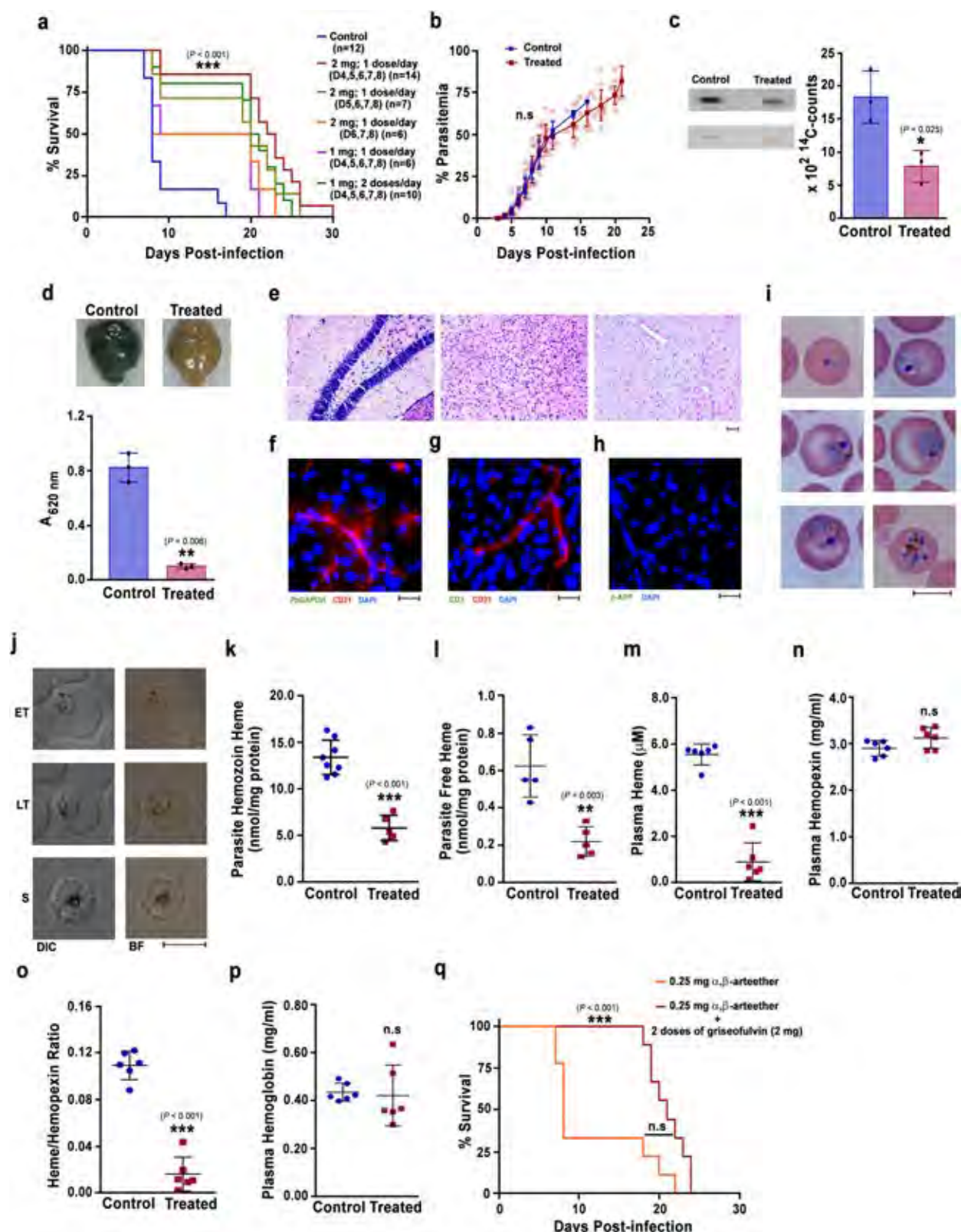
Plasmodium has at least two putative isoforms of cytochrome b5 annotated in PlasmoDB and one of them seems to be non-essential for asexual growth. It would be of interest to examine whether the non-essential cytochrome b5 participates in Δ9-desaturase activity, and its heme requirement is satisfied by biosynthetic heme and could not be compensated by Hb-heme. Further, the accessibility of Hb-heme to various organelles and its incorporation in hemoproteins may vary. Besides its role in disease pathogenesis, Hz is also associated with parasite sequestration, manipulation of host immune responses etc. that can exert selection pressure for the existence of molecular mechanisms to optimize its formation. Altogether, our findings suggest the importance of "dispensable" de novo heme pathway in the asexual stages despite its non-essentiality for parasite growth.

Fig. 9 Effect of griseofulvin treatment on CM pathogenesis. a Mortality curves of *Pb*WT-infected mice treated with different dosages of griseofulvin (***$P < 0.001$, log-rank (Mantel–Cox) test). **b** Growth curve analysis ($n = 12$) for 2 mg dose per day on day 4, 5, 6, 7, and 8 (mean ± SD; n.s not significant, Two-way ANOVA). **c** Phosphorimager and scanned images of TLC performed for ^{14}C-ALA labeled parasite free heme and the radioactive counts measured for three different experiments (mean ± SD; n.s not significant, *$P < 0.05$, unpaired *t*-test; two-sided). Individual data points are shown as black circles. Full-length scans are provided in the Supplementary Fig. 7. **d** Extravasation of Evans blue and its quantification ($n = 3$) (mean ± SD; **$P < 0.01$, unpaired *t*-test; two-sided). Individual data points are shown as black circles. **e** H&E staining of the brain sections. Images were captured using 10x objective. Scale bar = 50 μm. $n = 3$ independent experiments. **f** Parasite accumulation **g** CD3^{+} cells in the blood vessels. $n = 2$ independent experiments. **h** Axonal injury in the brain sections. Images were captured using 20x objective. Scale bar = 20 μm. $n = 3$ independent experiments. **i** Giemsa-stained parasites. Images were captured using 100x objective. Scale bar = 5 μm. $n = 3$ independent experiments. **j** Hz content in differential interference contrast (DIC; left) and bright field images (right) of paraformaldehyde-fixed RBCs. Images were captured using 100x objective. Scale bar = 5 μm. $n = 3$ independent experiments. **k** Parasite Hz ($n = 8$ for control; $n = 5$ for treated). **l** Parasite free heme ($n = 5$). **m** Plasma free heme ($n = 6$). **n** Plasma hemopexin ($n = 6$). **o** Plasma heme/hemopexin ratio. **p** Plasma hemoglobin ($n = 6$). **k–p** (mean ± SD; n.s not significant, **$P \le 0.01$, ***$P < 0.001$, unpaired *t*-test; two-sided). **q** Mortality curves for *Pb*WT-infected C57BL/6 female mice treated with α,β-arteether alone ($n = 9$) and α,β-arteether in combination with griseofulvin ($n = 9$). The data represent two different batches. (***$P < 0.001$, n.s not significant, log-rank (Mantel–Cox) test). Source data are provided as a Source Data file.

The fatality rates in malaria do not correlate with parasite clearance and therefore, targeting parasite virulence becomes important. The malaria deaths that occur despite treating the infected individuals with ACTs and the decreasing efficacy of ACTs that lead to delayed parasite clearance underscore the need of an adjunct therapy in the initial stages of ACT treatment. Until now, the attempts to develop adjunct therapies with candidates acting mainly on host responses did not succeed in clinical trials and only a few candidates are in the pipeline for evaluation in HCM[4,66]. We show that de novo heme in the blood stages can serve as a target for malaria pathogenesis. Griseofulvin—a FDA-approved antifungal drug prevents ECM in mice and delays death due to anemia by inhibiting parasite heme synthesis. The ability of griseofulvin to prevent disease pathogenesis is observed despite the absence of any antimalarial treatment. Griseofulvin treatment does not affect the parasite growth suggesting that ECM protection is not because of the inhibition of parasite mitosis. This is in concurrence with a clinical trial conducted in malaria-infected humans where, griseofulvin treatment did not affect in vivo parasite growth although NMPP formation occurred within the parasite. The participants were rescued early with ACT and therefore, no observations were made on disease severity[58]. Griseofulvin can also prevent ECM in *Pb*-infected mice treated with α,β-arteether at the late stages of infections with onset of neurological symptoms. It inhibits parasite heme synthesis and Hz formation in *Pf* clinical isolates as well.

Our study identifies a unique approach of targeting Hz through de novo heme to mitigate parasite virulence. Since de novo heme pathway is dispensable for asexual stages, there is a possibility of less selection pressure to result in resistance development. Griseofulvin can significantly affect host heme and porphyrin metabolism only at dosages of prolonged duration that are several fold higher than the therapeutic dose, although any subtle impact at lower doses cannot be ruled out. Conversely, malaria treatment is only for a shorter duration. Given the central role played by Hz in malaria pathogenesis, repurposing of griseofulvin can serve as an excellent adjunct to ACTs for cerebral and severe malaria that needs to be evaluated in clinical trials.

Methods

Ethics statement. All the studies involving mice were carried out with the approval of Institutional Animal Ethics Committee (ILS/IAEC-57-AH/JAN-16), Institute of Life Sciences, Bhubaneswar, according to the national guidelines framed by "The Committee for the Purpose of Control and Supervision of Experiments on Animals (CPCSEA)". *P. falciparum* clinical samples were collected with the approval of Institutional Ethics Committee (IEB) / Institutional Review Board (IRB) (94/HEC/19), Institute of Life Sciences, Bhubaneswar.

Routine propagation of *Pb* in mice and CM experiments. *Pb*ANKA WT and KO parasites were propagated in C57BL/6 male mice of 7–8 weeks old. Peripheral

blood parasitemia was monitored by performing light microscopy for Giemsa-stained thin blood smears prepared from tail vein blood. When the blood parasitemia was around 10%, 10^5 *P. berghei* ANKA WT or 10^5/10^7 ALAS/FC KO parasites were collected and injected intraperitoneally in 7–8 weeks old C57BL/6 male naïve mice to initiate ECM experiments. The male mice were preferred for uniformity in the experiments and the results on parasite growth, ECM protection, decrease in heme and hemozoin levels, and prevention of ECM by griseofulvin were reproducible in 7–8 weeks old C57BL/6 female mice as well. The experiments for which C57BL/6 female mice were used are mentioned in the figure legends. Balb/c male mice of 7–8 weeks old were used to examine growth phenotype, heme and hemozoin levels, and for raising polyclonal sera. Breeding and maintenance of mice were performed at the animal house facility of Institute of Life Sciences, Bhubaneswar, under standard conditions of 25 ± 3 °C temperature, 40–50% relative humidity, and 12 h light/12 h dark cycle. Growth curve analysis was carried out by monitoring the blood parasitemia. The development and progression of ECM were monitored by examining RMCBS for neurological symptoms as described[67]. On the respective days, WT- or KO-infected C57BL/6 mice were assessed for coordination (gait and balance), exploratory behavior (motor performance), strength and tone (body position and limb strength), reflexes and self-preservation (touch escape, pinna reflex, toe pinch and aggression) and hygiene-related behavior (grooming). Each parameter was scored for 0–2 (0 as the lowest and 2 as the highest), for a total RMCBS score of 20. To assess BBB integrity, Evans blue uptake assays were carried out by injecting 200 μl of 2% Evans blue in PBS intravenously and examining the extravasation of dye after one h in the brain of the infected mice that were transcardially perfused with PBS. The extent of BBB damage was quantified by incubating the brain samples in formamide at 37 °C for 48 h, extracting the Evans blue and measuring the absorbance at 620 nm[19].

Histological and immunofluorescence analyses of cerebral pathology. For H&E staining to assess vascular blockage, hemorrhages and demyelination, brain samples were fixed with formalin for 72 h at room temperature. After dehydrating with ethanol and treating with xylene, paraffin embedded blocks were made and sections of 7 μm thickness were prepared using Leica RM2125RT rotary microtome. The sections were then processed and stained with H&E using standard protocols. Immunohistochemical analysis of IgG extravasation in the brain sections was carried out as described[11]. The brain sections of 30 μm thickness were antigen retrieved by treating them at 95 °C for 30 min in sodium citrate buffer pH 6.0, followed by blocking with 3% H_2O_2 at room temperature for 30 min to prevent endogenous peroxidase activity. The sections were then incubated with HRP-conjugated goat anti-mouse IgG (Abcam, ab97023) at 1:250 dilution in PBS containing 0.3% Triton X-100 and 0.1% BSA, followed by developing with diamino-benzidine tetrahydrochloride (Vector Labs, SK-4100) and counterstaining with hematoxilin (HiMedia, S058). Immunoflourescence analysis of brain sections for parasite sequestration was carried out as described[11] by fixing the brain samples in 4% paraformaldehyde in PBS containing 20% sucrose for 24 h at 4 °C and cryo-protecting them for 48 h in PBS containing 20% sucrose. Coronal sections of 30 μm thickness were prepared using Leica CM1850 cryostat microtome and antigen retrieval was carried out by treating them at 95 °C for 30 min in sodium citrate buffer pH 9.0. After blocking with 1% BSA, the sections were incubated with anti-CD31 mouse monoclonal antibody (1:200 dilution) conjugated with Alexa Fluor 594 (SantaCruz, sc-376764) and anti-*Pb*GAPDH rabbit polyclonal serum (1:100 dilution) or anti-mouse CD3 rat monoclonal antibody (Thermo Fisher Scientific, 14-0032-82; 1:100 dilution) for 16 h at 4 °C. The sections were then treated with FITC-conjugated donkey anti-rabbit IgG (SantaCruz, sc-2090; 1:200 dilution) or FITC-conjugated goat anti-rat IgG (SantaCruz, sc-2011; 1:200 dilution), followed by 4′,6-diamidino-2-phenylindole (DAPI) staining. Anti-mouse β-APP rabbit polyclonal antibody (Thermo Fisher Scientific, 51–2700) was used in 1:200 dilution. All the images were captured using Olympus IX83 microscope with DP73 high-performance camera.
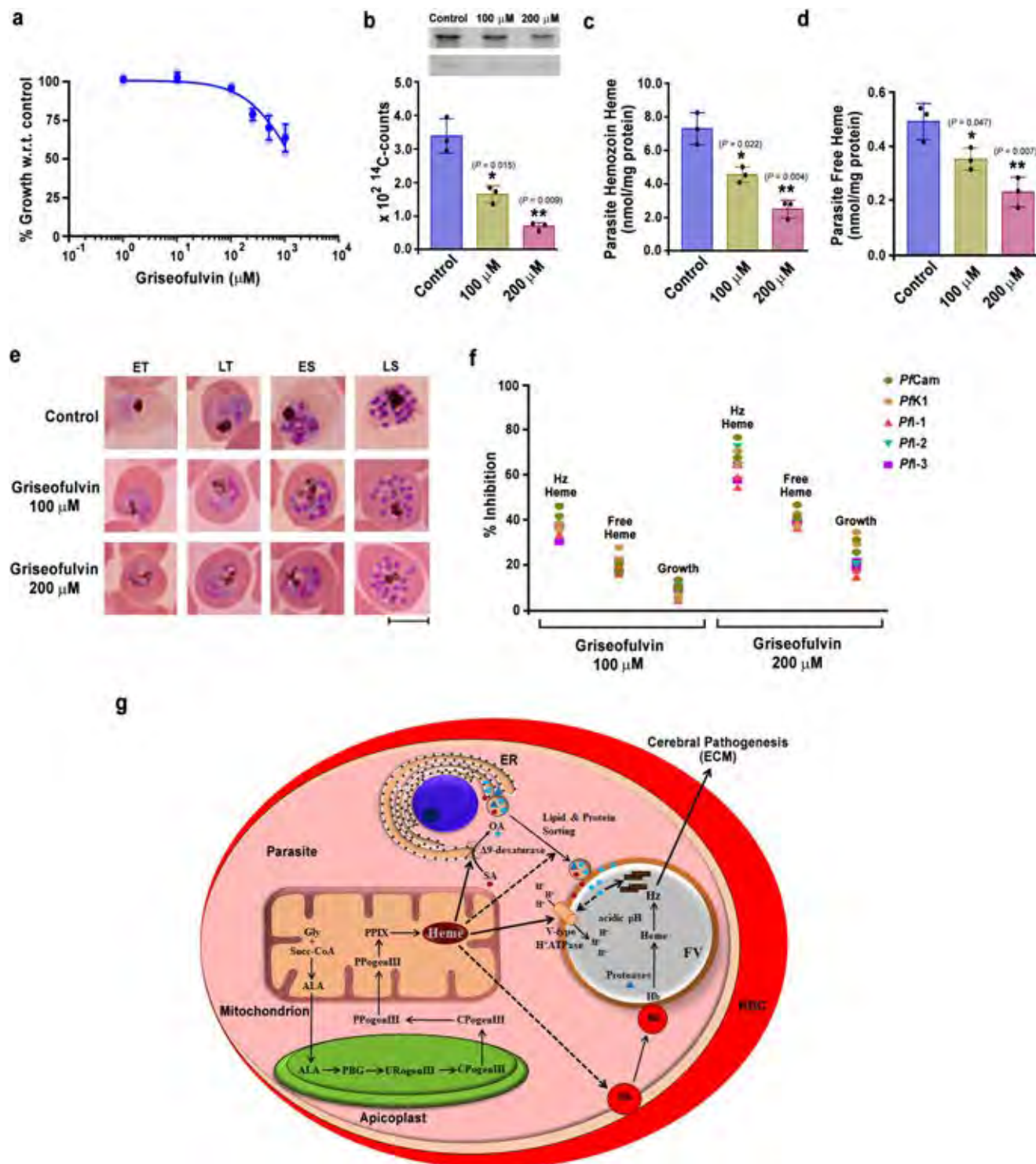
Heme, Hz, hemoglobin and hemopexin estimations. Free heme levels in the plasma samples of WT- and KO-infected mice were quantified using Hemin colorimetric assay kit (BioVision, K672) as per the manufacturer's protocol. The assay is specific for free heme and it utilizes peroxidase activity of hemin to facilitate the conversion of a colorless probe to a strongly colored compound with absorbance at 570 nm. The quantification of free heme in the parasite lysates was carried out by resuspending the parasite pellets in 5 volumes of hypotonic lysis buffer containing 5 mM Tris pH 7.5 with protease inhibitors and incubating them in ice for 30 min. The lysates were then centrifuged at 20,000 g for 20 min, 4 °C, and the supernatants obtained were used for free heme estimation as mentioned above for the plasma samples. The protein content of the hypotonic lysates was measured by Micro BCA protein assay kit (Thermo Fisher Scientific, 23235) and the free heme levels were expressed per mg of protein. The Hz content of the WT and KO parasite pellets

was estimated as described[68]. The parasite pellet was resuspended in 1 ml of 100 mM sodium acetate buffer, pH 5.0 and left at 37 °C for overnight, followed by centrifugation at 10,000 g for 5 min. The resultant pellet was resuspended in 100 mM Tris buffer pH 8.0 containing 2.5% SDS and incubated at 37 °C for 30 min, followed by centrifugation at 10,000 g for 5 min. The pellet obtained was washed once with 100 mM sodium bicarbonate pH 9.2 and then with distilled water. The final Hz pellet was dissolved in 100 mM NaOH containing 2.5% SDS, and the absorbance was measured at 405 nm. The supernatants of sodium acetate and Tris SDS steps were collected to estimate the protein content and heme content of the Hz was expressed per mg of total protein. To estimate the Hz content in the spleen and liver of the WT- and KO-infected mice, 50 mg tissue of the respective organs was homogenized in 50 mM Tris pH 8.0 containing 50 mM NaCl, 5 mM $CaCl_2$ and 1% Triton X-100, and incubated for 12 h at 37 °C in the presence of proteinase K.

Fig. 10 Effect of griseofulvin on *Pf* parasites and model depicting the role of de novo heme in regulating FV integrity and Hz formation. a Effect of griseofuvin on *Pf*3D7 parasite growth. The data (mean ± SD; R square = 0.8623) represent three different experiments. Individual data points are shown with the light shaded color. **b** Incorporation of ^{14}C-ALA into *Pf*3D7 parasite de novo heme. The radioactive counts represent three different experiments (mean ± SD; *P* < 0.05, **P* < 0.01, unpaired *t*-test; two-sided). Individual data points are shown as black circles. Phosphorimager and scanned images of TLC performed for ^{14}C-ALA labeled parasite free heme are also shown. Full-length scans are provided in the Supplementary Fig. 7. **c** *Pf*3D7 parasite Hz. **d** *Pf*3D7 parasite free heme. The data represent three different experiments (mean ± SD; *P* < 0.05, **P* < 0.01, unpaired *t*-test; two-sided). For **c** and **d**, individual data points are shown as black circles. **e** Giemsa-stained images of *Pf*3D7 parasites treated with griseofulvin. ET and LT early and late trophozoites; ES and LS early and late schizonts. Images were captured using 100x objective. Scale bar = 5 μm. *n* = 3 independent experiments. **f** Assessment of parasite Hz, free heme and growth in *Pf* clinical isolates. The data represent two different experiments for each clinical isolate. Percentage of inhibition was calculated with respect to untreated DMSO control. Individual data points are shown. **g** De novo heme pathway of malaria parasite and Hz formation in the FV are represented. Solid arrows indicate the effect of de novo heme on V-type H$^+$-ATPase, FV pH and OA synthesis affecting hemozoin formation. Dashed arrows represent the probable effects of de novo heme on Hb endocytosis, and protein and lipid trafficking. Gly glycine, Succ-coA succinyl coenzymeA, ALA δ-aminolevulinic acid, PBG prophobilinogen, URogenIII uroporphyrinogen III, CPogenIII coproporphyrinogen III, PPogenIII protoporphyrinogen III, PPIX protoporphyrin IX, ER endoplasmic reticulum. Source data are provided as a Source Data file.

The lysates were sonicated and centrifuged at 15,000 *g* for 30 min. The pellets obtained were resuspended with 100 mM sodium bicarbonate containing 2% SDS and sonicated, followed by centrifugation at 15,000 *g* for 15 min. After repeating this step thrice, the pellets were solubilized in 100 mM NaOH containing 2% SDS and 3 mM EDTA, and the absorbance was measured at 405 nm[69]. In parallel, the parasite load in the organs was examined by quantitative PCR (qPCR) analysis carried out with *Pb18SrRNA* primers for the total RNA isolated from 30 mg tissue of the organs using RNeasy Plus Mini Kit (Qiagen, 74134). After normalizing with respect to the parasite load, the total heme content of the Hz isolated was expressed per mg weight of the organ. Hemoglobin and hemopexin levels in the plasma samples of WT- and KO-infected mice were measured by Mouse Hemoglobin (Abcam, ab157715) and Mouse Hemopexin (Abcam, ab157716) ELISA kits as per the manufacturer's protocols.

PbALASKO^{Luc}, PbFCKO^{Luc}, PbControl^{Luc} and PbFCKO^{+FC} parasites. *Pb*A-LASKO^{Luc} and *Pb*FCKO^{Luc} parasites were generated by transfecting WT parasites with GOMO-GFP-Luc plasmid containing GFP-Luc-expressing cassette with m-cherry flanked on either side by 5′- and 3′-UTR regions of the respective genes. The primers utilized were similar to the earlier ones that were used for generating *Pb*ALASKO and *Pb*FCKO[34] except that the restriction sites used for forward and reverse primers were SacII and NotI for 5′ UTRs and XhoI and KpnI for 3′ UTRs, respectively. For *Pb*Control^{Luc} parasites, the following sets of forward and reverse primers were used to amplify the 5′- and 3′-UTRs of small subunit ribosomal RNA (*ssurRNA*): 5′UTR (F) – GCCACCGCGGGAAATACGACCAATATGTAATTAT TGGATAATAATTG; 5′UTR (R) – GCCCGCGGCCGCCTACTGGCAAGATCAA CCAGGTTACTATATATA; 3′UTR (F) – GCCACTCGAGGAGGCTTATCCTTC CTGATAAAGTG; 3′UTR (R) – GCCCGGTACCCAAAATACTAACCCACTATG TGCAATGTGC. The restriction sites are underlined. The 5′ and 3′ UTRs were cloned into GOMO-GFP-Luc plasmid and transfection was carried out in WT parasites. The transfections were performed with 4D-Nucleofector using P5 Primary Cell 4D-Nucleofector reagent (Lonza, V4XP-5012). The transfected parasites were selected with pyrimethamine and clonal selection was carried out by performing limiting dilutions. To perform FC complementation, *Pb*FCKO^{Luc}-infected mice were treated with 5-fluorocytosine to remove the pyrimethamine-selectable h*DHFR*-y*FCU* fusion gene from *Pb*FCKO^{Luc} parasites. The recovery of selectable marker-free *Pb*FCKO^{Luc} parasites was confirmed by the loss of m-cherry fluorescence. The parasites were then transfected with pL1102 plasmid in which RFP under *Pbeef1α* promoter was replaced with *Pb*FC under its native promoter. In brief, pL1102 plasmid was digested with AflII and XbaI to remove RFP and its promoter, followed by cloning of −906 to +1547 sequence representing *Pb*FC promoter and its coding sequence that was PCR amplified with the following forward and reverse primers: GCAACTTAAGTGGAGCATTTTCATGCTCATA AATATATTC and GCAATCTAGATTACCAGCCACTTAGATTTTTTTCAA TAAT. The restriction sites are underlined. The transfected *Pb*FCKO^{Luc} parasites having FC reintroduced in *c-ssurRNA* locus (*Pb*FCKO^{+FC}) were selected with pyrimethamine and clonal selection was carried out by limiting dilution.

In vivo bioluminescence imaging. In vivo bioluminescence imaging for mice infected with WT and KO parasite lines expressing luciferase was carried out as described[70]. For whole body imaging, 7–8 weeks old C57BL/6 mice were injected with Luc-expressing 10^5 WT or 10^7 KO parasites. On day 8 post-infection, mice were injected intraperitoneally with D-luciferin substrate (100 mg/kg animal weight in 200 μl of PBS), VivoGlo (Promega, P1041), and imaged after 5 min using in vivo Imaging System IVIS Lumina *XR* with medium binning, 10 s exposure and 12.5 FOV, under XGI-8 gas anesthesia system. For ex vivo imaging, transcardial perfusion was carried out for infected mice with cold PBS after injecting D-luciferin, and the organs were dissected out and imaged.

Analyses of cytokines, chemokines and chemokine receptors. Bio-Plex assays for cytokines and chemokines were carried out in Bio-Plex 200 system using Bio-Plex Pro Mouse Cytokine Grp I Panel 23-Plex assay kit (Bio-Rad, M60009RDPD) following manufacturer's protocol. The plasma samples utilized for the assays were prepared from the infected mouse blood collected on day7/8 post-infection. For transcript levels, total RNA was isolated from the brain samples of WT and KO-infected mice that were collected after a thorough perfusion with cold PBS. qPCR analyses were performed using QuantiFast SYBR Green RT-PCR Kit (Qiagen, 204154) on StepOne Real-Time PCR System (Applied Biosystems). The primers used were listed in Supplementary Table 2. Expression levels were normalized with GAPDH and fold changes for the transcripts of KO-infected mice with respect to WT were calculated using $2^{(-\Delta\Delta Ct)}$ method. To examine the transcript levels of parasite proteins, total RNA was isolated from the parasite pellets and the expression levels were normalized with respect to parasite GAPDH.

Flow cytometry. Flow cytometry analyses of T cells in the brain samples of WT- and KO-infected mice were carried out as described[71]. Mice were anesthetized and transcardially perfused with PBS, and the brain samples were dissected out and harvested in RPMI-1640 medium containing 10% FBS. For preparing single cell suspensions, the samples were minced and digested in RPMI-1640 medium containing 0.05% Collagenase D and 2U/ml DNase I for 30 min at room temperature, and passed through 70 μm nylon cell strainer, followed by 5 min of incubation on ice. Brain homogenates were then overlaid on 30% Percoll cushion and centrifuged at 400 *g* for 20 min at room temperature. The leukocyte pellets obtained were resuspended in 1 ml of RBC lysis buffer (155 mM NH$_4$Cl, 10 mM NaHCO$_3$ and 0.1 mM EDTA; pH 7.3) and incubated on ice for 5 min to remove any residual RBCs. The pellets were then washed with RPMI-1640, counted and stained for various markers. For intracellular markers like TNFα, IFNγ, perforin and granzyme B, staining was carried out after fixing the cells with 2% paraformaldehyde. Single fluorochrome-stained cells were used to compensate for the spectral overlap. Flow cytometry was performed with BD LSRFortessa and CytoFLEX S and the data were analyzed using FlowJo™ v10.6.1. The following fluorescent dye-conjugated antibodies were used for staining: anti-mouse CD3-FITC (clone 17A2; Thermo Fisher Scientific, 11-0032-82; 0.25 μg/10^6 cells in 100 μl volume), anti-mouse CD4-PE (clone RM4-5; Thermo Fisher Scientific, 12-0043-82; 0.125 μg/10^6 cells in 100 μl volume), anti-mouse CD8-PerCP-Cyanine5.5 (clone 53–6.7; Thermo Fisher Scientific, 45-0081-82; 0.25 μg/10^6 cells in 100 μl volume), anti-mouse CD69-Brilliant Violet 421 (clone H1.2F3; BioLegend, 104527; 0.25 μg/10^6 cells in 100 μl volume), anti-mouse CXCR3-PE (clone CXCR3-173; Thermo Fisher Scientific, 12-1831-82; 0.25 μg/10^6 cells in 100 μl volume), anti-mouse Perforin-PE (clone S16009A; Bio-Legend, 154305; 0.50 μg/10^6 cells in 100 μl volume), anti-mouse Granzyme B-APC (clone NGZB; Thermo Fisher Scientific, 17-8898-82; 0.125 μg/10^6 cells in 100 μl volume), anti-mouse IFNγ-eFluor 450 (clone XMG1.2; Thermo Fisher Scientific, 48-7311-82; 0.50 μg/10^6 cells in 100 μl volume), anti-mouse TNFα-eFluor 450 (clone MP6-XT22; Thermo Fisher Scientific, 48-7321-82; 0.25 μg/10^6 cells in 100 μl volume).

FV isolation and analyses. In *P. berghei*, the Hz containing vacuoles tend to remain as small discrete vacuoles until the late schizont stage and they coalesce only at the time of schizont rupture. Because of this, purifying the FVs for *P. berghei* trophozoites is difficult using the standard percoll protocol that is followed for *P. falciparum*, wherein the small vacuoles coalesce in the late ring stages itself. Hence, we resorted ourselves to the isolation of FVs that are released during the schizont rupture as described with slight modifications[72]. Infected blood containing WT or FCKO parasites was collected around 22:00 h, centrifuged at 1000 g for 5 min to remove plasma and buffy coat, and washed twice with RPMI-1640 medium containing 10% FBS. The washed cells were resuspended in 10 volumes of RPMI-1640 medium containing 10% FBS and then incubated at 37 °C for overnight in a CO$_2$ incubator. The maturation of schizonts was monitored by Giemsa

smears and the FVs released in the culture supernatant during schizont rupture were collected in the next day around 09:00 h. In brief, the cultures were centrifuged at 200 g for 5 min to remove the RBCs. After repeating this step twice, the supernatant devoid of RBCs was centrifuged at 400 g for 10 min to collect the FVs that are free of merozoites. The FV pellet was then washed twice with PBS by centrifuging at 3000 g for 3 min and stored at −20 °C. The purity of FVs was tested under microscope with 100x objective.

Microscopy analyses of FV pH, lipid staining, Hz content and Hz dynamics. To examine the LysoTracker Deep Red uptake in the live parasites, 10–20 μl of infected blood was collected from tail vein of the infected mice when the peripheral blood parasitemia was around 5–10% and resuspended in heparinised RPMI-1640 medium containing 10% FBS. After washing twice, the cells were incubated with 100 nM LysoTracker Deep Red (Thermo Fisher Scientific, L12492) for 30 min at 37 °C in RPMI-1640 medium containing 10% FBS. The cells were then washed thrice with RPMI-1640 medium without phenol red, resuspended in the same medium and examined immediately under 100x objective using Olympus IX83 microscope with DP73 high-performance camera at 1600 × 1200 resolution using TRITC filter. BODIPY 493/503 (Thermo Fisher Scientific, D3922) and Nile Red (Sigma-Aldrich, 19123) staining for parasitized RBCs were carried out as described[73]. 10–20 μl of infected mouse blood was collected from the tail vein in Hank's balanced salt solution (HBSS) and centrifuged at 2000 g for 3 min. The cell pellet obtained was resuspended in 200 μl of HBSS containing BODIPY 493/503 (10 μg/ml) or Nile Red (2 μg/ml) and incubated at 37 °C for 30 min. The cells were then washed twice and resuspended in HBSS. The images were acquired under 100x objective using Olympus IX83 microscope with DP73 high-performance camera at 1600 × 1200 resolution using FITC/TRITC filters. The images for WT and KO were acquired under identical exposure conditions and the fluorescent signal intensities were quantified using ImageJ software v1.52a. To examine the Hz content, bright field and DIC images were taken under 100× objective. Live imaging of Hz dynamics was carried out under 100x objective by acquiring 15 frames per second at 1600 × 1200 resolution. The video files were processed using VSDC video editor v6.4.2.108 and VideoPad v4.30 NCH softwares.

Labeling studies with ¹⁴C-ALA, ³²P-orthophosphoric acid and ¹⁴C-SA. [4-¹⁴C]-ALA (ARC 1550), ³²P-orthophosphoric acid (ARC 0103) and [1-¹⁴C]-SA (ARC 025) were procured from American Radiolabeled Chemicals, Inc. The infected blood samples were collected, centrifuged at 1000 g for 5 min to remove plasma and buffy coat, and washed twice with RPMI-1640 medium containing 10% FBS. The washed cells were resuspended in 10 volumes of RPMI-1640 medium containing 10% FBS and then incubated at 37 °C in a CO_2 incubator with the respective radioactive compounds. For ¹⁴C-ALA labeling, blood samples were collected from griseofulvin treated and control WT-infected mice around 16:00 h and the labeling was carried out for 9 h at a radioactivity of 1 μCi/ml. The infected RBCs were then centrifuged, washed with PBS and the parasites were isolated by saponin (Sigma-Aldrich, S4521) treatment. After washing the parasite pellet with PBS for four times, free heme present in the parasites was extracted using ethyl-lacetate:glacial acetate (4:1) followed by 1.5 N HCl and water washes to remove porphyrins and ALA as described[34]. The upper phase was separated, dried under nitrogen stream, dissolved in methanol and analyzed by TLC on silica gel using the mobile phase 2,6-lutidine and water (5 : 3 v/v) in ammonia atmosphere. The intensity of radiolabelling was scanned using Amersham Typhoon 5 Biomolecular Imager by exposing the TLC sheets to phosphorimager screen and the radioactive counts were measured using PerkinElmer MicroBeta² 2450 Microplate Counter. For ³²P-orthophosphoric acid and ¹⁴C-SA labeling, the blood sample collection and incubation were carried out as mentioned for the FV isolation. In addition to the isolation of the secreted FVs, the infected RBC pellets were subjected to saponin treatment for the isolation of the radiolabelled total parasites. The labeling was carried out for ³²P-orthophosphoric acid and ¹⁴C-SA at radioactivities of 50 μCi/ml and 2 μCi/ml, respectively. All these experiments were typically carried out in a total volume of 4 ml, carefully matching in terms of parasitized RBCs and hematocrit between WT and FCKO.

Lipid analyses. Lipid extraction for phospholipid analysis was carried out as described[74]. FV and parasite pellets were extracted with chloroform:methanol (2:1) and washed twice with water. The lower organic phase was collected and analyzed by TLC on silica gel using the mobile phase chloroform:ethanol:water:tri-ethyla-mine (30:35:7:35 v/v). 5 μl of the sample was used to take radioactive counts. For fatty acid analysis, the lipids extracted as mentioned above were dried, dissolved in 50 μl of toluene and subjected to mild methanolysis/methylation by the addition of 375 μl of methanol and 75 μl of 8% HCl in methanol. After incubating at 45 °C for 16 h, FAMEs were extracted by the addition of 250 μl of hexane and 250 μl of water[75]. The hexane layer containing FAMEs was analyzed by TLC on silica gel impregnated with 0.5% methanolic silver nitrate using the mobile phase light petroleum ether:acetone:formic acid (97:2:1 v/v) to separate FAMEs derived from unsaturated fatty acids[76]. In this separation, SAME lacking double bond migrates faster as an uppermost top band followed by OAME and other unsaturated FAMEs that are separated based on their degree of unsaturation and the length of fatty acyl chain. The respective standards were used for all the lipids. 5 μl of the hexane layer

was used to take radioactive counts. For GC-MS analysis, 1 μl of hexane containing the FAMEs was injected in split mode (50:1). The GC-MS analysis was performed using Agilent 7890B GC coupled with 240 Ion Trap MS. The column used for analysis was Agilent VF-5MS (30 m length × 0.25 mm internal diameter (ID) x 0.25 μm film thickness). The oven temperature was programmed from 140 °C (5 min hold), increased at rate of 4 °C/min to 240 °C. Helium was used as carrier gas with 1 ml/min flow rate. The mass spectrometer was operated in full scan mode from 40 to 500 m/z and NIST library search was performed to identify the compounds using Agilent Workstation Software v7.0.1. The set integration parameters of NIST search and identification include peak width value of 4, tangent % value of 10, slope sensitivity (Signal/Noise) value of 50 with peak size reject counts of 5000 and a default threshold of 500.

Proteomics analyses. To examine the protein content of the FVs from WT and FCKO parasites, proteins were extracted from three different preparations of WT and FCKO FVs using 25 mM ammonium bicarbonate containing 6 M urea. The respective WT and FCKO FV protein extracts were pooled separately, followed by treatment with DTT and iodoacetamide. The urea concentration was then reduced to 0.6 M by performing dilution with 25 mM ammonium bicarbonate. For LC-MS/MS, in-solution trypsin (SCIEX) digestion was carried out for 200 μg total protein, followed by sample clean up with Waters Oasis SPE cartridge. The samples were subjected to micro flow reverse-phase LC in Eksigent Ekspert Nano LC 425 system (SCIEX) that was directly connected to a tandem quadrupole time-of-flight SCIEX TripleTOF 5600+ ESI-mass spectrometer. The samples were concentrated using a SCIEX Micro Trap Cartridge (Chrome XP; C18-CL, 5-μm, 120-Å pore size). The trap cartridge was washed with 0.1% (v/v) formic acid and 2% (v/v) acetonitrile in water, and the concentrated peptides were then separated using a SCIEX capillary reverse-phase column (ChromeXP, 3C18-CL-120, 3 μm, 120 Å and 0.3 × 150 mm) at a flow rate of 5 μl/min using the following solvents: solvent A—98% water and 2% acetonitrile containing 0.1% formic acid (v/v), and solvent B—98% acetonitrile and 2% water containing 0.1% formic acid (v/v). The gradient parameters were set at 2 to 50% of solvent B in 28 min, followed by 50 to 90% of solvent B in 1 min, sustaining 90% of solvent B for 3 min and then 90–5% B in 0.5 min with a final re-equilibration with 2% of solvent B for 2.5 min. Mass spectra and tandem mass spectra were recorded in positive-ion and high-sensitivity mode with a full scan resolution of 35,000 (full width at half maximum) and the ion source was operated with the following parameters: IonSpray Voltage Floating (ISVF) = 5500; Ion Source Gas 1 (GS1) = 25; Ion Source Gas 1 (GS2) = 22; Curtain Gas Flow (CUR) = 30. The precursor ions were fragmented in a collision cell containing nitrogen as a collision gas. The calibrations for TOF MS spectra and TOF MS/MS spectra were performed by injecting 100 fmol beta-galactosidase digest (SCIEX). The peptide spectra were recorded over a mass/charge (m/z) range of 350 to 1250, and MS/MS spectra were recorded over an m/z range of 150–1600 in data-dependent acquisition (DDA) mode. Data acquisition was achieved using Analyst TF1.7.1. software and DDA was performed to obtain MS/MS spectra for the 15 most abundant parent ions following each survey MS1 scan (250-ms acquisition time per MS1 scan and 50-ms acquisition time per MS/MS). Dynamic exclusion features were set on an exclusion mass width of 50 mDa and an exclusion duration of 6 s. The acquired MS/MS data were annotated using Paragon algorithm (ProteinPilot Software Version 5.0.2, SCIEX) against the reference proteomes of Plasmodium berghei (UP000074855, Taxonomy 5823; UP000219974, Taxonomy 5821) available at Uniprot (https://www.uniprot.org/) with the following parameters: TripleTOF 5600 instrument; alkylation of cysteines by iodoacetamide; trypsin enzyme digestion; ID Focus on biological modifications and the detected protein threshold [Conf] set at >10%. The mass spectrometry proteomics data of LC-MS/MS have been deposited to the ProteomeXchange Consortium via the PRIDE partner repository with the dataset identifier PXD031736.

Fourplex iTRAQ labeling was carried out as per the manufacturer's protocol (iTRAQ kit, AbSciex, Cat No. 4381664). FVs were solubilized in 0.5 M triethylammonium bicarbonate (TEAB) containing 0.1% sodium dodecyl sulfate (SDS) and 5 mM reducing reagent tris-(2-carboxyethyl) phosphine (TCEP), and incubated at 60 °C for 1 h followed by treatment with methyl methane thiosulfonate (MMTS) for 10 min at room temperature. 50 and 100 μg total protein were used to perform trypsin digestion at 37 °C for 16 h. Two sets of four-plex reactions were carried out for three different preparations of WT and FCKO FVs along with two internal controls. The digested peptides of WT and FCKO FVs were labeled with either 115, 116 or 117 isobaric tag, and isobaric tag 114 was used exclusively to label the internal controls that had equivalent representation of all the samples for normalization. The samples were spiked with bovine serum albumin (BSA) to ensure the loading accuracy. The samples labeled with different isobaric tags were pooled together as one single sample for individual reaction set and vacuum concentrated. After performing sample clean up with Waters Oasis SPE cartridge, the peptides were separated and the mass spectra and tandem mass spectra were recorded as mentioned for LC-MS/MS analysis using Eksigent Ekspert Nano LC 425 system (SCIEX) coupled with a tandem quadrupole time-of-flight SCIEX TripleTOF 5600+ ESI-mass spectrometer. The peptide spectra were recorded over a mass/charge (m/z) range of 350 to 1250, and MS/MS spectra were recorded over an m/z range of 100 to 1600. Protein identification and quantification were performed using Paragon algorithm (ProteinPilot Software Version 5.0.2, SCIEX) with a false discovery rate (FDR) ≤1% against the reference proteome of Mus musculus (UP000000589, Taxonomy 10090)

available at Uniprot (https://www.uniprot.org/). Proteins having peptides identified with 95% confidence or above were considered for further analysis. Proteins were quantified by summing the reporter ion intensities across the spectra matching to each protein and normalizing them with respect to the internal control labeled with isobaric tag 114. The normalized reporter ion intensities were used to calculate the fold changes of α and β chains of mouse hemoglobin in *Pb*FCKO FVs with respect to *Pb*WT FVs. The mass spectrometry proteomics data of iTRAQ have been deposited to the ProteomeXchange Consortium via the PRIDE partner repository with the dataset identifier PXD031738.

Griseofulvin and α,β-arteether treatment in mice. Griseofulvin (Sigma-Aldrich) was prepared by dissolving 1 or 2 mg in 40 µl DMSO and then making up the volume to 200 µl with 10% solutol HS 15 (Sigma-Aldrich) in saline. The mixture was vortexed thoroughly for 10 min to form an emulsion and injected intraperitoneally into the mice. All single dose injections were carried out at 06:00 h and double dose injections were carried out at 06:00 h and 18:00 h for the respective days. Control mice were injected with the solvent. α,β-arteether (E MAL (75 mg/ml); Themis Medicare Ltd) was administered intramuscularly. For experiments involving the combination of α,β-arteether and griseofulvin, α,β-arteether was administered intramuscularly at 06:00 h on day 6, followed by two doses of griseofulvin at 24 h interval (at 09:00 h on day 6 and 7).

In vitro *Pf* culture maintenance and treatment. *Pf* cultures were maintained at 37 °C in RPMI-1640 medium (Gibco, 23400-013) containing 0.5% AlbuMAX-II (Thermo Fisher Scientific, 11021037) using O^{+ve} RBCs of 5% hematocrit under 90% N_2, 5% O_2 and 5% CO_2. Griseofulvin was dissolved in DMSO and added at appropriate concentrations to 5 ml cultures that were synchronized for late rings and early trophozoites with 5% sorbitol (w/v) (Sigma-Aldrich, 240850). The final concentration of DMSO in cultures did not exceed 0.2% (v/v). The initial parasitemia at the time of griseofulvin addition was around 0.5–1%. The cultures were harvested after 72 h when the parasites were predominantly in schizonts and saponin lysis was carried out to isolate the parasites from infected RBCs. ^{14}C-ALA labeling in griseofulvin-treated *Pf* cultures was carried out for 24 h by adding ^{14}C-ALA (1 µCi/ml culture volume) at 48 h post-treatment. ^{14}C-radiolabelled de novo heme present in the parasites was extracted using ethylacetate:glacial acetate (4:1), and heme and Hz analyses were carried out as mentioned for *Pb*. The parasite growth was monitored by performing flow cytometry for the infected RBCs stained with 0.5X SYBR Green I (Thermo Fischer Scientific, S7563) for 30 min at 37 °C and by examining Giemsa smears prepared for the cultures. The *Pf* clinical strains used for griseofulvin treatment were revived from the glycerolyte stocks prepared directly from the patient blood using RPMI-1640 medium containing 10% human O^{+ve} serum. The clinical samples were collected with the approval of Institutional Ethics Committee (IEB) / Institutional Review Board (IRB) (94/HEC/19), Institute of Life Sciences, Bhubaneswar, from febrile patients who visited Ispat General Hospital, Rourkela, India, after obtaining their informed consent. The *Pf* infections were confirmed by microscopic examination of Giemsa-stained thick and thin blood smear, rapid diagnostic test and PCR for *Pf*18S rRNA. *Pf*Cam clinical isolate (IPC 5202) was from a human patient with malaria in Battambang province, western Cambodia. *Pf*K1 was isolated from a patient in Thailand.

Western blot analyses and other procedures. Western analyses were carried out using standard procedures. Brain samples were homogenized in 50 mM Tris-Cl buffer, pH 7.5 containing 5 mM EDTA, 50 mM NaCl, 5 mM DTT, 0.1% Np-40, 50 mM NaF, 1 mM PMSF, 1 mM Na_3VO_4, and 1x Halt Protease Inhibitor Cocktail (Thermo Fisher Scientific), followed by centrifugation at 18,000 *g* for 20 min at 4 °C. The supernatants were collected and quantified for total protein. The following antibodies were used: anti-mouse NF-κB p65 (Thermo Fisher Scientific, 14-6731-81; 1:1000 dilution); anti-mouse Phospho-NF-κB p65 (Ser536) (Thermo Fisher Scientific, MA5-15160; 1:1000 dilution); anti-mouse NLRP3 (Thermo Fisher Scientific, PA5-20838; 1:1000 dilution); anti-mouse Phospho-NLRP3 (Ser295) (Thermo Fisher Scientific, PA5-105071; 1:1000 dilution); anti-mouse Caspase 1 (Thermo Fisher Scientific, 14-9832-82; 1:500 dilution); anti-mouse Cleaved Caspase-1 (Asp296) (Cell Signaling Technology, 89332; 1:1000 dilution); anti-mouse IL-1β (Thermo Fisher Scientific, 701304; 1:250 dilution); anti-mouse Cleaved IL-1β (Cell Signaling Technology, 52718; 1:1000 dilution) and anti-mouse β-Actin (Cell Signaling Technology, 3700; 1:2000 dilution). Blots were developed using Pierce ECL Western Blotting Substrate (Thermo Fisher Scientific). Polyclonal sera raised against recombinant *Pf*FC in mouse and recombinant *Pb*GAPDH in rabbit were used at 1:500 dilution. Polyclonal sera raised against recombinant *Pb*V-type H$^+$ATPase subunits B and G in mouse were used at 1:1000 dilution. The parasite lysates for Western analysis of FC were prepared by resuspending the parasite pellets isolated by saponin lysis in 50 mM Tris pH 8.0 containing 500 mM NaCl, 0.5% Triton X-100 and protease inhibitors, followed by sonication in mice. The lysates were then centrifuged at 15,000 *g* for 20 min at 4 °C and the supernatants were used. For Western analysis of V-type ATPase subunits, parasite and food vacuole pellets were resuspended in 50 mM Tris pH 8.0 containing 1 M NaCl, 1% Triton X-100 and 1x Halt Protease Inhibitor Cocktail, followed by sonication in ice. In vitro cytoadherence studies were performed under static conditions using mouse brain endothelial cell line b.End5 (Sigma-Aldrich, 96091930) pre-stimulated with recombinant mouse TNF-α (50 ng/ml) (Sigma-Aldrich, T7539) for 16 h as

described[77]. Parasitized RBCs infected with *Pb*Control^{Luc} and *Pb*FCKO^{Luc} trophozoites and schizonts expressing m-cherry were purified using Nycodenz density gradient centrifugation. In vitro cytoadherence of parasitized-RBCs was examined after 90 min of incubation with endothelial cells at 37 °C. To assess the parasite load in peripheral circulation, qPCR analyses were carried out using *Pb*GAPDH primers with the total RNA prepared from 100 µl of whole blood collected by retro-orbital bleeding from the infected mice treated with respective drugs. The ΔC_t and $\Delta\Delta C_t$ values for the parasite load were calculated with respect to mouse GAPDH.

Statistical analyses. All the graphs were plotted using GraphPad Prism Version 7.00 software and the statistical analyses were carried out using unpaired Welch's *t*-test (two-sided), two-way ANOVA and log-rank (Mantel–Cox) test. For two-way ANOVA, Tukey test was performed and the multiple comparisons were corrected using statistical hypothesis testing. n.s not signiicant, $*P < 0.05$, $**P < 0.01$, $***P < 0.001$. The non-linear regression fit was carried out for inhibitor versus response curve and the R-squared value was determined using GraphPad Prism Version 7.00 software.

Reporting summary. Further information on research design is available in the Nature Research Reporting Summary linked to this article.

Data availability

References

1. World Health Organization. *World Malaria Report* https://www.who.int/teams/global-malaria-programme/reports/world-malaria-report-2021 (2021).
2. World Health Organization. Severe malaria. *Trop. Med. Int. Health* **19**, 7–131 (2014).
3. Zimmerman, G. A. & Castro-Faria-Neto, H. Persistent cognitive impairment after cerebral malaria: models, mechanisms and adjunctive therapies. *Expert Rev. Anti. Infect. Ther.* **8**, 1209–1212 (2014).
4. Varo, R. et al. Adjunctive therapy for severe malaria: a review and critical appraisal. *Malar. J.* **17**, 47 (2018).
5. de Souza, J. B., Hafalla, J. C., Riley, E. M. & Couper, K. N. Cerebral malaria: why experimental murine models are required to understand the pathogenesis of disease. *Parasitology* **137**, 755–772 (2010).
6. Ghazanfari, N., Mueller, S. N. & Heath, W. R. Cerebral malaria in mouse and man. *Front. Immunol.* **9**, 2016 (2018).
7. Niz, M. D. et al. The machinery underlying malaria parasite virulence is conserved between rodent and human malaria parasites. *Nat. Commun.* **7**, 11659 (2016).
8. Dorovini-Zis, K. et al. The neuropathology of fatal cerebral malaria in Malawian children. *Am. J. Pathol.* **178**, 2146–2158 (2011).
9. Franke-Fayard, B., Fonager, J., Braks, A., Khan, S. M. & Janse, C. J. Sequestration and tissue accumulation of human malaria parasites: can we learn anything from rodent models of malaria? *PLoS Pathog.* **6**, e1001032 (2010).
10. Baptista, F. G. et al. Accumulation of Plasmodium berghei-infected red blood cells in the brain is crucial for the development of cerebral malaria in mice. *Infect. Immun.* **78**, 4033–4039 (2010).
11. Strangward, P. et al. A quantitative brain map of experimental cerebral malaria pathology. *PLoS Pathog.* **13**, e1006267 (2017).
12. Dunst, J., Kamena, F. & Matuschewski, K. Cytokines and chemokines in cerebral malaria pathogenesis. *Front. Cell Infect. Microbiol.* **7**, 324 (2017).
13. Grau, G. E. R. & Wassmer, S. C. In *Malaria: Immune Response to Infection and Vaccination*(eds. Mota, M. M. & Rodriguez, A.) 67–80 (Springer International Publishing, Cham, 2017).
14. Jaramillo, M. et al. Hemozoin-inducible proinflammatory events in vivo: potential role in malaria infection. *J. Immunol.* **172**, 3101–3110 (2004).
15. Olivier, M., Van Den Ham, K., Shio, M. T., Kassa, F. A. & Fougeray, S. Malarial pigment hemozoin and the innate inflammatory response. *Front. Immunol.* **5**, 25 (2014).

16. Gowda, D. C. & Wu, X. Parasite recognition and signaling mechanisms in innate immune responses to malaria. *Front. Immunol.* **19**, 9:3006 (2018).

17. Raulf, M. K. et al. The C-type lectin receptor CLEC12A recognizes Plasmodial hemozoin and contributes to cerebral malaria development. *Cell Rep.* **28**, 30–38.e5 (2019).

18. Eugenin, E. A., Martiney, J. A. & Berman, J. W. The malaria toxin hemozoin induces apoptosis in human neurons and astrocytes: potential role in the pathogenesis of cerebral malaria. *Brain Res.* **1720**, 146317 (2019).

19. Pamplona, A. et al. Heme oxygenase-1 and carbon monoxide suppress the pathogenesis of experimental CM. *Nat. Med.* **13**, 703–710 (2007).

20. Ferreira, A., Balla, J., Jeney, V., Balla, G. & Soares, M. P. A central role for free heme in the pathogenesis of severe malaria: the missing link? *J. Mol. Med. (Berl.).* **86**, 1097–1111 (2008).

21. Ferreira, A. et al. Sickle hemoglobin confers tolerance to Plasmodium infection. *Cell* **145**, 398–409 (2011).

22. Jani, D. et al. HDP-a novel heme detoxification protein from the malaria parasite. *PLoS Pathog.* **4**, e1000053 (2008).

23. Dorn, A., Stoffel, R., Matile, H., Bubendorf, A. & Ridley, R. G. Malarial haemozoin/beta-haematin supports haem polymerization in the absence of protein. *Nature* **374**, 269–271 (1995).

24. Sullivan, D. J. Jr., Gluzman, I. Y. & Goldberg, D. E. Plasmodium hemozoin formation mediated by histidine-rich proteins. *Science* **27**, 219–222 (1996).

25. Bendrat, K., Berger, B. J. & Cerami, A. Haem polymerization in malaria. *Nature* **378**, 138–139 (1995).

26. Fitch, C. D., Cai, G. Z., Chen, Y. F. & Shoemaker, J. D. Involvement of lipids in ferriprotoporphyrin IX polymerization in malaria. *Biochim. Biophys. Acta* **1454**, 31–37 (1999).

27. Amodu, O. K., Adeyemo, A. A., Olumese, P. E. & Gbadegesin, R. A. Intraleucocytic malaria pigment and clinical severity of malaria in children. *Trans. R. Soc. Trop. Med. Hyg.* **92**, 54–56 (1998).

28. Newton, C. R., Taylor, T. E. & Whitten, R. O. Pathophysiology of fatal falciparum malaria in African children. *Am. J. Trop. Med. Hyg.* **58**, 673–683 (1998).

29. Birhanu, M. et al. Hematological parameters and hemozoin-containing leukocytes and their association with disease severity among malaria infected children: a cross-sectional study at Pawe general hospital, Northwest Ethiopia. *Interdiscip. Perspect. Infect. Dis.* **2017**, 8965729 (2017).

30. Dalko, E. et al. Multifaceted role of heme during severe plasmodium falciparum infections in India. *Infect. Immun.* **83**, 3793–3799 (2015).

31. Elphinstone, R. E. et al. Dysregulation of the haem-haemopexin axis is associated with severe malaria in a case–control study of Ugandan children. *Malar. J.* **14**, 511 (2015).

32. Dondorp, A. M. et al. Artesunate versus quinine in the treatment of severe falciparum malaria in African children (AQUAMAT): an open-label, randomised trial. *Lancet* **376**, 1647–5167 (2010).

33. Surolia, N. & Padmanaban, G. De novo biosynthesis of heme offers a new chemotherapeutic target in the human malarial parasite. *Biochem. Biophys. Res. Commun.* **187**, 744–750 (1992).

34. Nagaraj, V. A. et al. Malaria parasite-synthesized heme is essential in the mosquito and liver stages and complements host heme in the blood stages of infection. *PLoS Pathog.* **9**, e1003522 (2013).

35. Nagaraj, V. A. & Padmanaban, G. Insights on heme synthesis in the malaria parasite. *Trends Parasitol.* **33**, 583–586 (2017).

36. Ke, H. et al. The heme biosynthesis pathway is essential for Plasmodium falciparum development in mosquito stage but not in blood stages. *J. Biol. Chem.* **289**, 34827–34837 (2014).

37. Sigala, P. A., Crowley, J. R., Henderson, J. P. & Goldberg, D. E. Deconvoluting heme biosynthesis to target blood-stage malaria parasites. *Elife* **14**, 4 (2015).

38. Bonday, Z. Q., Dhanasekaran, S., Rangarajan, P. N. & Padmanaban, G. Import of host delta-aminolevulinate dehydratase into the malarial parasite: identification of a new drug target. *Nat. Med.* **6**, 898–903 (2000).

39. Dhanasekaran, S., Chandra, N. R., Sagar, B. K. C., Rangarajan, P. N. & Padmanaban, G. Delta-aminolevulinic acid dehydratase from Plasmodium falciparum: indigenous versus imported. *J. Biol. Chem.* **279**, 6934–6942 (2004).

40. Varadharajan, S., Dhanasekaran, S., Bonday, Z. Q., Rangarajan, P. N. & Padmanaban, G. Involvement of delta-aminolaevulinate synthase encoded by the parasite gene in de novo haem synthesis by Plasmodium falciparum. *Biochem. J.* **367**, 321–327 (2002).

41. Padmanaban, G., Nagaraj, V. A. & Rangarajan, P. N. *Handbook of Porphyrin Science. With Applications to Chemistry, Physics, Materials Science, Engineering, Biology and Medicine* (World Scientific Publishing, 2013).

42. Rizopoulos, Z., Matuschewski, K. & Haussiga, J. M. Distinct prominent roles for enzymes of Plasmodium berghei heme biosynthesis in sporozoite and liver stage maturation. *Infect. Immun.* **84**, 3252–3262 (2016).

43. Bushell, E. et al. Functional profiling of a Plasmodium genome reveals an abundance of essential genes. *Cell* **170**, 260–272.e8 (2017).

44. Harding, C. R. et al. Genetic screens reveal a central role for heme biosynthesis in artemisinin susceptibility. *Nat. Commun.* **11**, 4813 (2020).

45. Olafson, K. N., Ketchum, M. A., Rimer, J. D. & Vekilov, P. G. Mechanisms of hematin crystallization and inhibition by the antimalarial drug chloroquine. *Proc. Natl Acad. Sci. USA* **112**, 4946–4951 (2015).

46. Schwarzer, E., Kuhn, H., Valente, E. & Arese, P. Malaria-parasitized erythrocytes and hemozoin nonenzymatically generate large amounts of hydroxy fatty acids that inhibit monocyte functions. *Blood* **101**, 722–728 (2003).

47. Stiebler, R. et al. Unsaturated glycerophospholipids mediate heme crystallization: biological Implications for hemozoin formation in the kissing bug *Rhodnius prolixus. PLoS One* **9**, e88976 (2014).

48. Gratraud, P. et al. Oleic acid biosynthesis in Plasmodium falciparum: characterization of the stearoyl-CoA desaturase and investigation as a potential therapeutic target. *PLoS One* **4**, e6889 (2009).

49. Kloehn, J., Harding, C. R. & Soldati-Favre, D. Supply and demand-heme synthesis, salvage and utilization by Apicomplexa. *FEBS J.* **288**, 382–404 (2020).

50. Lamarque, M. et al. Food vacuole proteome of the malarial parasite Plasmodium falciparum. *Proteom. Clin. Appl.* **2**, 1361–1374 (2008).

51. Hayashi, M. et al. Vacuolar H$^{(+)}$-ATPase localized in plasma membranes of malaria parasite cells, Plasmodium falciparum, is involved in regional acidification of parasitized erythrocytes. *J. Biol. Chem.* **275**, 34353–34358 (2000).

52. Lin, J. et al. Replication of *Plasmodium* in reticulocytes can occur without hemozoin formation, resulting in chloroquine resistance. *J. Exp. Med* **212**, 893–903 (2015).

53. Hopp, C. S. et al. Deletion of the rodent malaria ortholog for falcipain-1 highlights differences between hepatic and blood stage merozoites. *PLoS Pathog.* **13**, e1006586 (2017).

54. World Health Organization. *WHO Model Prescribing Information: Drugs Used in Skin Diseases* https://apps.who.int/iris/bitstream/handle/10665/41975/9241401060.pdf?sequence=1&isAllowed=y (1997).

55. Petersen, A. B., Ronnest, M. H., Larsen, T. O. & Clausen, M. H. The chemistry of griseofulvin. *Chem. Rev.* **114**, 12088–12107 (2014).

56. Sahoo, A. K. & Mahajan, R. Management of Tinea corporis, Tinea cruris, and Tinea pedis: a comprehensive review. *Indian Dermatol Online J.* **7**, 77–86 (2016).

57. Liu, K. et al. A metabolomic perspective of griseofulvin-induced liver injury in mice. *Biochem. Pharmacol.* **98**, 493–501 (2015).

58. Smith, C. M. et al. Griseofulvin impairs intraerythrocytic growth of Plasmodium falciparum through ferrochelatase inhibition but lacks activity in an experimental human infection study. *Sci. Rep.* **7**, 41975 (2017).

59. Jaramillo, M., Godbout, M. & Olivier, M. Hemozoin induces macrophage chemokine expression through oxidative stress-dependent and -independent mechanisms. *J. Immunol.* **174**, 475–484 (2005).

60. Mandala, W. L. et al. Cytokine profiles in Malawian children presenting with uncomplicated malaria, severe malarial anemia, and cerebral malaria. *Clin. Vaccin. Immunol.* **24**, e00533–16 (2017).

61. Sorensen, E. W. et al. CXCL10 stabilizes T cell-brain endothelial cell adhesion leading to the induction of cerebral malaria. *JCI Insight* **3**, 98911 (2018).

62. Deroost, K., Pham, T. T., Opdenakker, G. & Van den Steen, P. E. The immunological balance between host and parasite in malaria. *FEMS Microbiol. Rev.* **40**, 208–257 (2016).

63. Abshire, J. R., Rowlands, C. J., Ganesan, S. M., So, P. T. & Niles, J. C. Quantification of labile heme in live malaria parasites using a genetically encoded biosensor. *Proc. Natl Acad. Sci. Usa.* **114**, E2068–E2076 (2017).

64. Oh, Y. J. et al. Cytochrome b5 reductase 1 triggers serial reactions that lead to iron uptake in plants. *Mol. Plant* **9**, 501–513 (2016).

65. Antonny, B., Vanni, S., Shindou, H. & Ferreira, T. From zero to six double bonds: phospholipid unsaturation and organelle function. *Trends Cell Biol.* **25**, 427–436 (2015).

66. Riggle, B. A., Miller, L. H. & Pierce, S. K. Desperately seeking therapies for cerebral malaria. *J. Immunol.* **204**, 327–334 (2020).

67. Carroll, R. W. et al. A rapid murine coma and behavior scale for quantitative assessment of murine cerebral malaria. *PLoS One* **5**, e13124 (2010).

68. Tripathi, A. K., Khan, S. I., Walker, L. A. & Tekwani, B. L. Spectrophotometric determination of de novo hemozoin/beta-hematin formation in an in vitro assay. *Anal. Biochem.* **325**, 85–91 (2004).

69. Deroost, K. et al. Improved methods for haemozoin quantification in tissues yield organ-and parasite-specific information in malaria-infected mice. *Malar. J.* **11**, 166 (2012).

70. Dende, C. et al. Nanocurcumin is superior to native curcumin in preventing degenerative changes in experimental cerebral malaria. *Sci. Rep.* **7**, 10062 (2017).

71. Ryg-Cornejo, V., Ioannidis, L. J. & Hansen, D. S. Isolation and analysis of brain-sequestered leukocytes from Plasmodium berghei ANKA-infected mice. *J. Vis. Exp.* **71**, 50112 (2013).

72. Dasari, P. et al. Digestive vacuoles of Plasmodium falciparum are selectively phagocytosed by and impair killing function of polymorphonuclear leukocytes. *Blood* **118**, 4946–4956 (2011).

73. Palacpac, N. M. Q. et al. Developmental-stage-specific triacylglycerol biosynthesis, degradation and trafficking as lipid bodies in Plasmodium falciparum-infected erythrocytes. *J. Cell. Sci.* **117**, 1469–1480 (2004).

74. Deranieh, R. M., Joshi, A. S. & Greenberg, M. L. Thin-Layer chromatography of phospholipids. *Methods Mol. Biol.* **1033**, 21–27 (2013).

75. Ichihara, K. & Fukubayashi, Y. Preparation of fatty acid methyl esters for gas-liquid chromatography. *J. Lipid Res.* **51**, 635–640 (2010).

76. Nikolova-Damyanova, B. & Momchilova, S. Silver ion thin-layer chromatography of fatty acids. A survey. *J. Liq. Chromatogr. Relat. Technol.* **24**, 1447–1466 (2001).

77. El-Assaad, F. et al. Cytoadherence of Plasmodium berghei-infected red blood cells to murine brain and lung microvascular endothelial cells in vitro. *Infect. Immun.* **81**, 3984–3991 (2013).

78. Nagaraj. V. A. Malaria parasite heme biosynthesis promotes and griseofulvin protects against cerebral malaria in mice. *figshare* https://doi.org/10.6084/m9.figshare.19354475 (2022).

Author contributions

M.C., A.A., S.G., R.D., S.B., S.J., A.R.S., and V.A.N. performed the experiments. G.P. and V.A.N. conceived and designed the study. M.C., A.A., S.G., R.D., A.R.S., G.P., and V.A.N. analyzed the data. M.C., A.A., S.G., G.P., and V.A.N. wrote the manuscript.

Competing interests

The authors declare no competing interests.

Additional information

Supplementary information The online version contains supplementary material available at https://doi.org/10.1038/s41467-022-31431-z.

Correspondence and requests for materials should be addressed to Viswanathan Arun Nagaraj.

Peer review information *Nature Communications* thanks the anonymous reviewers for their contribution to the peer review of this work.

Reprints and permission information is available at http://www.nature.com/reprints

Publisher's note Springer Nature remains neutral with regard to jurisdictional claims in published maps and institutional affiliations.

Article

Distinct evolution of type I glutamine synthetase in *Plasmodium* and its species-specific requirement

Sourav Ghosh [1,2], Rajib Kundu[1,2,9], Manjunatha Chandana[1,3,9], Rahul Das[1,2], Aditya Anand[1,2], Subhashree Beura[1], Ruchir Chandrakant Bobde[1,2], Vishal Jain[1], Sowmya Ramakant Prabhu[4], Prativa Kumari Behera[5], Akshaya Kumar Mohanty[1,5], Mahabala Chakrapani [6], Kapaettu Satyamoorthy [7], Amol Ratnakar Suryawanshi[1], Anshuman Dixit[1], Govindarajan Padmanaban[8] & Viswanathan Arun Nagaraj [1] ✉

Malaria parasite lacks canonical pathways for amino acid biosynthesis and depends primarily on hemoglobin degradation and extracellular resources for amino acids. Interestingly, a putative gene for glutamine synthetase (GS) is retained despite glutamine being an abundant amino acid in human and mosquito hosts. Here we show *Plasmodium* GS has evolved as a unique type I enzyme with distinct structural and regulatory properties to adapt to the asexual niche. Methionine sulfoximine (MSO) and phosphinothricin (PPT) inhibit parasite GS activity. GS is localized to the parasite cytosol and abundantly expressed in all the life cycle stages. Parasite GS displays species-specific requirement in *Plasmodium falciparum* (*Pf*) having asparagine-rich proteome. Targeting *Pf*GS affects asparagine levels and inhibits protein synthesis through eIF2α phosphorylation leading to parasite death. Exposure of artemisinin-resistant *Pf* parasites to MSO and PPT inhibits the emergence of viable parasites upon artemisinin treatment.

Malaria parasites have lost de novo pathways for amino acid biosynthesis and retained only a few transaminases and enzymes functioning at the junction of nitrogen and carbon metabolism[1–4]. The asexual stage parasites acquire hemoglobin (Hb) from host RBCs and degrade it in the acidic food vacuole (FV) containing various proteases[5]. Hb degradation caters to amino acid requirements and provides space for the parasites to grow. The only amino acid that is absent in human Hb is isoleucine. In vitro cultures of *P. falciparum* (*Pf*) can be maintained continuously by providing isoleucine as the sole

amino acid in the culture medium, suggesting that the other amino acids released from Hb degradation are adequate to support asexual growth[6]. Unlike the intracellular development of asexual stages in RBCs, sexual stage development in mosquitoes that spans around 12–18 days is extracellular. Starting from the egress of gametocytes, the zygotes, ookinetes, oocysts, and sporozoites depend primarily on extracellular sources of amino acids that are derived from the ingested blood meal and present in the hemolymph. When the sporozoites invade hepatocytes and undergo exo-erythrocytic schizogony, they

[1]Infectious Disease Biology, Institute of Life Sciences, Bhubaneswar 751023 Odisha, India. [2]Regional Centre for Biotechnology, Faridabad 121001 Haryana, India. [3]School of Biotechnology, Kalinga Institute of Industrial Technology, Bhubaneswar 751024 Odisha, India. [4]Department of Biotechnology, Manipal School of Life Sciences, Manipal Academy of Higher Education, Manipal 576104 Karnataka, India. [5]Ispat General Hospital, Sector 19, Rourkela 769005 Odisha, India. [6]Department of Medicine, Kasturba Medical College, Mangalore, Manipal Academy of Higher Education, Manipal 576104 Karnataka, India. [7]Department of Cell and Molecular Biology, Manipal School of Life Sciences, Manipal Academy of Higher Education, Manipal 576104 Karnataka, India. [8]Department of Biochemistry, Indian Institute of Science, Bangalore 560012 Karnataka, India. [9]These authors contributed equally: Rajib Kundu, Manjunatha Chandana. ✉e-mail: arun@ils.res.in

may have to depend on host hepatocyte reserves and/or extracellular sources for amino acids[7,8]. Further, sexual and liver stages do not seem to have FV and therefore, lack the machinery for host protein degradation[9]. Malaria parasite undergoes rapid proliferation in the human and mosquito hosts to generate asexual and liver-stage merozoites, and sporozoites. Intriguingly, the parasite accomplishes it by utilizing the amino acids mainly from human and mosquito resources.

Glutamine is required for carbamoyl phosphate and cytidine triphosphate (CTP) synthesis in the de novo pyrimidine pathway of malaria parasite catalyzed by cytosolic carbamoyl phosphate synthetase II and CTP synthetase, respectively[4,10]. Although the parasite lacks de novo purine synthesis and possesses hypoxanthine-guanine phosphoribosyltransferase (HGPRT) to salvage host purines, it has retained guanosine monophosphate synthetase (GMPS) for which, glutamine serves as an amide donor[11,12]. Glutamine is also utilized by glutamine-fructose-6-phosphate transaminase of hexosamine pathway to generate uridine diphosphate N-acetylglucosamine (UDP-GlcNAc) required for glycoprotein, proteoglycan and glycolipid biosynthesis[13]. In vitro metabolic labeling studies of Pf asexual and sexual stages carried out with ^{13}C-glutamine in the culture medium have suggested a flux of glutamine-derived carbon skeletons into TCA cycle that can possibly lead to the generation of reducing equivalents[14]. Glutamine serves as an amide nitrogen donor for asparagine synthesis as well. Interestingly, glutamine is the most abundant amino acid in human blood with plasma concentrations around 0.5 mM[15]. The asexual stages and gametocytes can also utilize extracellular glutamine as evident from stable isotope labeling studies[14]. In addition, they can acquire glutamine derived from Hb degradation in the FV[6]. Glutamine is also abundant in the mosquito hemolymph[16] and it represents 40–60% of the total amino acids in human liver tissue[15]. Despite the abundance of glutamine in the host milieu and the ability to access Hb-derived and extracellular glutamine, parasite has retained a putative gene for glutamine synthetase (GS) that is conserved across the *Plasmodium* species infecting humans, primates, rodents and birds[17]. This has prompted us to examine the functional significance of GS in malaria parasites. Here, we show parasite GS is enzymatically active and it belongs to a unique type I enzyme that has evolved in a distinct manner. It is expressed in the cytosol of all the stages of parasite life cycle. By utilizing in vitro cultures of Pf for asexual stages and gametocytes, and *P. berghei* (Pb) as an in vivo rodent parasite model for the entire life cycle, we show the species-specific differences in GS requirement in the asexual stages of *Plasmodium* and validate them with clinical samples of Pf and *P. vivax* (Pv) from malaria-infected individuals. Finally, we show the effect of inhibiting GS in artemisinin (ART)-resistant Pf strain. All these findings have implications in developing therapeutic strategies for Pf - the deadliest human parasite responsible for more than 90% of global malaria infections.

Results

### *Plasmodium* GS I is enzymatically active

GS can be classified into three types: I, II and III based on the sequence and structural conformation (Supplementary Discussion). *Plasmodium* genome has a putative, single-copy gene for GS. Multiple sequence alignment suggested that *Plasmodium* GS is a type I enzyme showing ~50% similarity and ~30% identity with respect to GS I of *Mycobacterium tuberculosis* (*Mt*), *Salmonella typhimurium* (*St*), and *Helicobacter pylori* (*Hp*) (Fig. 1a). The sequence length of *Plasmodia* GS is around 540 amino acids, ~60–70 amino acids more than a typical GS I. This can be attributed to two different peptide inserts representing 174–196 and 443–480 amino acids (numbers represent the positions in *Pf*GS) spanning across the regions that are not directly associated with the substrate-binding and catalytic sites. Further, GS I can be classified into two subtypes based on the regulatory mechanisms - Iα that is regulated through the feedback inhibition by glutamine, adenosine monophosphate (AMP) and other amino acids like serine, alanine and glycine,

and Iβ that is additionally inhibited by adenylylation of a tyrosine residue near the active site and not feedback-inhibited by glutamine[18–21]. The characteristic features of GS Iβ are the presence of a specific ~25 amino acid insertion and an adenylylation site with a conserved tyrosine residue (Fig. 1a) that are absent in GS Iα (Supplementary Fig. 1a). Interestingly, the sequence corresponding to 25-amino acid insertion in *Plasmodia* GS is diverged from other organisms and it is flanked by the first peptide insert. Further, *Plasmodia* GS seem to lack a tyrosine residue in the corresponding position of adenylylated tyrosine in St and MtGS, flanked by the second peptide insert towards the C-terminus (Fig. 1a). Besides these differences, key amino acid residues of catalytic and flexible loops constituting the 'bifunnel' active site existing between the adjacent monomers, and residues interacting with metal and ammonium ions, water molecules, ATP and glutamate are conserved in *Plasmodia* GS[19,20] (Fig. 1a). Cryo-electron microscopy (cryoEM) of parasite GS has suggested a classical dodecameric GS I structure composed of two hexamers stacked face-to-face[22]. While the first peptide insert that comes in proximity to the pore of the hexamer ring forming dodecamer channel could not be observed in the cryoEM structure, the second peptide insert forms a long loop that folds down in the opposite direction from the active site. Based on the structure of PfGS, we modeled the monomeric and oligomeric structures for Pb and Pv GS, and the peptide inserts specific for *Plasmodia GS* are represented (Fig. 1b). Our modeled structures of *Plasmodia* GS showed the presence of dodecamer channel with a compact pore arising due to the first peptide insert. For comparison, monomeric and oligomeric structures of MtGS are shown (Fig. 1c) along with the superimposed images of Pf, Pb, and Pv GS monomers with MtGS monomer (Supplementary Fig. 1b). All these evidences suggest that parasite GS belongs to type I enzyme of prokaryotic origin with unique structural features arising out of two peptide inserts that are absent in other GS I. A similar signature is present in GS of *Hepatocystis* (Supplementary Fig. 1c), the closest relative of *Plasmodium* under the phylum Apicomplexa having an analogous life cycle[17].

Studies on *Plasmodium* biology are widely carried out using Pf - a human parasite maintained in vitro, and Pb (or *P. yoelii*) - an in vivo rodent parasite model. We sought to understand the functional significance of GS using Pf and Pb, and checked whether Pf and Pb GS are enzymatically active. GS catalyzes the synthesis of glutamine by incorporating ammonia into glutamate with concomitant ATP hydrolysis. In the presence of divalent cations such as Mg^{2+} or Mn^{2+}, the terminal phosphate from ATP is transferred to glutamate resulting in γ-glutamyl phosphate, which is subsequently attacked by ammonia to form glutamine (Fig. 2a). The purified recombinant (r) Pf and Pb GS with N-terminal His-tag expressed in *E. coli* showed molecular weight of around ~65 kDa in SDS-PAGE (Fig. 2b, c). HPLC analyzes of purified proteins incubated with glutamate, ammonia, ATP and $MgCl_2$ showed the formation of glutamine (Fig. 2d). The specific activity and catalytic efficiency (K_{cat}/K_m) were found to be 1.12 ± 0.17 µmol mg^{-1}min^{-1} and $1.92 \pm 0.29 \times 10^4$ M^{-1}S^{-1} for rPfGS, and 1.35 ± 0.47 µmol mg^{-1}min^{-1} and $0.96 \pm 0.33 \times 10^4$ M^{-1}S^{-1} for rPbGS, respectively (Supplementary Fig. 2a, b). Since GS can also exhibit activity in the presence of $MnCl_2$, enzyme assays were performed with 0.5–50 mM $MnCl_2$ concentrations. While the optimal activity for parasite GS was obtained with 5 mM $MnCl_2$, it was almost 25–30% less when compared with $MgCl_2$ suggesting that $MgCl_2$ is the preferred metal ion cofactor (Supplementary Fig. 2c). For comparison, we expressed and purified r*E. coli* GS I under identical conditions, and performed the assays (Supplementary Fig. 2d–f). All these data suggest that parasite GS can catalyze the synthesis of glutamine.

Inhibition and regulation of *Plasmodium* GS activity

L-Methionine sulfoximine (MSO) is a potent irreversible inhibitor of GS. MSO-phosphate generated through the phosphorylation of MSO by GS serves as a transition state analogue that binds non-
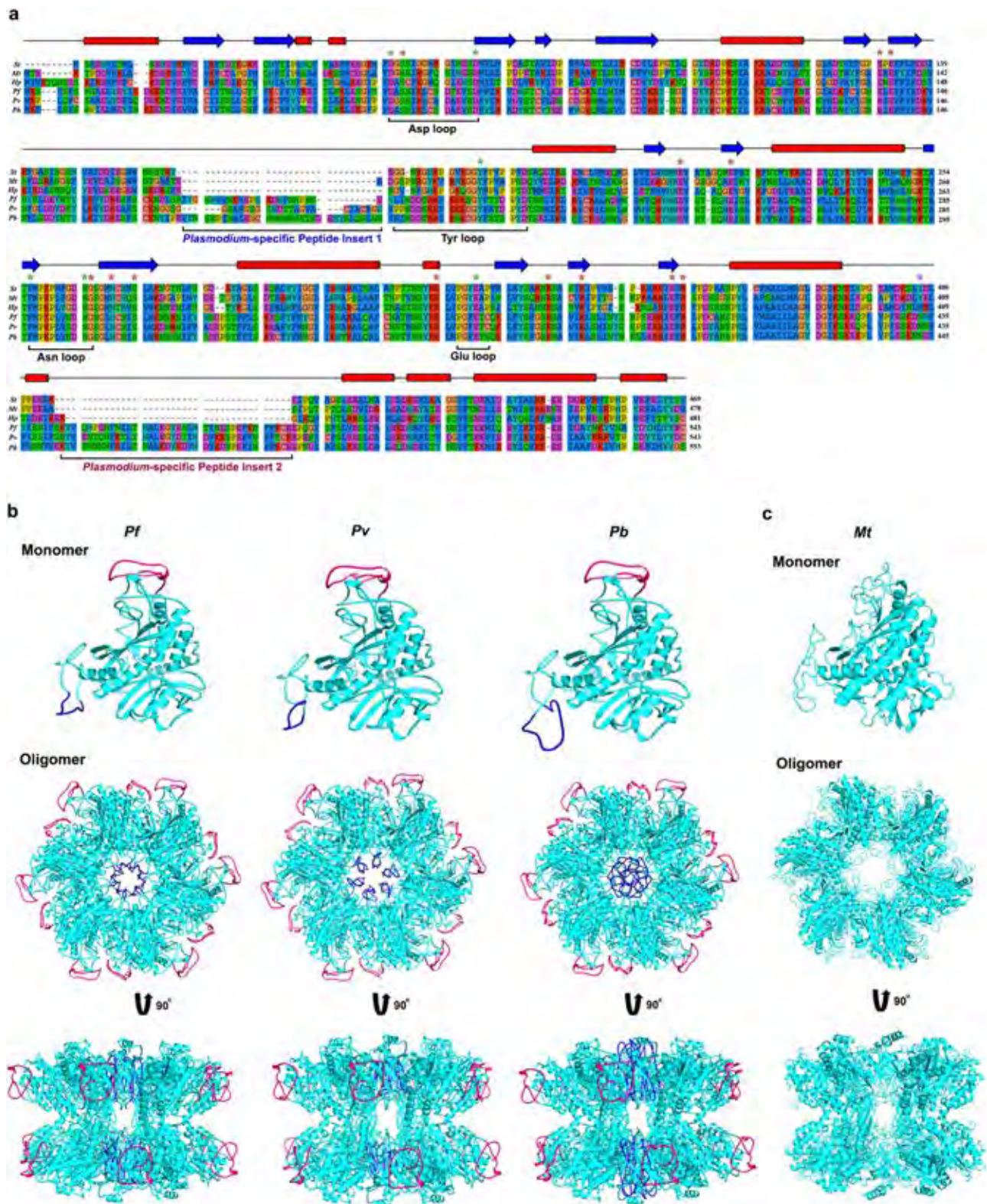
Fig. 1 | Multiple sequence alignment and homology modeling of *Plasmodia* GS.
a Multiple sequence alignment of *Plasmodia* GS (*Pf*, *Pv* and *Pb*) with type I GS of *Mt*, *St* and *Hp*. The alignment was carried out with SeaView Version 3.2 (http://pbil.univ-lyon1.fr/software/seaview3). The secondary structures predicted as α-helices and β-strands are represented as red cylinders and blue arrows, respectively. The conserved amino acid residues in the catalytic and flexible loops of 'bifunnel' active site - Asp59 and Asp73 present in the aspartate loop, Tyr212 present in the tyrosine loop, Phe287 and Asn296 present in the asparagine loop, and Glu361 present in the glutamate loop are highlighted with green asterisks. The residues that are involved

in the substrate and ligand interactions - Ser61, Glu137, Glu139, Glu245, Glu252, Gly297, His301, Ser305, Arg355, Arg373, Arg378, Glu393 and Arg395 are highlighted with brown asterisks. The tyrosine residue that undergoes adenylylation in *Mt* and *St* GS are highlighted with pink asterisk. **b** Monomeric and oligomeric structures of *Pf*, *Pv* and *Pb* GS. *Pv* and *Pb* GS structures were modeled based on the cryoEM structure of *Pf* GS (PDB ID: 6PEW). *Plasmodia* GS-specific peptide inserts are represented in blue (Insert 1) and red (Insert 2). **c** Monomeric and oligomeric structures of *Mt* GS (PDB ID: 2WGS).
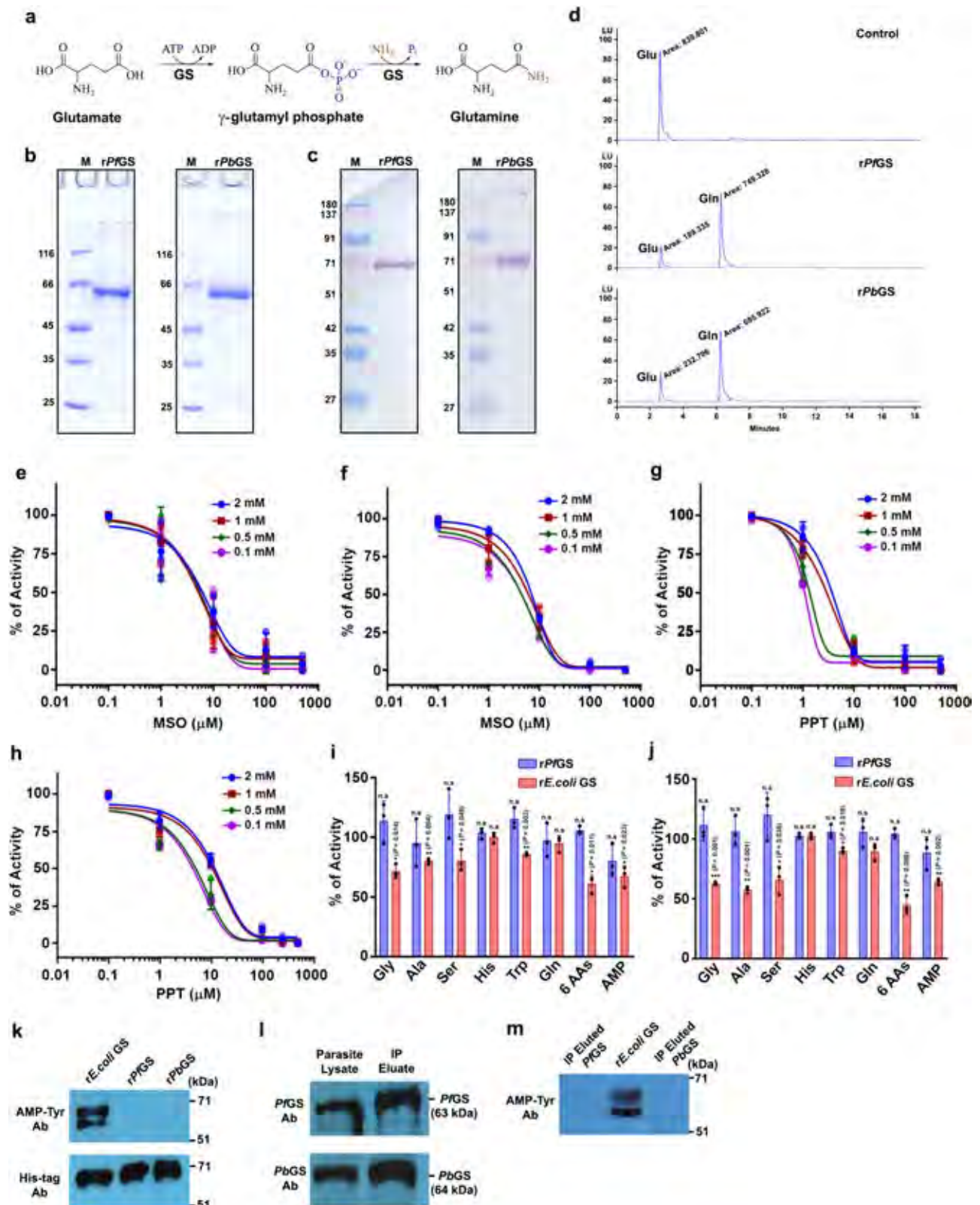
covalently and stabilizes the flexible loop of GS active site thereby, preventing glutamate entry. In addition, methyl group of MSO-phosphate occupies the ammonium binding site to prevent further reaction[23, 24]. While MSO can inhibit both GS I and II, K_i values reported for GS I are ~10^2 times lower when compared with GS II[25,26]. Kinetic studies showed that the parasite GS is sensitive to MSO inhibition like other GS I with K_i values of 5.64 ± 0.39 μM and

5.44 ± 1.07 μM for rPf and PbGS, respectively (Fig. 2e, f). Phosphinothricin (PPT; also known as glufosinate), widely used as a broad-spectrum herbicide, is another potent irreversible inhibitor whose mechanism of inhibition is similar to that of MSO[27]. While the sensitivity of bacterial GS to PPT is similar to that of MSO, plant GS is more sensitive to PPT than MSO[26–30]. Parasite GS is equally sensitive to PPT and the respective K_i values obtained for rPf and PbGS were

Fig. 2 | Inhibition and regulation of *Plasmodium* GS. a Schematic representation of GS enzymatic reaction. **b,c** Coomassie gel pictures of r*Pf*GS and r*Pb*GS purified using Ni^{2+}-NTA resin and their Western blot analysis using anti-his tag antibodies, respectively. Lane M: Protein molecular weight marker (kDa). **d** HPLC chromatogram of r*Pf*GS and r*Pb*GS enzyme assays. **b**–**d** $n = 3$ independent experiments. **e, f** Effect of MSO on r*Pf*GS and r*Pb*GS activity, respectively. **g, h** Effect of PPT on r*Pb*GS and r*Pb*GS activity, respectively. Percentage of activities (mean ± SD) with respect to the control (without inhibitor) are shown and the assays were independently carried out with 0.1, 0.5, 1.0, and 2.0 mM concentrations of glutamate. $n = 3$ independent protein preparations. **i, j** Comparison of the feedback inhibition of r*Pf*GS and r*E.coli* GS in the presence of MgCl$_2$ at 1 mM (**i**) and 5 mM (**j**) concentrations of amino acids and AMP. "6AAs" represents the mixture of all the six amino acids. For "6AAs" of 5 mM concentration, tryptophan alone was used at 2.5 mM concentration because of its limited solubility and the rest were used at

5 mM concentration. The percentage of activities with respect to the control (without feedback inhibitor) are shown (mean ± SD; n.s - not significant, *$P < 0.05$, **$P < 0.01$, ***$P < 0.001$, unpaired *t*-test; two-sided). $n = 3$ independent protein preparations. **k** Western blot analysis of r*Pf*GS, r*Pb*GS and r*E.coli* GS adenylylation with anti-AMP-tyrosine antibody. The doublet was observed for r*E.coli* GS could be because of the oligomerization of r*E.coli* GS having ~3 kDa higher molecular weight due to the presence of histidine tag and enterokinase recognition and cleavage sites, with endogenous *E. coli* GS. **l** Western blot analysis of endogenous GS immunoprecipitated from *Pf* and *Pb* parasite lysates. 15 μl of 150 μl parasite lysates and 10 μl of 30 μl immunoprecipitation eluates were used. **m** Western blot analysis of adenylylation in immunoprecipitated *Pf*GS and *Pb*GS. r*E.coli* GS was used as a control. 0.1 μg of eluted protein was used. IP - immunoprecipitation. **k**–**m** $n = 2$ independent experiments. For **e**–**h** individual data points are shown with respective light-shaded colors. Source data are provided as a Source Data file.

2.31 ± 1.10 μM and 8.07 ± 3.31 μM (Fig. 2g, h). These data indicate that parasite GS can be inhibited by transition state analogs.

To examine whether parasite GS is regulated by feedback inhibition through end products of glutamine metabolism, we performed enzyme assays with 1 and 5 mM concentrations of glycine, serine, alanine, tryptophan, histidine, glutamine and AMP. *E. coli* GS Iβ is inhibited by alanine, glycine, serine, and tryptophan in the presence of MgCl$_2$[31]. *Bs*GS Iα is inhibited almost completely by AMP and glutamine in the presence of MnCl$_2$[32]. Similar inhibition by alanine, glycine and serine has been reported for type II rat GS as well[33]. Interestingly, none of the amino acids either tested individually or in a cumulative manner could significantly inhibit r*Pf*GS activity in the presence of MgCl$_2$. The inhibition with AMP was also not significant with respect to the control. For comparison, assays were performed with *E. coli* GS. As reported earlier, *E. coli* GS showed 20–30% inhibition for glycine, alanine, serine, and AMP, and 10% inhibition for tryptophan at 1 mM concentration. There was almost 30–40% inhibition for glycine, alanine, serine, and AMP at 5 mM concentration (Fig. 2i, j). Further, glutamine serves as a strong feedback inhibitor for GS 1α, but not for Iβ[32,34]. In agreement, *E. coli* and r*Pf*GS activities were not inhibited by glutamine even at a 5 mM concentration (Fig. 2j). Since the effect of inhibitors can vary with the metal ion cofactors[32], we performed r*Pf*GS assays in the presence of MnCl$_2$ as well. Again, none of the amino acids tested could inhibit the activity, and a moderate inhibition of around 25% was observed only for 5 mM AMP (Supplementary Fig. 3a). Similar results were obtained for r*Pb*GS with respect to amino acids and there was a moderate inhibition by AMP in the presence of MgCl$_2$ and MnCl$_2$ (Supplementary Fig. 3b, c). Another salient feature of type Iβ GS is its regulation by adenylylation[35,36]. Interestingly, Western analysis using anti-AMP-tyrosine antibody showed that both r*Pf* and r*Pb* GS do not undergo adenylylation, although *E. coli* GS exhibits adenylylation (Fig. 2k). This was also confirmed by performing immunoprecipitation for endogenous GS from *Pf* and *Pb* parasite lysates, wherein, adenylylation could not be detected (Fig. 2l, m). These results suggest that parasite GS is unique and it lacks the characteristic regulatory mechanisms of GS 1α or 1β.

Functional significance of *Plasmodium*-specific peptide inserts
To understand the functional significance of *Plasmodium* GS-specific peptide inserts, we performed independent deletions for first (ΔI$_1$r*Pf*GS) and second peptide inserts (ΔI$_2$r*Pf*GS) of r*Pf*GS (Fig. 3a; Supplementary Fig. 3d, e), and examined their activities. ΔI$_1$r*Pf*GS behaved like r*Pf*GS in terms of specific activity (Fig. 3b), inhibition by MSO and PPT (Fig. 3c), and lack of feedback inhibition by amino acids (Fig. 3d). Since the first peptide insert occupying hexamer pore of the dodecameric channel renders it more compact than GS I of other organisms (Fig. 3e), we were interested in examining the stability of ΔI$_1$r*Pf*GS. While the activity of ΔI$_1$r*Pf*GS was comparable with r*Pf*GS when exposed to higher concentrations of urea or NaCl (Supplementary Fig. 3f, g), ΔI$_1$r*Pf*GS was thermally less stable. Exposure of ΔI$_1$r*Pf*GS to increased temperatures in the febrile range of 37 °C to 42 °C for one

hour could lead to visible precipitation and almost 80% reduction in its activity in comparison with ~30% reduction observed for r*Pf*GS (Fig. 3f). Size-exclusion chromatography examining the oligomeric status showed the dissociation of oligomers when ΔI$_1$r*Pf*GS was exposed to 37 °C or 42 °C for 15 min (Fig. 3g–i). Interestingly, deletion of the second peptide insert (ΔI$_2$r*Pf*GS) led to loss of enzyme activity under various conditions that were tested (Fig. 3b). For additional insights, we performed all-atom molecular dynamics (MD) simulations for the two adjacent subunits constituting the active site from upper and lower hexamers of *Pf*GS and ΔI$_2$*Pf*GS. A comparison of intra-chain and inter-chain hydrogen bonds of one subunit suggested 25 and 12 interactions that were unique for *Pf*GS and ΔI$_2$*Pf*GS, respectively (Fig. 3j). This also included some of the residues that are directly associated with the enzyme activity (Supplementary Data 1). Interestingly, of the 25 unique interactions in *Pf*GS, only two of them were from the second peptide insert. The analyzes of MD simulations showed changes in the overall protein conformation (Fig. 3k) with deviations in C$_\alpha$ backbone, residue flexibility, hydrogen bond formation, and solvent accessible surface area (SASA) (Supplementary Fig. 3h–k). As observed for ΔI$_2$r*Pf*GS, r*Pf*GS lacking both the inserts (ΔI$_1$I$_2$r*Pf*GS) was also found to be inactive (Supplementary Fig. 3l). These results suggest that the evolution of the second peptide insert has occurred with compensatory structural changes in *Pf*GS that affect *Pf*GS activity when the second peptide insert was deleted.

Plasmodium GS is cytosolic and expressed in the entire life cycle
We examined the expression and localization of native GS, and its activity in the parasite. Western analyzes carried out for *Pf* lysates having equal number of synchronized rings, trophozoites and schizonts using *Pf*GS antibodies showed GS expression in all the asexual stages (Fig. 4a). Similarly, GS expression could be detected in the lysates of *Pb* asexual stages (Fig. 4b). Immunofluorescence analyzes showed an abundant cytosolic localization wherein, the fluorescence signal was observed all over the parasite in rings, trophozoites and schizonts (Fig. 4c). This was in agreement with the absence of any predictable signal sequence in the parasite GS[17]. Enzyme assays to assess the functionality of native GS in asexual stages showed a GS activity of around 0.21 and 0.29 nmol mg^{-1} total protein min^{-1} for *Pf* and *Pb* lysates, respectively (Fig. 4d). Further, GS expression was detected in *Pf* and *Pb* gametocytes (Fig. 4e, f). Given the safety constraints associated with performing sexual stage development of *Pf* in mosquitoes, we utilized *Pb* to examine GS expression in these stages. Immunofluorescence analyzes for the sexual stage development of *Pb* in *Anopheles stephensi* mosquitoes showed GS expression in ookinete, oocyst and sporozoite stages (Fig. 4g–i). GS expression could also be detected for in vitro exo-erythrocytic stages of *Pb* when the sporozoites from infected mosquitoes were allowed to infect immortalized human hepatocyte cell line HC-04 (Fig. 4j). All these evidences suggest that native parasite GS is cytosolic and active, and abundantly expressed in all the stages of the parasite life cycle.
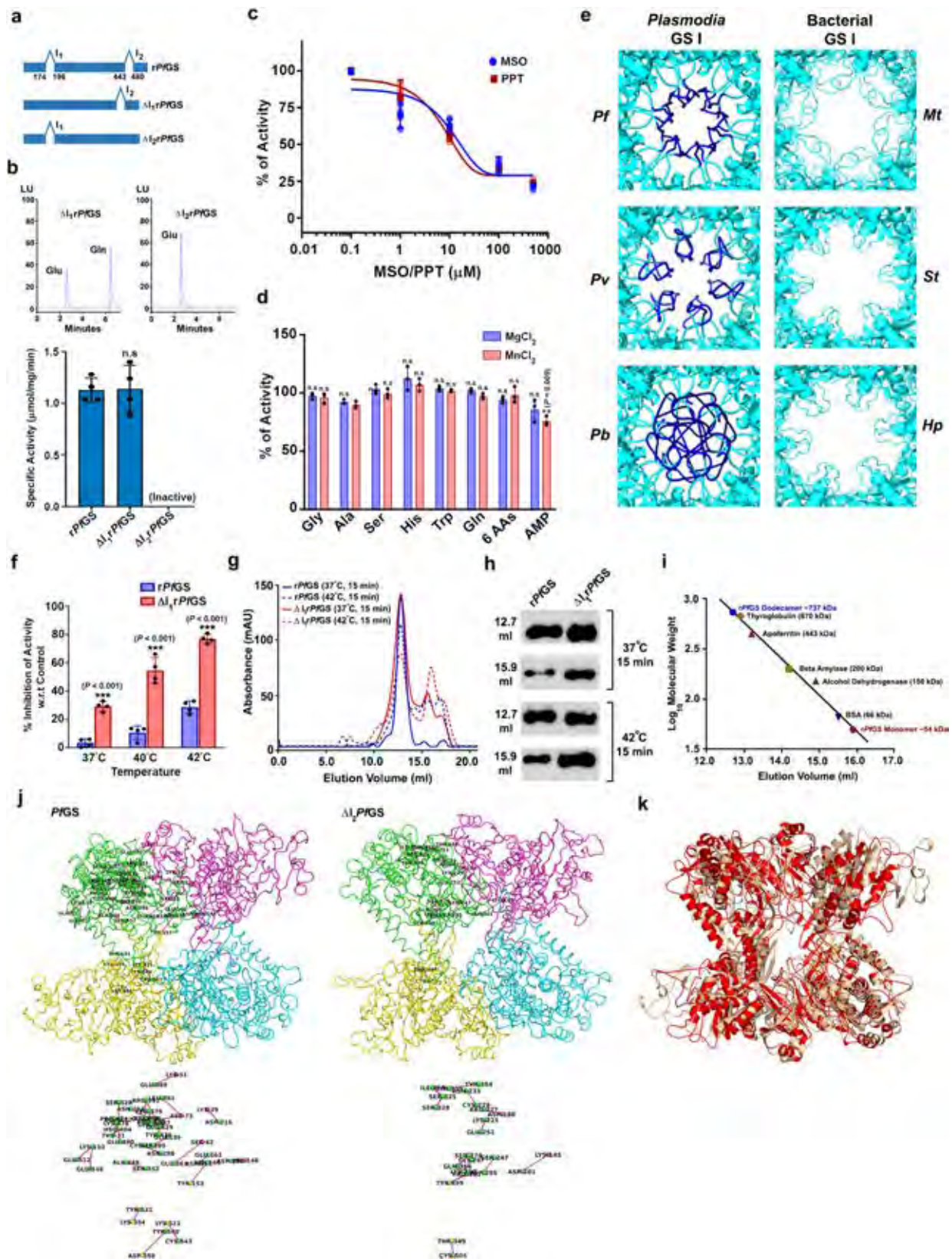
GS is required for the optimal development of *Pf* asexual and gametocyte stages

Our next interest was to understand the significance of GS in asexual and gametocyte stages of *Pf*. Repeated attempts to generate GS knockout (KO) in *Pf* using conventional double crossover recombination, selection-linked integration and CRISPR-Cas9 approaches turned out to be unsuccessful. Therefore, we generated a conditional, mis-localizing, knock sideways (cKS) 3D7 strain for GS (*Pf*GS^cKS) through selection-linked integration approach[37] wherein, GS was fused in-frame with FKBP and GFP through linkers, followed by a neomycin selectable marker separated by skip peptide (Fig. 5a). The integration was confirmed by PCR analyzes for the genomic DNA and RNA isolated from

Fig. 3 | Characterization of r*Pf*GS lacking the first and second peptide inserts. **a** Schematic representations showing deletions of first and second peptide inserts. **b** HPLC chromatograms of ΔI₁r*Pf*GS and ΔI₂r*Pf*GS enzyme assays. Specific activities (mean ± SD shown below represent four different protein preparations. Lack of enzyme activity in ΔI₂r*Pf*GS was also verified with MnCl₂ and for a prolonged incubation of 6 h. **c** Effect of MSO and PPT on ΔI₁r*Pf*GS activity. Individual data points are shown with the respective light shaded colors. **d** Feedback inhibition of ΔI₁r*Pf*GS in the presence of MgCl₂ and MnCl₂ at 5 mM concentrations of amino acids and AMP. For **c** and **d** percentage of activities (mean ± SD) with respect to control (without inhibitor/feedback inhibitor) are shown. $n = 3$ different protein preparations. **e** Comparison of *Plasmodia* and bacterial GS I dodecamer channels. *Mt*, *St*, and *Hp* structures were retrieved from PDB. **f** Comparison of r*Pf*GS and ΔI₁r*Pf*GS thermal stabilities. Percentage of inhibition of the activities (mean ± SD) with respect to unexposed controls are shown. $n = 3$ different protein preparations.

Recombinant proteins were exposed to the respective temperatures for one hour before performing assays at 37 °C. **g** Chromatograms showing the dissociation of oligomers in r*Pf*GS and ΔI₁r*Pf*GS. Protein preparations were exposed to 37 °C or 42 °C for 15 min and subjected immediately to size-exclusion chromatography. **h**, Western analysis of r*Pf*GS (~65 kDa) and ΔI₁r*Pf*GS (~63 kDa) in 12.7 and 15.9 ml elution volume fractions. **i** Estimation of r*Pf*GS molecular weights eluted at 12.7 and 15.9 ml based on the elution of standard proteins. For **g**–**i** $n = 2$ independent protein preparations. **j** Unique hydrogen bond interactions of *Pf*GS and ΔI₂r*Pf*GS are shown for subunit A. Four subunits are represented in green (subunit A), pink (subunit B), yellow (subunit C) and cyan (subunit D). Interactions without the subunit background are shown below. **k** Superimposition of MD simulation structures of two adjacent subunits from upper and lower hexamers of *Pf*GS (grey) and ΔI₂r*Pf*GS (red). (n.s - not significant, **$P < 0.01$, ***$P < 0.001$, unpaired t-test; two-sided). Source data are provided as a Source Data file.

*Pf*GS^cKS parasites (Fig. 5b, c). Western analysis carried out with GFP and GS antibodies confirmed the expression of 120 kDa fusion protein in *Pf*GS^cKS parasites with levels comparable to parental 3D7 strain (Fig. 5d). Since the expression of GS fused with FKBP-GFP in *Pf*GS^cKS parasites is driven by native promoter, it helped us to verify the GS localization results obtained with polyclonal antibodies. Live imaging showed GFP fluorescence all over the parasite reconfirming the cytosolic localization of GS (Fig. 5e). To check the effect of FKBP-GFP fusion on *Pf*GS activity, we purified r*Pf*GS-FKBP-GFP and performed enzyme assays. While r*Pf*GS-FKBP-GFP was capable of forming glutamine, its specific activity was almost 70% less in comparison to r*Pf*GS (Fig. 5f; Supplementary Fig. 4a, b). In agreement, *Pf*GS^cKS parasites displayed ~60% reduction of growth in RPMI-1640 medium containing physiological levels (0.5 mM) of glutamine (RPMI^Pgln) when compared with *Pf*3D7 parasites, on day 7 representing three asexual cycles. Similar results were also obtained with normal RPMI-1640 medium containing 2 mM glutamine (RPMI^Ngln) (Fig. 5g). Moreover, *Pf*3D7 cultures could be maintained continuously for several days in a glutamine-free RPMI-1640 medium (RPMI^-gln) and we examined it for over 90 days (Supplementary Fig. 4c). Flow cytometry analysis performed at 48 h intervals for five successive cycles showed only a 15–20% decrease in the parasite multiplication rate for each cycle (Supplementary Fig. 4d), suggesting that glutamine derived from endogenous GS activity and Hb degradation are adequate to support the parasite growth. Interestingly, unlike *Pf*3D7, *Pf*GS^cKS parasites failed to grow in RPMI^-gln and no viable parasites could be detected after 4 days of glutamine removal (Fig. 5g; Supplementary Fig. 4e). All these results suggest that intervention of endogenous GS activity affects the growth of *Pf* asexual stages, highlighting its significance in *Pf*.

To perform GS mislocalization, *Pf*GS^cKS strain was transfected with a plasmid that expressed plasma membrane-targeting Lyn peptide fused with FRB and mcherry. After selecting the transfected *Pf*GS^cKS parasites (*Pf*GS^cKS+Lyn) with blasticidin, GS was knocked sideways from cytosol to the plasma membrane by the addition of rapamycin (Fig. 5a). This was evident from the change in the localization of GFP signal (Fig. 5h; Supplementary Fig. 4f). Since the active sites of GS are formed by adjacent monomers, membrane anchoring driven by rapamycin-induced dimerization of GS-FKBP-GFP with Lyn-FRB-mCherry would disrupt the oligomerization of GS and abrogate GS activity. The rapamycin-induced mislocalization of GS from its site of action caused further reduction in *Pf*GS^cKS+Lyn parasite growth in RPMI^Pgln, leading to almost 90% decrease in comparison with *Pf*3D7 parasites (Fig. 5g). Further, rapamycin alone did not have any effect on *Pf*3D7 and *Pf*GS^cKS asexual stage growth (Supplementary Fig. 4g). Western analysis and enzyme assays carried out for the cytosol and membrane fraction of rapamycin-induced *Pf*GS^cKS+Lyn parasites confirmed the mislocalization of GS and the loss in GS activity due to mislocalization (Supplementary Fig. 4h, i). Since GS expression was also detectable in the sexual stages, we examined its significance in the sexual stages of *Pf*GS^cKS+Lyn maintained in RPMI^Pgln. Treatment of cultures with rapamycin on day three

post-induction of gametocytes led to almost 70% reduction in the formation of mature, stage V gametocytes in comparison with untreated control (Fig. 5i, j). Again, rapamycin alone had no effect on gametocyte formation (Supplementary Fig. 4j). All these findings demonstrate the requirement of endogenous GS for the development of *Pf* asexual stages and gametocytes, signifying that Hb-derived and extracellular glutamine are inadequate for the optimal growth of *Pf*. We generated another transgenic line (*Pf*GS^HA-DD) to perform conditional knockdown wherein, GS was fused with HA-tagged destabilization domain (HA-DD)[38]. Like *Pf*GS^cKS parasites, *Pf*GS^HA-DD parasites displayed decreased growth in RPMI^Pgln and could not survive in RPMI^-gln. However, *Pf*GS^HA-DD parasites did not support GS knockdown, probably due to the abundant GS expression, and its complex oligomeric nature limiting the exposure of DD to Shield-1 and proteasomal degradation (Supplementary Fig. 5a–e, Supplementary Discussion).

GS is dispensable for the entire life cycle of *Pb*

We then examined the essentiality of GS in *Pb*. In contrast to *Pf*, GS could be deleted in *Pb* through double crossover recombination (Fig. 6a) as verified by PCR with genomic DNA and total RNA isolated from *Pb*GSKO parasites (Fig. 6b, c), and by Southern analysis (Fig. 6d). This was also confirmed at the protein level by Western and immunofluorescence analyzes (Fig. 6e, f). Interestingly, the growth of GSKO parasites in Balb/c mice (mouse model of anemia in rodent parasite infections) was similar to that of wildtype (WT) parasites and there was no significant difference in the mortality of GSKO-infected mice (Fig. 6g, h). The mortality due to anemia started around day 12 and almost 80% of the mice did not survive beyond day 20. There was also no significant difference in RBC versus reticulocyte preference of *Pb*GSKO parasites (Fig. 6i). Since host glutamine metabolism has been implicated in cerebral malaria (CM)[39], we examined whether GS deletion in *Pb* has any impact on cerebral pathogenesis in CM-susceptible C57BL/6 mice. Again, no significant differences could be observed in the parasite growth or CM mortality (Fig. 6j, k). Almost 70% of WT- or GSKO-infected mice succumbed to CM within day 10 when the blood parasitemia was around 20% and the rest died of anemia. The infected mice showed typical symptoms of CM such as coma, ataxia, paralysis etc., and the loss of blood brain-barrier integrity could be observed in Evans blue extravasation assays (Fig. 6l). Plasma levels of glutamine were comparable between WT- and GSKO-infected mice suggesting that GS deletion did not affect the host extracellular glutamine (Fig. 6m). For each molecule of glutamine produced by GS, one molecule of ammonia and ATP are utilized. Considering the neurotoxicity of ammonia and the ability of ATP to act as a danger signal in vertebrate host[40, 41], we examined the plasma levels of ammonia and ATP in GSKO-infected mice and the levels were comparable with WT-infected mice (Fig. 6n, o). These results suggest that GS is dispensable for the asexual stage development of *Pb*, and GS deletion does not alter the outcome of anemia or CM pathogenesis in mice.
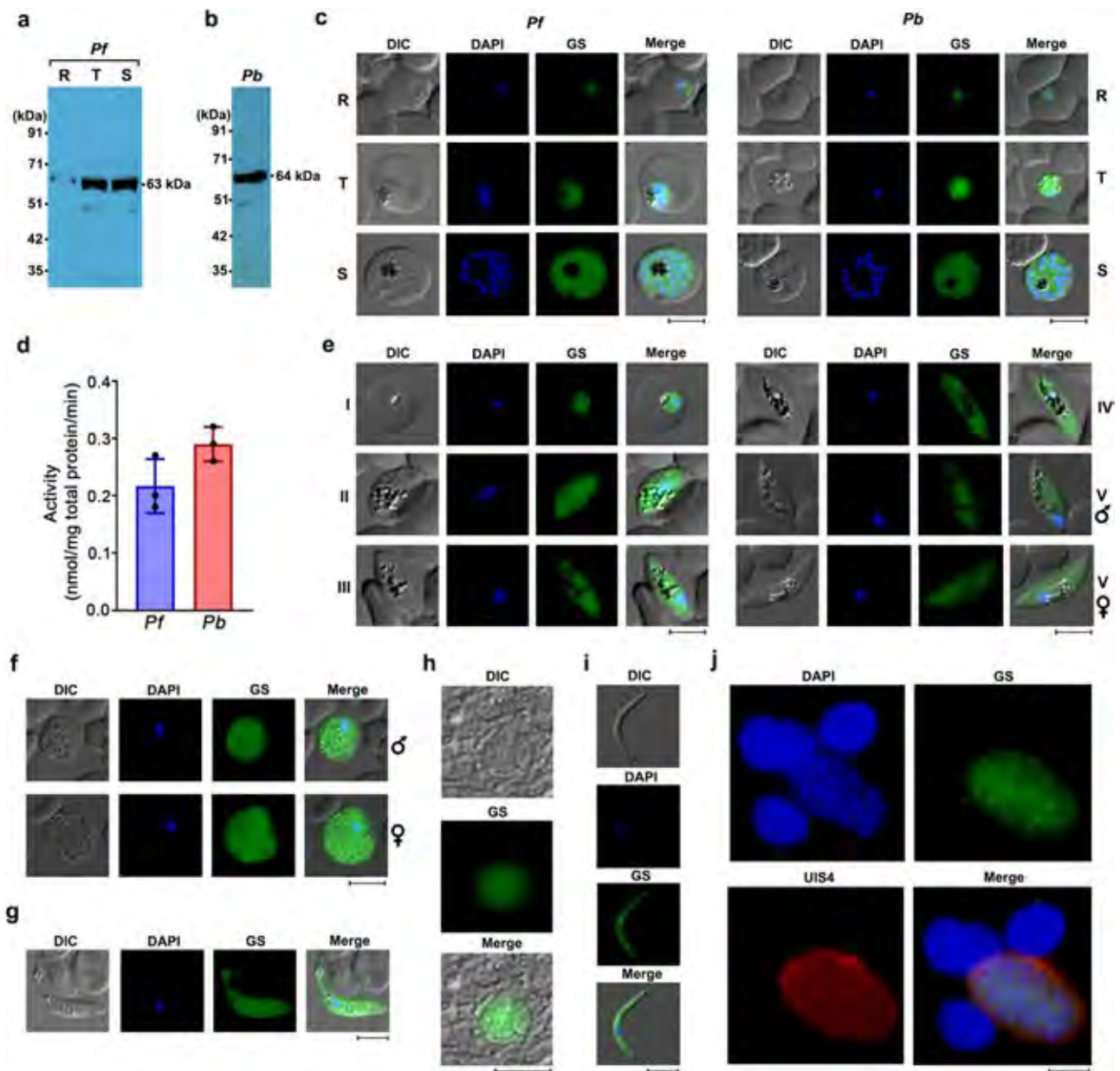
Fig. 4 | Expression of GS in the life cycle of *Plasmodia*. a Western analysis of GS expression in the lysates of *Pf* rings, trophozoites and schizonts. Equal number of rings (R), trophozoites (T) and schizonts (S) were used from 10 ml of tightly synchronized cultures. **b** Western analysis of GS expression in *Pb* parasite lysate. 50 μg of total protein was used. **c** Immunofluorescence analysis of GS expression in *Pf* and *Pb* rings (R), trophozoites (T) and schizonts (S). Scale bar = 5 μM. For **a–c**, *n* = 3 independent experiments. **d** GS activity in the parasite lysates of *Pf* and *Pb*. The activity (mean ± SD) was determined with respect to the total protein. *n* = 3 independent preparations. **e** Immunofluorescence analysis of GS expression in *Pf* gametocytes (Stage I-V). Scale bar = 5 μM. **f** Immunofluorescence analysis of GS expression in *Pb* gametocytes. Scale bar = 5 μM. **g–i** Immunofluorescence analysis of GS expression in *Pb* ookinete, oocyst and sporozoite, respectively. Scale bar for ookinete and sporozoite = 5 μM. Scale bar for oocyst = 20 μM. **j**, Immunofluorescence analysis of GS expression in *Pb* exo-erythrocytic stage. UIS4 antibody was used to identify the exo-erythrocytic stage. Scale bar = 20 μM. All the images were captured using 60x/100x objective. Oocyst image was captured using 20x objective. For **e–j** *n* = 2 independent experiments. Source data are provided as a Source Data file.

Our next interest was to understand its essentiality in the sexual and liver stage development of *Pb*. The number of male and female gametocytes, exflagellation centers observed for male gametocytes and ookinetes formed in vitro were comparable between WT and GSKO parasites (Fig. 7a–c). To assess the contribution of extracellular glutamine, we examined the male gametocyte exflagellation and ookinete formation of GSKO parasites in vitro in medium lacking glutamine. Interestingly, GSKO parasites could undergo exflagellation and give rise to ookinetes in the absence of extracellular glutamine (Fig. 7b, c) suggesting that glutamine reservoir generated in the gametocytes through Hb digestion and/or

extracellular uptake was adequate to support until ookinete formation that spans for a duration of 21 h. These findings could not be extended for oocyst and sporozoite development due to the lack of robust in vitro culture techniques. In vivo assessment of the sexual stage development in mosquitoes showed no significant differences in the number of ookinetes (Fig. 7d, e) and oocysts present in the gut (Fig. 7f, g). However, there was a significant 40% reduction in the sporozoites of salivary glands from GSKO-infected mosquitoes in comparison with WT-infected mosquitoes (Fig. 7h, i). These findings suggest that glutamine derived from mosquito hosts could support a major portion of *Pb*GSKO sexual stage development albeit a
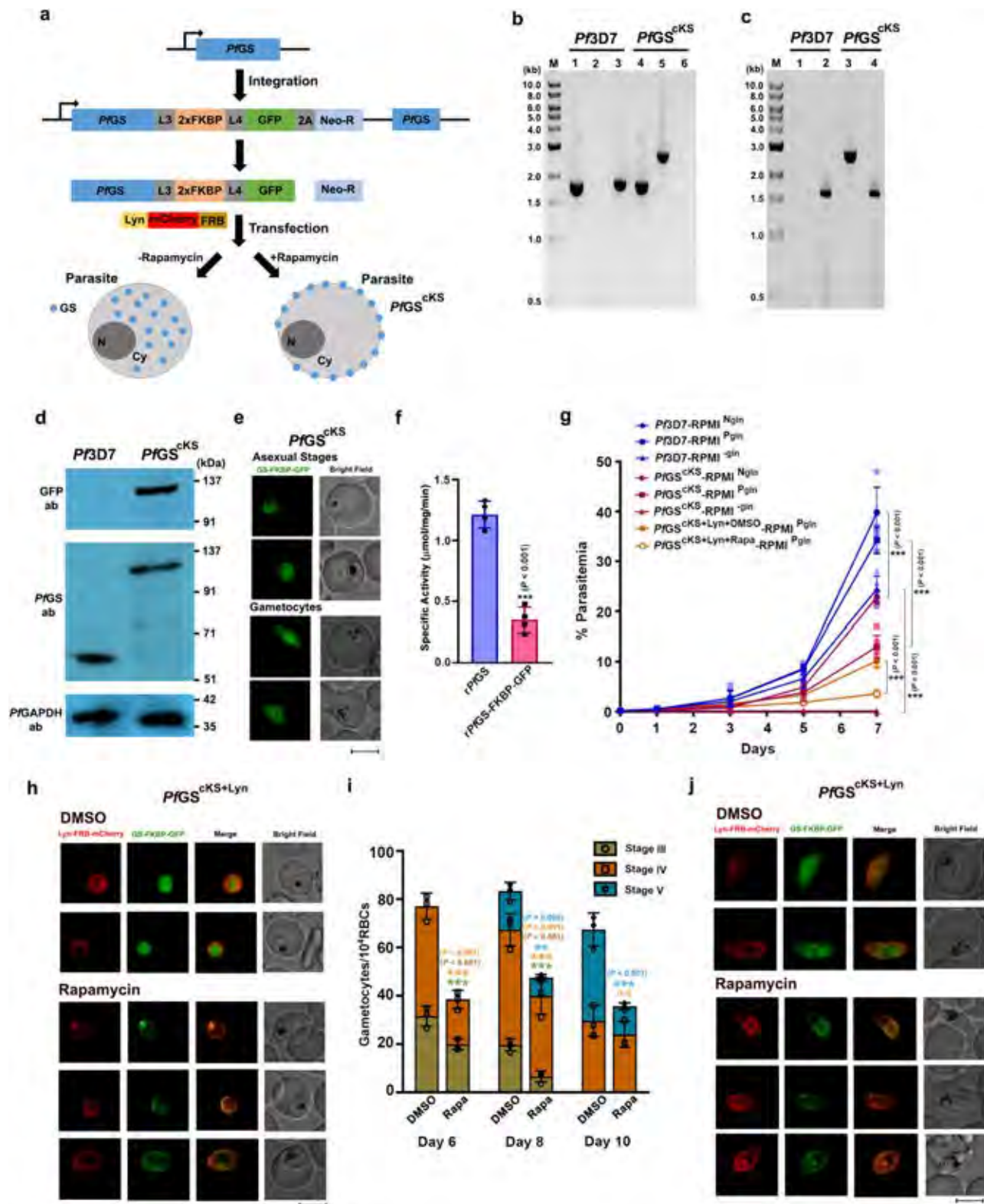
significant decrease in sporozoites was observed towards the end. Further, we examined the ability of GSKO sporozoites to undergo exo-erythrocytic stage development in the liver. Intravenous injection of 2×10^4 sporozoites into naïve mice showed that GSKO sporozoites could complete exo-erythrocytic stage development as evidenced from the appearance of blood-stage infections. The pre-patent period was comparable between WT and GSKO-infected mice and blood stage parasites were detectable on day 5. There was

no significant difference in the growth of sporozoite-derived GSKO asexual stages (Fig. 7j). These results were also confirmed by direct blood-feeding experiments. The absence of GS was verified by performing immunofluorescence for GSKO ookinetes and sporozoites isolated from the mosquitoes (Fig. 7k, l), and exo-erythrocytic stages grown in vitro using HC-04 cell line, using *Pb*GS antibodies (Fig. 7m). All these results suggest the dispensable nature of GS in the entire life cycle of *Pb*.

Fig. 5 | Conditional knock sideways of GS in *Pf*. a Schematic representation of conditional knock sideways approach to mislocalize *Pf*GS. **b** Genomic DNA PCR confirmation for *Pf*GS^cKS parasites. Lane 1 and 4: 1.76 kb product amplified with GS-specific forward and reverse primers. Lane 2 and 5: 2.64 kb product amplified with GS-specific forward and GFP-specific reverse primers to confirm the in-frame fusion. Lane 3 and 6: 1.82 kb product amplified with GS-specific forward and 3' UTR-specific reverse primer to confirm the integration. Lane M: 1 kb ladder. **c** RT-PCR confirmation for *Pf*GS^cKS parasites. Lane 1 and 3: 2.51 kb product amplified with GS-specific forward and GFP-specific reverse primers. Lane 2 and 4: 1.63 kb product amplified with GS-specific forward and reverse primers. Lane M: 1 kb ladder. **d** Western blot confirmation for GS-FKBP-GFP fusion in *Pf*GS^cKS parasites. Upper panel: Confirmation of 120 kDa fusion protein in *Pf*GS^cKS parasites with GFP antibody. Middle panel: Confirmation with *Pf*GS antibody. Lower panel: Parasite GAPDH as a loading control. **e** Live imaging of GS-FKBP-GFP localization in *Pf*GS^cKS parasites. Images were captured using 100x objective. Scale bar = 5 µM. For

b–e *n* = 3 independent experiments. **f** Specific activity of r*Pf*GS-FKBP-GFP fusion protein in comparison with r*Pf*GS. (mean ± SD; **P < 0.001, unpaired t-test; two-sided). *n* = 4 independent assays performed with two different protein preparations. **g** Asexual stage growth analysis of *Pf*3D7 and *Pf*GS^cKS parasites in RMPI^Ngln, RPMI^Pgln and RPMI^-gln medium, and *Pf*GS^cKS+Lyn parasites in RPMI^Pgln medium. (mean ± SD; ***P ≤ 0.001, Two-way ANOVA). Rapa - rapamycin. *n* = 4 independent experiments. **h** Live fluorescence analysis of GS mislocalization in rapamycin-treated *Pf*GS^cKS+Lyn asexual stages. Images were captured using 100x objective. Scale bar = 5 µM. **i** Analysis of gametocyte maturation in cKS-induced *Pf*GS^cKS+Lyn parasites in RPMI^Pgln medium. (mean ± SD; n.s - not significant, **P < 0.01, ***P < 0.001, Two-way ANOVA) Rapa - rapamycin. *n* = 3 independent experiments. **j** Live fluorescence analysis of GS mislocalization in rapamycin-treated *Pf*GS^cKS+Lyn gametocytes, respectively. Images were captured using 100x objective. Scale bar = 5 µM. *n* = 3 independent experiments. Source data are provided as a Source Data file.

MSO and PPT inhibit the growth of *Pf*, but not of *Pb*

The results of transgenic *Pf* and *Pb* parasites were further validated by examining the effect of MSO and PPT on in vitro growth of *Pf*, and in vitro and in vivo growth of *Pb*. It is known that the presence of glutamine in culture medium can compete with the cellular uptake of MSO and PPT because of its structural similarity[42–44]. Therefore, we preferred to examine the effect of MSO and PPT on in vitro growth of *Pf* in the presence and absence of glutamine. MSO and PPT addition could inhibit the growth of *Pf* asexual stages in the presence and absence of glutamine. The IC_{50} values for MSO and PPT inhibiting *Pf* growth in RPMI^-gln medium were in the range of ~25 µM and Giemsa-stained smears showed the presence of stressed, arrested, pyknotic and dead parasites (Fig. 8a–d). In RPMI^Pgln, the IC_{50} values obtained for MSO and PPT were almost 10 times higher (Supplementary Fig. 5f, g). On the contrary, MSO and PPT did not inhibit the growth of *Pb* in single-cycle in vitro cultures. Even at a 2 mM concentration of MSO, there was only a slight inhibition of around 20% in RPMI^-gln (Fig. 8e), and there was no inhibition in the presence of glutamine (Supplementary Fig. 5h). Similar effect was observed in vivo when *Pb*WT-infected mice were treated with a dosage of MSO and PPT, as high as 20 mg/kg (a non-lethal, sub convulsive dose) per day for four days starting from day 4 post-infection. The growth of *Pb*WT in the treated mice was similar to that of untreated control with no significant changes in the mortality of mice (Fig. 8f). Besides confirming the requirement of GS in *Pf*, the data obtained with the chemical inhibition studies indicate the effect of targeting GS for *Pf* infections.

Targeting GS affects the protein synthesis in *Pf*

To gain insights on *Pf*-specific requirement of GS, we examined the metabolic labeling of proteins using [35S]-Methionine and -Cysteine in in vitro cultures of *Pf* and *Pb*. Interestingly, MSO and PPT treatments for only 12 h could inhibit protein synthesis in *Pf*, but not in *Pb*. While a significant 40–50% inhibition in protein synthesis of *Pf* was observed at 50 µM MSO and PPT, the inhibition was close to 80% at 250 µM in RPMI^-gln medium (Fig. 9a, b). In RPMI^Pgln medium, MSO and PPT could lead to ~50% inhibition in protein synthesis at 1 mM concentration (Supplementary Fig. 5i, j). In case of *Pb*, no such inhibition was observed even in RPMI^-gln medium at 2 mM MSO and PPT (Fig. 9c, d). For further analysis, we performed our studies with MSO in RPMI^-gln medium. Examination of free glutamine levels in *Pf* parasites treated with MSO in RPMI^-gln medium with respect to the untreated parasites, and *Pb*GSKO parasites isolated from mice with respect to *Pb*WT parasites showed a similar decrease in the glutamine levels (Fig. 9e, f). However, the free asparagine levels were reduced to the extent of 1.5–2.0 fold in *Pf* parasites treated with MSO with respect to the untreated control (Fig. 9e), and almost remained unaltered in *Pb*GSKO parasites in comparison with *Pb*WT parasites (Fig. 9f). Since *Pf* proteins are rich in asparagine[45,46], we examined whether GS inhibition by MSO in *Pf* can lead to eIF2α phosphorylation - a molecular signature of amino acid

deprivation leading to the inhibition of protein synthesis. Interestingly, a short-term exposure of in vitro cultures to 250 µM MSO for 6 h could lead to prominent phosphorylation of eIF2α in *Pf* (Fig. 9g), and no such phosphorylation could be detected either in *Pb* WT or GSKO parasites (Fig. 9h). To investigate the reflection of eIF2α phosphorylation on *Pf* proteome, we performed proteomics analysis for MSO-treated *Pf*3D7 parasites. Around 150 *Pf* proteins associated with various metabolic and cellular functions, cytoadherence and host invasion, Hb degradation, etc., were significantly reduced or undetectable in MSO-treated *Pf*3D7 parasites from two independent experiments. This, in turn, represented >40% of the total proteins identified in the control, suggesting an overall decrease in protein synthesis (Supplementary Fig. 6a; Fig. 9i, j; Supplementary Data 2). This also included important asparagine-rich proteins such as tRNA ligases, components of RNA processing and protein degradation pathways, lipocalin associated with hemozoin formation and antimalarial drug sensitivity[47], heat shock protein 110c essential for stabilizing the asparagine repeat-rich parasite proteins[46] etc. (Fig. 9j; Supplementary Data 2). Only ten proteins were found to be significantly upregulated in MSO-treated *Pf*3D7 parasites (Supplementary Fig. 6b; Supplementary Data 2).

Given the primitive role of TCA cycle and mitochondrion in the asexual stages of *Plasmodium*, the other major functions of glutamine that could be considered for growth inhibition are nucleotide and hexosamine biosynthesis. To examine the effect of MSO treatment on nucleotide biosynthesis, we performed 32P-orthophosphoric acid and [35S]-Methionine and -Cysteine radiolabelling of in vitro *Pf* cultures, and assessed RNA and protein synthesis in parallel for synchronized rings and trophozoites. While both the stages showed inhibition in protein and RNA synthesis, inhibition in protein synthesis was comparatively higher (Supplementary Fig. 7a, b). The levels of nucleotides were comparable between untreated and MSO-treated *Pf* parasites (Supplementary Fig. 7c). In addition, we supplemented *Pf* cultures with orotic acid (OA) and glucosamine (GlcN) - the respective committed precursors of pyrimidine nucleotide and hexosamine biosynthesis. OA supplementation up to 30 µM and GlcN supplementation up to 2 mM concentrations are well tolerated in *Pf* cultures without much inhibition of parasite growth[48,49]. However, the supplementation of *Pf* cultures with OA or GlcN independently, and the combination of both could not rescue MSO inhibition by more than 20% even in 24 h and 48 h (Supplementary Fig. 8a, b). The supplementation of OA and GlcN at concentrations above 30 µM and 2 mM, respectively, did not rescue further and there was actually a mild growth inhibition. Since MSO can also inhibit γ-glutamylcysteine synthetase to certain extent[26], enzyme catalyzing the first step in glutathione synthesis, we examined the levels of glutathione in MSO-treated *Pf* parasites. However, no significant differences could be observed between treated and untreated *Pf* parasites (Supplementary Fig. 8c), and similar results were obtained for *Pb*WT and *Pb*GSKO parasites (Supplementary Fig. 8d), suggesting that the inhibition or deletion of GS does not affect the levels of
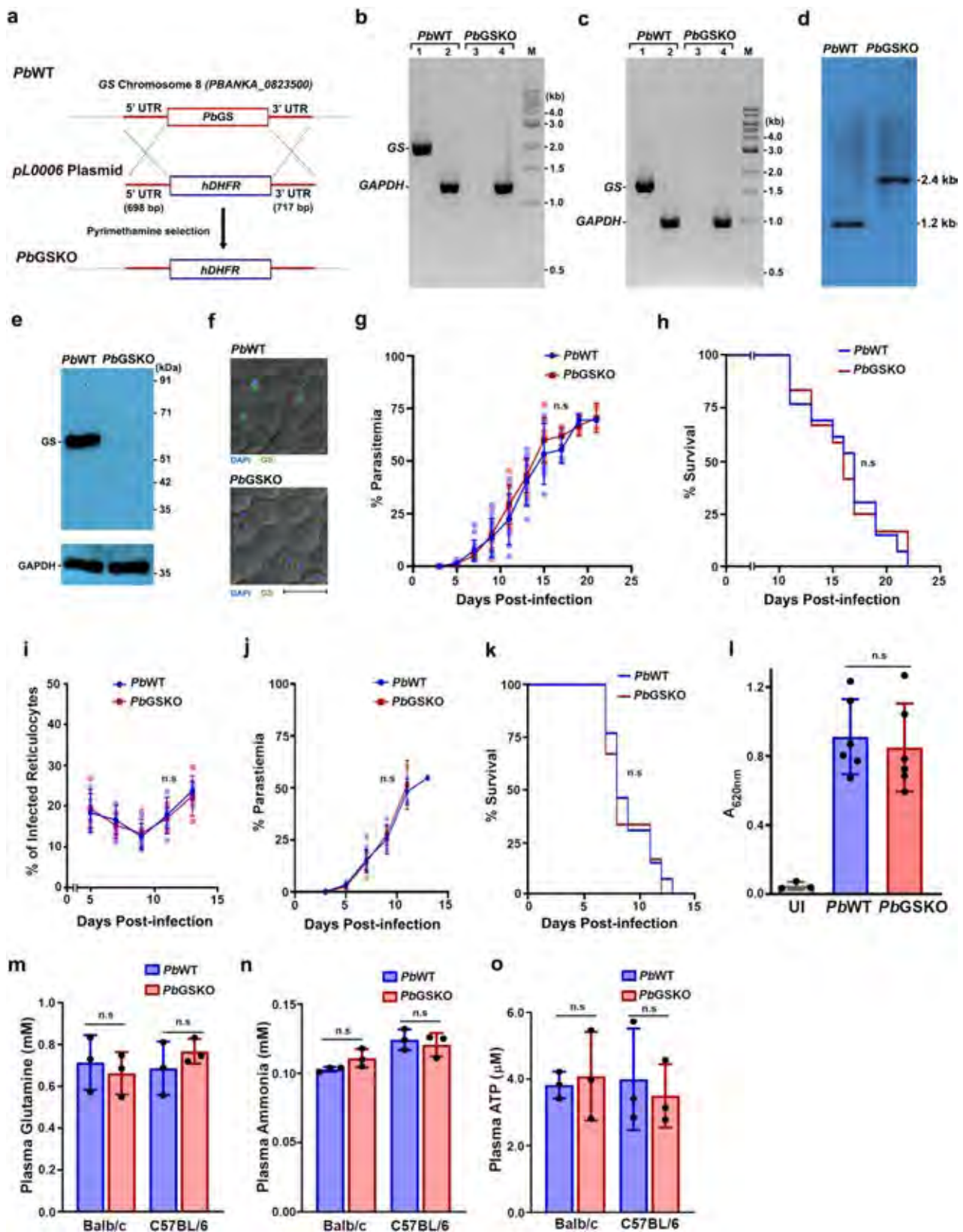
glutathione in *Pf* or *Pb* parasites, respectively. More importantly, the experiments of chemical inhibition and cKS were all carried out in RPMI^{gln} or RPMI^{Pgln} medium containing ~5 times higher asparagine levels (378 μM) than plasma (40–80 μM), suggesting that the extracellular asparagine could not compensate for the endogenous asparagine deficit in *Pf* caused by GS inhibition. Even at a very high

extracellular concentration of 5 mM, asparagine could not restore the growth inhibition of MSO in *Pf* (Supplementary Fig. 8e) and rescue GS-mislocalized *Pf*GS^{cKS} parasite growth (Supplementary Fig. 8f). This in turn correlates with the absence of detectable transporters for aspartate and asparagine in apicomplexan parasites[4]. All these findings suggest that *Pf*-specific requirement of GS could be due to a unique

Fig. 6 | Characterization of *Pb*GSKO in the asexual stages. a Double crossover recombination strategy utilized for the generation of *Pb*GSKO parasites. **b** Genomic DNA PCR confirmation for GS deletion in *Pb*. Lane 1 and 3: GS amplification (2.04 kb). Lane 2 and 4: *Pb*GAPDH amplification (1.25 kb). Lane M: 1 kb ladder. **c** RT-PCR confirmation for GS deletion. Lane 1 and 3: GS amplification (1.66 kb). Lane 2 and 4: GAPDH amplification (1.01 kb). Lane M: 1 kb ladder. **d** Southern blot analysis to confirm GS deletion. **e** Western blot confirmation of GS deletion. 50 μg total protein was loaded. GAPDH was used as control. **f** Immunofluorescence confirmation for GS deletion. Scale bar = 10 μM. For **b**–**f** n = at least 2 independent experiments. **g** Growth analysis of *Pb*WT (n = 13) and *Pb*GSKO (n = 13) in Balb/c mice. 10^5 parasites were used to initiate infections. (mean ± SD; n.s - not significant, Two-way ANOVA). **h** Mortality curves of mice infected with *Pb*WT (n = 13) and *Pb*GSKO (n = 12) parasites in Balb/c mice. (n.s - not significant, log-rank (Mantel-

Cox) test). **i** Percentage of infected reticulocytes in parasitized red cells of *Pb*WT (n = 5) and *Pb*GSKO-infected mice (n = 5). (mean ± SD; n.s - not significant, Two-way ANOVA). **j** Growth analysis of *Pb*WT (n = 13) and *Pb*GSKO (n = 12) in C57BL/6 mice. 10^5 parasites were used to initiate infections. (mean ± SD; n.s - not significant, Two-way ANOVA). **k** Mortality curves of mice infected with *Pb*WT (n = 13) and *Pb*GSKO (n = 12) parasites in C57BL/6 mice. (n.s - not significant, log-rank (Mantel-Cox) test). **l** Quantification of Evans blue extravasation in the brain samples of mice infected with *Pb*WT and *Pb*GSKO parasites (n = 3). (mean ± SD; n.s - not significant, unpaired t-test; two-sided). UI - uninfected mouse. **m**–**o** Estimation of plasma glutamine (**m**), ammonia (**n**) and ATP (**o**) in *Pb*WT- and *Pb*GSKO-infected Balb/c and C57BL/6 mice (n = 3). (mean ± SD; n.s - not significant, unpaired t-test; two-sided). Source data are provided as a Source Data file.

functional requirement of glutamine for the synthesis of asparagine that is crucial for asparagine-rich proteins in *Pf*, but not in *Pb*.

Effect of GS inhibitors on *P. vivax* (*Pv*) and ART-resistant *Pf*Cam3.I^R539T parasites

We next sought to examine the requirement of GS in *Pf* clinical samples and investigate whether the non-essentiality of GS in *Pb* could be corroborated with *Pv* - another human parasite whose proteins are not asparagine-rich. For this, we collected the blood samples from *Pf*- and *Pv*-infected patients and incubated them in in vitro cultures without or with glutamine and assessed their growth in the presence of MSO and PPT. MSO and PPT could inhibit the growth of *Pf* clinical samples to the extent that was observed for *Pf*3D7 strain. However, as observed for *Pb*, MSO, and PPT caused only a ~ 10% inhibition in the growth of *Pv* clinical samples (Fig. 10a, b; Supplementary Fig. 9a, b). This in turn suggested that GS requirement is restricted to *Pf* mainly due to the asparagine-rich nature of its proteins containing asparagine repeats. It has been shown that GS levels are upregulated in ART-resistant *Pf* parasites during ART exposure favoring them to synthesize glutamine for nitrogen storage and prepare for starvation[50]. Therefore, our next interest was to examine whether inhibiting GS by MSO can be effective in ART-resistant strain. For this, we performed ring-stage survival assay (RSA) using tightly synchronized rings of ART-resistant *Pf*Cam3.I^R539T strain. ART or dihydroartemisinin (DHA; 700 nM) exposure for 6 h led to viable parasites in *Pf*Cam3.I^R539T cultures after 72 h, but not in ART-sensitive *Pf*3D7 cultures. Interestingly, the exposure of ART or DHA in combination with MSO for 6 h led to ~50–80% reduction in viable parasites at 50–250 μM concentrations of MSO in RPMI^gln in vitro cultures with respect to the treatment with ART or DHA alone. The exposure of *Pf*Cam3.I^R539T rings to MSO alone for 6 h could only lead to 10–20% inhibition with respect to the untreated control (Fig. 10c). A similar inhibition pattern was observed for RPMI^Pgln in vitro cultures wherein, 50% inhibition was observed at ~500 μM MSO (Supplementary Fig. 9c). PPT could also reduce the viability of *Pf*Cam3.I^R539T rings in combination with ART or DHA, although PPT was slightly less effective than MSO (Fig. 10d; Supplementary Fig. 9d). These data suggest the effect of inhibiting GS in ART-resistant *Pf* strain.
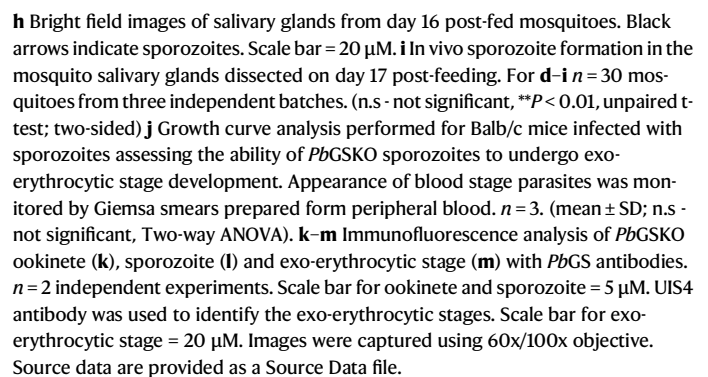
Discussion

GS is an ancient ubiquitous enzyme known for extensive evolutionary adaptations and diverse regulatory mechanisms[51, 52]. It plays a pivotal role in the nitrogen metabolism of prokaryotes and eukaryotes. Glutamine, the product of GS, regulates protein turnover and homeostasis, apoptosis, autophagy, pH homeostatis, cell signaling etc. It is required for nucleotide and hexosamine biosynthesis. Glutamine is also a gluconeogenic and lipogenic precursor, and it serves as an anaplerotic carbon source for TCA cycle controlling cell growth, proliferation and function[15]. A plethora of functions played by glutamine renders it a versatile and the most abundant amino acid, not only in humans but also in mosquitoes. While the coevolution of malaria parasite with human and mosquito hosts, and the parasitic niche that is

conducive for acquiring amino acids from the host, have resulted in the loss of de novo pathways for amino acid biosynthesis, the parasite has surprisingly retained a gene for GS. We demonstrate that *Plasmodium* GS is enzymatically active and it has evolved as a unique type I GS that cannot be classified under α or β subtypes. It is neither regulated by adenylylation nor feedback inhibited by the end products of glutamine metabolism that controls GS1β activity (Fig. 10e). In agreement with this, the three key proteins essential for GS adenylylation and deadenylylation cycle - adenylyltransferase (ATase;*glnE*), bifunctional uridylyltransferase/uridylyl-removing enzyme (UTase/UR;*glnD*) and the signal transduction protein pII[36] are also absent in the malaria parasite[17]. Further, parasite GS is not feedback inhibited by glutamine that strongly inhibits GS Iα activity. AMP is the only metabolite that showed moderate inhibition.

We propose that parasite GS has evolved to adapt to the asexual stage metabolism (Fig. 10e). The asexual stages acquire up to 75% of host Hb and degrade it in the FV, releasing amino acids in millimolar concentrations that are far more than the requirement for protein synthesis. The parasite utilizes approximately one-fifth of Hb-derived amino acids and effluxes the surplus. This includes amino acids such as glycine, serine, and alanine that inhibit GS of other organisms[53–56]. Therefore, the absence of feedback inhibition by amino acids could have rendered parasite GS withstanding its activity in the cytosol where there is a continuous release of amino acids from FV. Likewise, the lack of regulation by adenylylation could be a metabolic adaptation. α-ketoglutarate, a TCA cycle intermediate, is a key allosteric regulator of GS and low intracellular concentrations of α-ketoglutarate inactivate GS by bringing out adenylylation through pII/ATase[36]. It is known that the asexual stages support their rapid growth and proliferation by continuously deriving ATP through glycolysis and the flux of carbon skeletons from glucose into the TCA cycle is minimal[14]. Most of the TCA cycle enzymes could be deleted without any significant effect on asexual stages. However, TCA cycle is essential for mosquito stage development[57]. The lack of regulation by adenylylation could have provided the flexibility for parasite GS to function in all the life cycle stages irrespective of its energy metabolism being supported by glycolysis or oxidative phosphorylation. It is worthwhile to mention that *Hp* lacking adenylylation of GS is also known for mixed acid fermentation pathways involving alternate electron acceptors and reduced TCA cycle activity[58]. The preference of parasite GS for Mg^{2+} over Mn^{2+} could also be correlated with the abundant Mg^{2+} levels (39–59 μg/g) in RBCs than Mn^{2+} (0.009–0.033 μg/g), and the presence of multiple putative magnesium transporters in the parasite genome[17].

Another interesting feature of *Plasmodia* GS is the presence of two characteristic peptide inserts. We show that the first peptide insert occupying dodecamer channel contributes to the stability of *Pf*GS at febrile temperatures. *Plasmodium* parasites show extensive adaptations to febrile temperatures, with *Pf* heat shock protein 110 stabilizing the asparagine repeat-rich parasite proteins and *Pf*AP2-HS transcription factor protecting the parasites[46,59]. Unlike the first peptide insert, deletion of second insert present near the active site renders parasite

Fig. 7 | Sexual and exo-erythrocytic stage development of *Pb*GSKO parasites.
a Number of male and female gametocytes observed in Giemsa-stained smears of Balb/c mice ($n = 6$) prepared on day 8 post-infection. **b** Number of exflagellation centers observed in glutamine-free (Gln⁻) and glutamine-containing (Gln⁺) exflagellation medium for the blood collected on day 8 post-infection. $n = 7$ different Balb/c mice. **c** In vitro ookinete formation in glutamine-free (Gln⁻) and glutamine-containing (Gln⁺) medium. $n = 3$ different Balb/c mice. For **a**–**c** (mean ± SD; n.s - not significant, unpaired t-test; two-sided). **d** Giemsa-stained images for in vivo ookinetes observed in smears prepared from the blood bolus collected at 21 h post-fed mosquito guts. Images were captured using 100x objective. Scale bar = 5 μM. **e** In vivo ookinete formation in the mosquito guts dissected at 21 h post-feeding. **f** Mercurochrome staining for the day 10 post-fed mosquito guts. Black arrows indicate oocysts. Images were captured using 20x objective. Scale bar = 20 μM. **g** In vivo oocyst formation in the mosquito guts dissected on day 10 post-feeding.

h Bright field images of salivary glands from day 16 post-fed mosquitoes. Black arrows indicate sporozoites. Scale bar = 20 μM. **i** In vivo sporozoite formation in the mosquito salivary glands dissected on day 17 post-feeding. For **d**–**i** $n = 30$ mosquitoes from three independent batches. (n.s - not significant, **$P < 0.01$, unpaired t-test; two-sided) **j** Growth curve analysis performed for Balb/c mice infected with sporozoites assessing the ability of *Pb*GSKO sporozoites to undergo exo-erythrocytic stage development. Appearance of blood stage parasites was monitored by Giemsa smears prepared form peripheral blood. $n = 3$. (mean ± SD; n.s - not significant, Two-way ANOVA). **k**–**m** Immunofluorescence analysis of *Pb*GSKO ookinete (**k**), sporozoite (**l**) and exo-erythrocytic stage (**m**) with *Pb*GS antibodies. $n = 2$ independent experiments. Scale bar for ookinete and sporozoite = 5 μM. UIS4 antibody was used to identify the exo-erythrocytic stages. Scale bar for exo-erythrocytic stage = 20 μM. Images were captured using 60x/100x objective. Source data are provided as a Source Data file.

GS completely inactive. It would be of interest to examine the compensatory structural rearrangements that have occurred in *Plasmodium* GS to accommodate this insert and their impact on GS activity. It is also possible that this insert is responsible for the lack of feedback inhibition by amino acids. Further structural studies are required to understand its conformational flexibility in the presence of substrates, transition-state analogs, and feedback inhibitors. Altogether, our findings highlight the distinct evolution of parasite GS and shed insights on unique biochemical and structural features of parasite GS that complement the metabolic signature and febrile niche of asexual stage parasites.

Another important finding of this study is the recognition of species-specific differences in the requirement of *Plasmodium* GS. By combining reverse genetics with chemical inhibition studies and by

Fig. 8 | Differential Inhibition of *Pf* and *Pb* parasites by MSO and PPT. a Effect of MSO on in vitro cultures of *Pf* in RPMI^{-gln} medium. $n = 4$ independent experiments. **b** Giemsa-stained images of *Pf* parasites treated with MSO. **c** Effect of PPT on in vitro cultures of *Pf* in RPMI^{-gln} medium. $n = 3$ independent experiments. **d** Giemsa-stained images of *Pf* parasites treated with PPT. **e** Effect of MSO and PPT on in vitro single-cycle cultures of *Pb* maintained in RPMI^{-gln} medium. Giemsa-stained images of MSO and PPT-treated *Pb* schizonts are provided for 1 mM concentration. A growth assessment was carried out based on ^{3}H-hypoxanthine uptake and verified by Giemsa-stained smears. $n = 3$ independent experiments. **f** Effect of MSO and PPT on in vivo *Pb* growth in Balb/c mice. *Pb* infections were initiated by injecting 10^{5} parasites intraperitoneally on day 0. Mice were treated with the respective doses of MSO and PPT for four consecutive days starting from day 4. $n = 3$ different mice. Giemsa-stained images of MSO and PPT-treated *Pb* parasites are provided for 20 mg/kg treatment. Images for Giemsa-stained parasites were captured using 100x objective. Scale bar = 5 μM. For **a**, **c**, **e**, and **f** the data represent mean ± SD. Source data are provided as a Source Data file.

correlating the results with clinical samples, we show that GS is required for optimal *Pf* growth, but non-essential for *Pb* and *Pv*. GS deletion in *Pb* does not affect the asexual stage parasite growth or the disease outcome in mice. *Pb*GSKO parasites can complete the

transmission cycle and the only significant effect is a ~40% reduction in sporozoite formation. The dispensable nature of *Pb*GS is also reported in high-throughput barcoded *Pb* mutant studies[60,61]. More importantly, GS deletion does not alter the intracellular levels of asparagine in *Pb*,
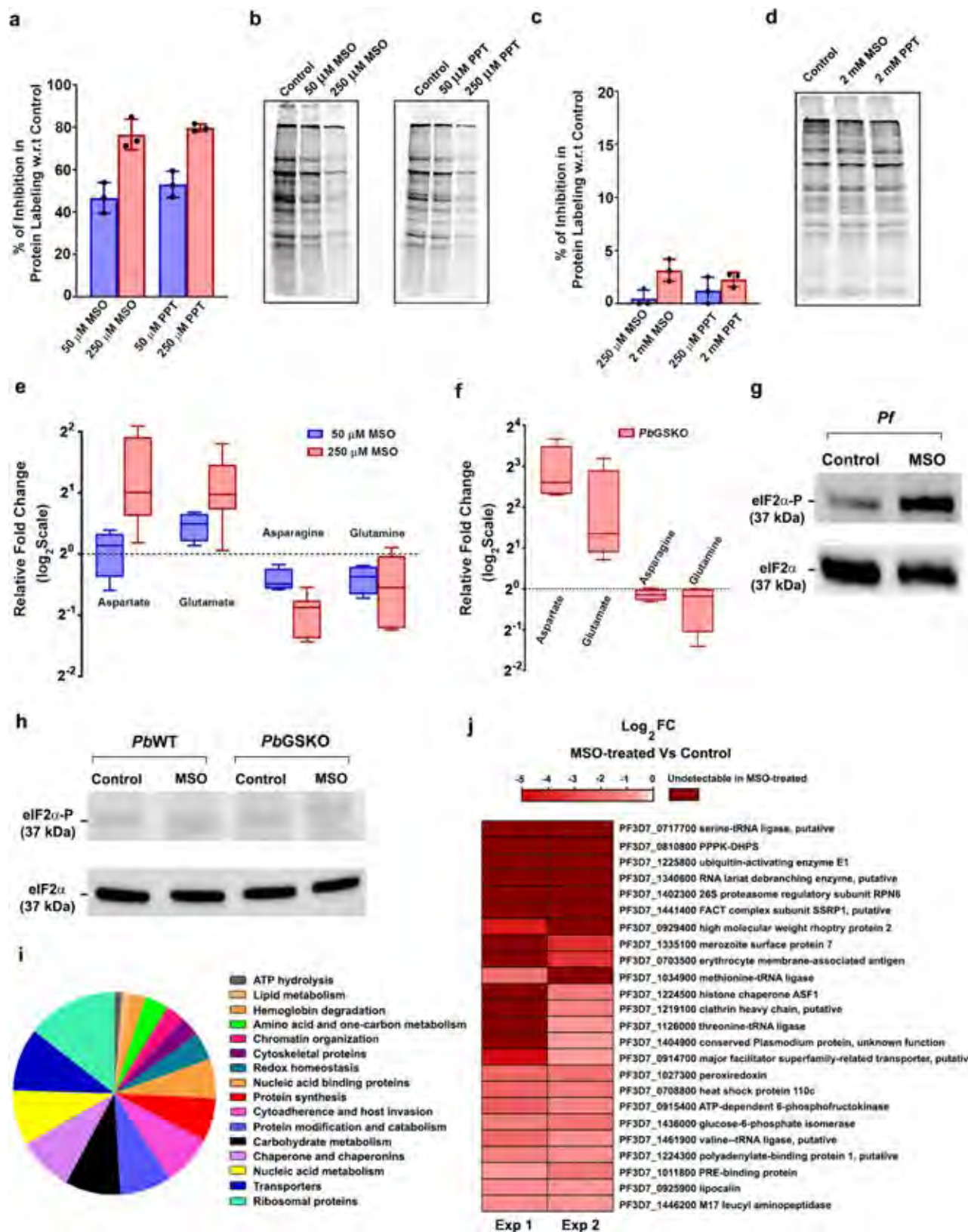
and treatment of *Pb*WT parasites with MSO or PPT does not affect protein synthesis. In contrast, chemical inhibition of *Pf* with MSO and PPT shows significant reduction in the asparagine levels and a clear-cut inhibition of protein synthesis within 12 h, suggesting the requirement of GS for asparagine and protein synthesis in *Pf*. Our in vitro studies with MSO and PPT are performed in the presence and absence of

glutamine, since glutamine is known to compete with their uptake. We have also substantiated the requirement of GS in *Pf* asexual and sexual stage development by cKS approach. For essential metabolic enzymes that are abundantly expressed, even 90–95% knockdown does not lead to significant growth defects, and 5–10% of enzyme activity from the leftover protein seems to be adequate for normal parasite growth[62]. In

Fig. 9 | Targeting GS in *Pf* affects asparagine levels and protein synthesis. a, **c** In vitro metabolic labeling of *Pf* (**a**) and *Pb* (**c**) cultures with [^{35}S]-Methionine and -Cysteine. Percentage of inhibition (mean ± SD) for treated parasites based on ^{35}S counts with respect to solvent control is shown. **b**, **d** SDS-PAGE analysis of protein labeling for *Pf* (**b**) and *Pb* (**d**) parasites. Phosphorimager scan was performed after overnight exposure. $n = 3$ independent experiments. **e** Quantification of aspartate, glutamate, asparagine and glutamine levels in *Pf* cultures treated with 50 ($n = 4$) and 250 μM ($n = 6$) MSO. In vitro experiments were carried out in RPMI^{-gln} medium. **f** Quantification of aspartate, glutamate, asparagine and glutamine levels in *Pb*GSKO parasites ($n = 4$). For **e** and **f** relative fold changes of the amino acids with respect to control are plotted after normalizing them with the levels of serine, threonine, histidine, arginine and tyrosine. Box and whisker plots display minimum/maximum points (whiskers), 25th/75th percentile (boxes) and median (center line). **g**, **h** Western analysis of total and phosphorylated eIF2α levels in *Pf* and *Pb*

parasites, respectively. 10 ml of synchronized *Pf* cultures having rings were treated in vitro with 250 μM MSO for 6 h in RPMI^{-gln} medium. Shorter treatment of *Pf* rings was preferred since eIF2α phosphorylation occurs at late asexual stages. $n = 4$ independent experiments. For *Pb*, infected mouse blood containing rings was incubated in vitro with 250 μM MSO for 6 h in RPMI^{-gln} medium. $n = 2$ independent experiments. **i** Functional classification of downregulated proteins in MSO-treated *Pf* parasites. **j** List of downregulated asparagine-rich proteins in MSO-treated *Pf* parasites. Proteins containing ≥10% asparagine or at least one asparagine repeat with 5 or more asparagine residues were considered asparagine-rich. For **i** and **j** proteins identified in both the untreated controls of two independent experiments and either undetectable or significantly downregulated (≥1.5 fold) in MSO-treated *Pf* parasites are represented. List of other downregulated proteins is provided in Supplementary Fig. 7a. Source data and silver-stained gels representing phosphorimager scans are provided as a Source Data file.

case of *Pf*GS^{cKS}, there was almost 90% growth inhibition suggesting the important role played by GS in *Pf*. This is in agreement with the low mutant fitness score (MFS) of *Pf*GS observed in piggyBac mutagenesis[17]. Despite being predicted as non-essential with high mutagenesis index score, low MFS suggests the relatively low abundance of GS mutants in the pool, indicating a high fitness cost of the GS mutation. We have extended our findings on *Pb* to *Pv* by demonstrating that in vitro treatment of MSO and PPT does not cause significant growth inhibition in *Pv* clinical samples. While the results obtained with *Pb* do not suggest significant differences in the RBC versus reticulocyte preference upon GS deletion, the contribution of reticulocyte tropism to the refractoriness of MSO and PPT inhibition in *Pv*, if any, needs further investigations.

Glutamine is limited in Hb[6] representing ~1.3% of the total amino acids present in α and β chains of Hb, in comparison to ~4–5% of glutamate or aspartate. Our findings clearly suggest that Hb-derived and extracellular glutamine are inadequate to support optimal *Pf* growth in asexual and sexual stages when the endogenous GS activity is compromised. With a very high AT content of 80.6% in its genome, *Pf* has a distinct evolutionary path derived from *Laverania* subgenus infecting African Great Apes. The rest of the human parasites - *vivax*, *malariae*, *ovale* and *knowlesi* represent *Plasmodium* (*non-Laverania*) subgenus and their AT content of genome varies between 60–75%. The 23 Mb AT-rich genome of *Pf* encodes more than 5000 proteins and the unique feature of *Pf* proteins is their asparagine-rich nature. Many *Pf* proteins expressed in different developmental stages have asparagine repeats with an average length of 37 residues that span across 30% of the proteome[46]. While AT-rich genome of *Pf* could be attributed to asparagine-rich nature, encoded mainly by AAT, such repeats are not present in other species like *malariae* and *ovale* with a reasonably high AT content. The evolutionary significance of asparagine-rich *Pf* proteome remains unclear. However, asparagine repeats present in the Low Complexity Region (LCR) are visualized to act like 'sponges' for asparaginyl-tRNA, rendering a rate-limiting function in *Pf* protein synthesis[46]. Despite having a high requirement of asparagine, *Pf* can be maintained in vitro in an amino acid-free RPMI supplemented only with isoleucine. Therefore, *Pf* should have a biosynthetic machinery to support its high asparagine requirement for protein synthesis. While our results show that *Pf*GS supplies glutamine as an amide donor for asparagine synthesis, they do not exclude the requirement of glutamine for other metabolic pathways as evident from the decreased RNA labeling in MSO-treated *Pf*. Requirement of glutamine for other metabolic pathways may eventually become prominent at prolonged duration of MSO treatment although inhibition of protein synthesis occurs early. Our results also suggest that *Pb* and *Pv* parasites can satisfy glutamine requirement for protein synthesis and other metabolic pathways in the absence of endogenous GS activity through hemoglobin degradation and/or extracellular sources. Deletion or inhibition of

endogenous GS does not have a significant impact on *Pb* or *Pv* growth. In summary, asparagine-rich proteome imposes a selective burden in *Pf* for glutamine besides its requirement for other metabolic pathways.

Finally, we show the effect of inhibiting GS in ART-resistant *Pf* strain. The exposure of ART-resistant *Pf*Cam3.I^{R539T} strain to the combination of ART/DHA with MSO/PPT for a short duration of 6 h leads to a substantial decrease in the parasite survival. Since ART-resistant parasites depend on glutamine as a nitrogen reservoir[50] and exhibit fitness loss in amino acid and nutrient limitation conditions[63,64], we propose that the asparagine-rich nature of *Pf* proteins and the requirement of glutamine as a nitrogen source for asparagine and protein synthesis can be explored for ART-resistance. GS is being examined as a target for *Mt* infections and structural analogues of MSO, PPT, and ATP have been evaluated for their potential to inhibit *Mt*GS[24,36]. Targeting GS is also being attempted for cancer therapy since glutamine metabolism plays an important role in cancer cells and GS levels are upregulated in certain types of cancer[65]. We believe that the unique structural features of *Plasmodium* GS and its unusual type I nature can serve as a platform for developing *Plasmodium*-specific GS inhibitors. The other challenges such as the efficient uptake of GS inhibitors and their efficacy at clinically relevant doses with favorable therapeutic index have to be addressed. Asparagine synthetase (AS) mutation also seems to impose a high fitness cost in *Pf* as evidenced by low MFS[17] and therefore, *Pf*AS can be explored as a target. We have already shown that AS can be deleted in *Pb*[8] and it would be of interest to examine its requirement in *Pf*. Like GS, AS is being explored for cancer therapy, and adenylated sulfoximines and methylsulfoximines are shown to be potential inhibitors of AS[66]. While an antimalarial for all the species of *Plasmodium* is preferable, the inclusion of a *Pf*-specific drug in the existing ACTs would be helpful to address ACT failure and fulfil the requirement of an additional partner in ACTs for *Pf* infections[67]. In such combinations, the primary drugs will clear the other species. Nevertheless, the reason for why other *Plasmodium* species lacking asparagine-rich proteins have retained GS and whether *Pf*GS can be targeted for the mosquito and liver stages require further studies. The metabolic transactions in *Pf* that facilitate the channeling of glutamine for protein synthesis need to be addressed.

Methods

Ethics statement

The studies involving mice were approved by Institutional Animal Ethics Committee (ILS/IAEC-69-AH/AUG-16) and the experiments were carried out according to the national guidelines framed by "The Committee for the Purpose of Control and Supervision of Experiments on Animals (CPCSEA)". *Pf* and *Pv* clinical samples were collected with the approvals from Institutional Ethics Committee (IEB)/ Institutional Review Board (IRB) of the Institute of Life Sciences (94/HEC/19), Bhubaneswar, and KMC Hospital (IEC:248/ 2019), Mangalore.
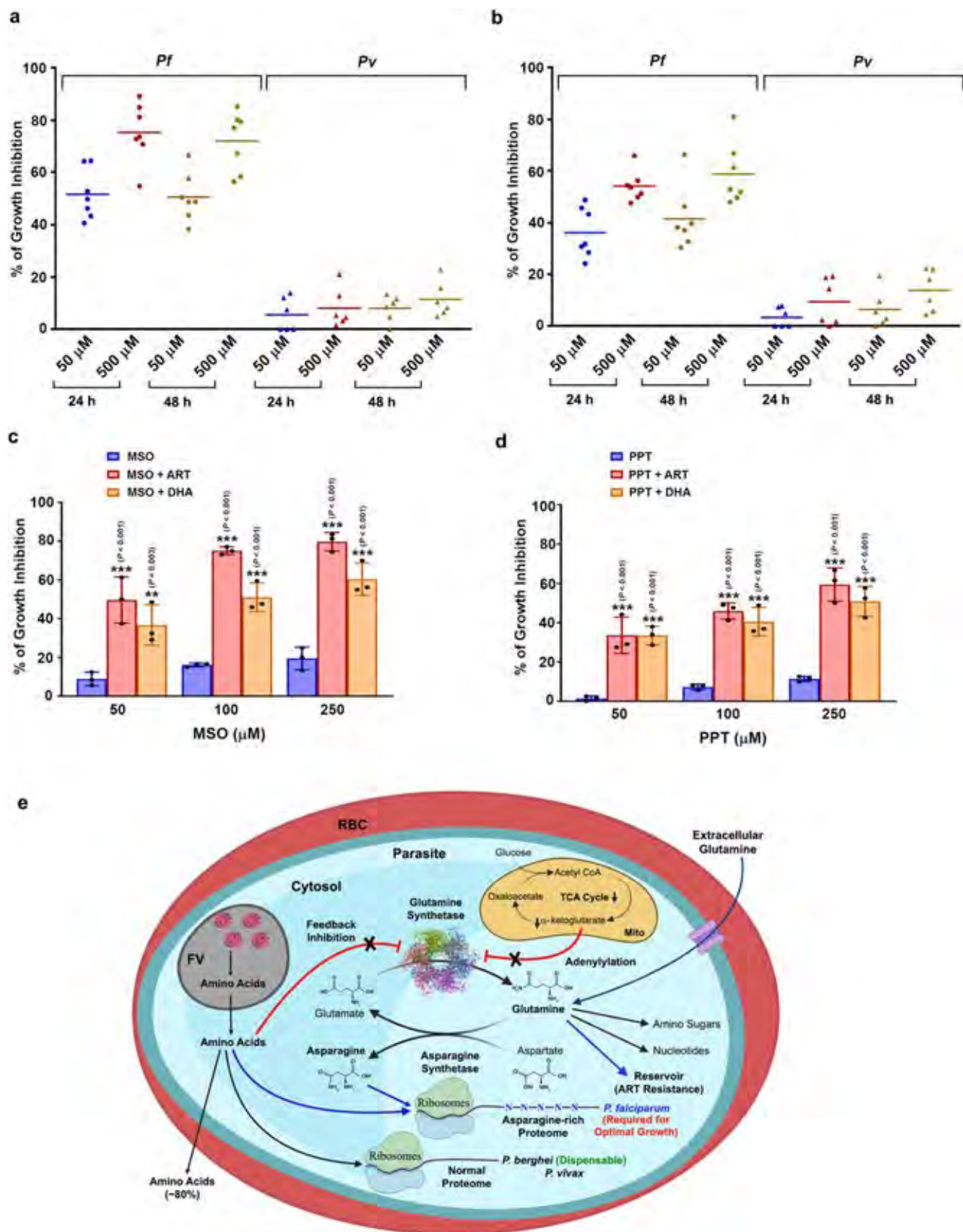
Homology modeling of *Plasmodium* GS

Three-dimensional structures of *Pv* and *Pb* GS are not available. Therefore, homology modeling of *Pv* and *Pb* GS were carried out using MODELLER v10.1. based on the cryo-EM structure of *Pf*GS (PDB ID: 6PEW). *Pv* and *Pb* GS showed 74.22% and 68.42% identity with *Pf*GS, respectively. We performed alignment of *Pv* and *Pb* GS with the available three-dimensional structures of *Pf* (PDB ID: 6PEW), *St* (PDB ID: 1F1H), *Mt* (PDB ID: 2WGS), and *Hp* GS (PDB ID: 5ZLP) using PRO-MALS3D. Ten models were built for *Pv* and *Pb* GS, and they were subsequently optimized using the variable target function method (VTFM) with conjugate gradient (CG) algorithm and then refined using molecular dynamics (MD) with simulated annealing (SA). The best

Fig. 10 | Effect of MSO and PPT on *Pf* and *Pv* clinical isolates and ART-resistant *Pf*Cam3.I[R539T] strain. a Effect of MSO on in vitro growth of *Pf* ($n = 7$) and *Pv* ($n = 6$) clinical isolates in RPMI[gln]. **b** Effect of PPT on in vitro growth of *Pf* ($n = 7$) and *Pv* ($n = 6$) clinical isolates in RPMI[gln]. A growth assessment was carried out based on ^{3}H-hypoxanthine uptake and verified by Giemsa-stained smears. **c** Effect of ART/DHA and MSO combination on the growth of ART-resistant *Pf*Cam3.I[R539T] parasites in RSA were performed with RPMI[gln] medium. The percentage of growth inhibition of ART/DHA and MSO combination treatment was determined at 96 h with respect to ART/DHA-treated parasites. The percentage of growth inhibition of MSO treatment alone was determined at 96 h with respect to untreated parasites. **d** Effect of ART/DHA and PPT combination on the growth of ART-resistant *Pf*Cam3.I[R539T] parasites in RSA were performed with RPMI[gln] medium. The percentage of growth inhibition of ART/DHA and PPT combination treatment was determined at 96 h with respect to ART/DHA-treated parasites. The percentage of growth inhibition of PPT treatment alone was determined at 96 h with respect to untreated parasites. Growth assessment was carried out based on ^{3}H-hypoxanthine uptake and verified by Giemsa-stained smears and flow cytometry. (mean ± SD; **$P < 0.01$, ***$P < 0.001$, Two-way ANOVA) $n = 3$ independent experiments. **e** Model depicting the distinct evolution of *Plasmodium* GS and its significance in *P. falciparum*. Lack of feedback inhibition by amino acids and absence of adenylylation in *Plasmodium* GS are represented. Blue arrows highlight the requirement of GS in supporting *Pf* asparagine-rich proteome and the role of glutamine as a reservoir of nitrogen source in ART-resistance. FV- food vacuole; Mito - mitochondrion; RBC - red blood cell. The model was created with BioRender.com.

models for *Pv* and *Pb* GS were chosen based on the molpdf scores. A close inspection of the generated structures revealed that the loops present in the first peptide inserts of *Pv* (Gly174-His196) and *Pb* GS (Va174-Ser206) were having knotting with the same loop of other monomeric units in the final dodecameric structure. Therefore, loop modeling and loop refinement were also performed using MODELLER v10.1. by generating 100 loop models to remove knotting. Each of the generated loops was incorporated in a monomeric unit that was superimposed on the dodecameric structure generated previously. Each of the generated structures was carefully analyzed to check for any loop entanglement, and the model that had no loop entanglement or bumping with a nearby monomeric unit was selected. The final model generated was then superimposed on *Pf*GS to examine the differences in C_α backbone of the model using PyMOL Molecular Graphics System, Version 1.2r3pre, Schrödinger, LLC. A similar procedure was also followed to model the first peptide insert of *Pf*GS that could not be observed in the cryo-EM structure.

Cloning, over-expression and purification of recombinant *Pf*, *Pb*, and *E. coli* GS

cDNA sequences of *Pf*GS (PF3D7_0922600) and *Pb*GS (PBANKA_0823500) were retrieved from PlasmoDB (https://plasmodb.org/plasmo/app). cDNA sequence of *E. coli* GS (CAD6154619.1) was retrieved from NCBI GenBank (https://www.ncbi.nlm.nih.gov/genbank/). Total RNA from *Pf*, *Pb* or *E. coli* was isolated using RNeasy Mini Kit (Qiagen, 74104) according to the manufacturer's protocol. cDNA synthesis was carried out with 1 μg of total RNA using RevertAid Reverse Transcriptase (Thermo Fisher Scientific, EP0442), followed by PCR with Phusion High-Fidelity DNA Polymerase (New England Biolabs, M0530). The following were the forward (F) and reverse (R) primers used: *Pf*GS (F): 5'-GCCA<u>GGATCC</u>ATGAAGTCCGTGAGTTTTTCAAATAATGC-3'; *Pf*GS (R): 5'-GCCC<u>AGATCT</u>CTAACATTCATAATATAAGTGATAATCATAAGCG-3'; *Pb*GS (F): 5'-GCCA<u>GGATCC</u>ATGAAATTTATCAGTTTTTCGAACCCAATCG-3'; *Pb*GS (R): 5'-GCCC<u>AGATCT</u>TTAAGATCCATAATACATGATAAATTCAGAAGG-3'; *E. coli* GS (F): 5'-GCAA<u>CTCGAG</u>ATGTCCGCTGAACACGTACTGACG-3'; and *E. coli* GS (R): 5'- GC<u>AAAAGCTT</u>TTAGACGCTGTAGTACAGCTCAAACTCTAC-3' (Sigma-Aldrich). The restriction sites used for cloning are underlined. cDNA products were digested with the respective restriction enzymes and cloned into pRSETA plasmid (Thermo Fisher Scientific). Recombinant protein expressions were carried out in *E. coli* Rosetta2DE3pLysS strain (Novagen). In brief, *E. coli* Rosetta2DE3pLysS cells transformed with recombinant plasmids were grown to an A_{600} of 1.0 at 30 °C and the protein induction was carried out at 18 °C for 12 h using 1 mM isopropyl-β-D-thiogalactoside (IPTG) (MP Biomedicals, 11IPTG0001). The recombinant proteins fused with 6xHis tag were purified using Ni^{2+}-NTA Agarose resin (Qiagen, 30210). In brief, the bacterial cell pellets expressing the recombinant proteins were resuspended in lysis buffer containing 50 mM Tris pH 8.0, 500 mM NaCl, 20% glycerol, 0.01% Triton X-100, 1 mM dithiothreitol and protease inhibitors, sonicated and centrifuged at 43,000 *g* for 1 h. The supernatant was separated and loaded onto a column packed with Ni^{2+}-NTA resin and

washed sequentially with lysis buffer containing 1, 10, and 50 mM imidazole. The recombinant proteins were then eluted with lysis buffer containing 150 mM imidazole. The purified protein was then dialyzed against 50 mM Tris pH 8.0, 50 mM NaCl and 20% glycerol. Protein estimation was carried out using Pierce BCA Protein Assay Kit (Thermo Fisher Scientific, 23225). The total yield of recombinant GS was around 0.25–0.50 mg per litre of bacterial culture.

Enzyme assays

Plasmodium and *E. coli* GS enzyme assays were carried out by performing HPLC analysis for glutamine formation as well as by quantifying the release of inorganic phosphate (P_i)[68,69]. The enzyme assays were carried out at 37 °C for 1 h in a total volume of 25 μl and the assay mixtures contained 50 mM Tris buffer pH 8.0 with 4 mM glutamate, 50 mM NaCl, 50 mM NH$_4$Cl, 10 mM ATP and 50 mM MgCl$_2$ and 0.5–1.0 μg of recombinant protein. The amino acids were extracted by vortexing the assay mixtures with 50 μl of water and 375 μl of acetonitrile, followed by incubation in ice for 30 min and centrifugation at 20,000 *g* for 20 min at 4 °C. The supernatant was collected, lyophilized and dissolved in 50 μl of water. 2.5 μl of the sample was subjected to pre-column derivatization with OPA reagent (Agilent, 5061–3335) by programming the auto-sampler and the separation of amino acids was carried out in Agilent 1260 Infinity HPLC System (Agilent Technologies) using a Poroshell 120 HPH-C18 column (4.6 mm × 100 mm X 2.7 μm) as per the manufacturer's protocol[70]. Mobile phase consisted of Solvent A: 10 mM Na$_2$HPO$_4$, and 10 mM Na$_2$B$_4$O$_7$, pH 8.2 and solvent B: methanol: acetonitrile: water (45:45:10 v/v). OPA-derivatized amino acids were detected using 1260 Infinity II Fluorescence Detector with excitation of 340 nm and emission of 450 nm. Amino acid standards (Agilent, 5061–3330) were used to determine the retention time. The standard curves were generated for glutamine and the assay products were also confirmed by spiking with glutamine. For every molecule of glutamine formed, one molecule of ATP is hydrolyzed to ADP and P_i. Therefore, the release of P_i was quantified as an indirect way of measuring glutamine synthesis and the activities were found to be comparable with HPLC assays. For P_i assays, the assay mixtures incubated at 37 °C for 1 h were diluted with water to 200 μl, followed by the addition of 30 μl of phosphate reagent of Phosphate Assay Kit (Abcam, ab65622). After vortexing, the absorbance was measured at 650 nm as per the manufacturer's protocol. The enzyme assays for r*Pf*GS-FKBP-GFP were carried out at 37 °C for 3 h. The enzyme activity of recombinant proteins was also verified after cleaving the 6xHis tag with enterokinase (New England Biolabs, P8070S). For enzyme assays carried out with parasite lysates of *Pf* or *Pb*, parasite pellets isolated by saponin lysis were resuspended in 200 μl of 50 mM Tris pH 7.5 containing 5 mM MgCl$_2$, 2 mM dithiothreitol and protease inhibitors, followed by a brief sonication for 15 s. The lysates were then centrifuged at 20,000 *g* for 20 min and the supernatants were separated. The assays were performed with the supernatants as described for the recombinant proteins with the inclusion of 200 μM phosphoenolpyruvate (Sigma-Aldrich, P0564) and 6 Units of pyruvate kinase (Sigma-Aldrich, P7768) to ensure the regeneration of ATP in the parasite

lysates[71]. The reaction mixtures were incubated at 37 °C for 6 h and the amino acids were extracted with acetonitrile as mentioned above for HPLC assays. For inhibition studies of recombinant proteins with MSO (M5379, Sigma) and PPT (45520, Sigma), recombinant proteins were pre-incubated with the respective inhibitors, ATP & MgCl$_2$ at 37 °C for 20 min, followed by the addition of NH$_4$Cl and glutamate, and subsequent incubation at 37 °C for 1 h. Feedback inhibition assays were carried out with 1 mM and 5 mM concentrations of glycine, alanine, serine, histidine, tryptophan, glutamine and AMP. For the mixture of all six amino acids at 5 mM concentrations, tryptophan alone was used at 2.5 mM concentration due to its limited solubility. Individual glutamate- and protein-omitted reactions were used as controls for all the assays.

Adenylylation analysis of recombinant and endogenous *Pf* and *Pb*GS

To examine the adenylylation of recombinant *Pf* and *Pb* GS, *E. coli* Rosetta2DE3pLysS strain transformed with the respective recombinant plasmid was grown at 30 °C for 6 h to an A$_{600}$ of 0.4-0.5 in LB medium containing 10 mM glutamine, followed by induction with 1 mM IPTG at 30 °C for another 6 h. Recombinant *Pf* and *Pb*GS protein inductions were successful at 30 °C, except for the total yield of soluble protein was approximately less by one third in comparison with protein induction at 18 °C. Recombinant *E. coli* GS protein induction was also carried out at identical conditions and the purification of all the three recombinant proteins was carried out in a similar fashion as mentioned above. Western blot analysis was carried out with AMP-Tyr specific mouse monoclonal antibodies (1:1000 dilution; clone 1G11)[72]. In brief, nitrocellulose membrane was blocked with 1X Roti-Block (Carl Roth, A151.2) for 3 h, followed by overnight incubation with primary antibodies in 1X Roti-Block containing 1 mM MnCl$_2$ at 4 °C. After developing, the same blot was stripped and reprobed with mouse monoclonal his-tag antibody (1:4000 dilution; Sigma-Aldrich, H1029). To examine the adenylylation of endogenous GS, parasite lysates were prepared by resuspending *Pf* or *Pb* pellets in 50 mM Tris pH 8.0 containing 100 mM NaCl, 2% glycerol, 0.1 % Triton X-100 and Halt protease inhibitor (Thermo Fisher Scientific, 78438), followed by sonication and centrifugation at 20,000 *g* at 4 °C. The endogenous GS present in the supernatants was immunoprecipitated by allowing it to bind with parasite GS-specific IgG purified from polyclonal sera raised against recombinant parasite GS using protein A magnetic beads (Thermo Fisher Scientific, 88845) and cross-linked with AminoLink Plus coupling resin using Pierce Co-Immunoprecipitation Kit (Thermo Fisher Scientific, 26149). The bound endogenous GS was eluted from cross-linked IgG using Elution buffer pH 2.8 as per the manufacturer's protocol. Western analysis for endogenous GS adenylylation was carried out as mentioned for recombinant proteins and recombinant *E. coli* GS was used as control in all these experiments.

Generation of ΔI$_1$r*Pf*GS, ΔI$_2$r*Pf*GS and ΔI$_1$I$_2$r*Pf*GS recombinant plasmids

To generate ΔI$_1$r*Pf*GS and ΔI$_2$r*Pf*GS recombinant plasmids, the two fragments on either side of the respective peptide inserts were PCR amplified individually and cloned sequentially into pRSETA plasmid. For ΔI$_1$r*Pf*GS plasmid construct, the following forward (F) and reverse (R) primers were used: *Pf*GS(F): 5'-GCCA<u>GGATCC</u>ATGAAGTCCGTGAG TTTTTCAAATAATGC-3' and ΔI$_1$*Pf*GS (R): 5'-GCAA<u>CTCGAG</u>ACTCGAT AAATCATTTTTACAAGAAAATGA-3' to amplify the first fragment; ΔI$_1$*Pf*GS(F): 5'-GCAA<u>CTCGAG</u>ATTAATGATGATAGTAAAAAAGTAAAGA AAAAA-3' and ΔI$_1$/I$_2$*Pf*GS(R): 5'-GCAA<u>GGTACC</u>CTAACATTCATAATATA AGTGATAATCATAAGC-3' to amplify the second fragment. For ΔI$_2$r*Pf*GS plasmid construct, the following forward (F) and reverse (R) primers were used: *Pf*GS(F): 5'-GCCA<u>GGATCC</u>ATGAAGTCCGTGA GTTTTTCAAATAATGC-3' and ΔI$_2$*Pf*GS(R): 5'-GCAA<u>CTGCAG</u>CGAAAAT

ATGCTTGAAATGTAGAAATGATT-3' to amplify the first fragment; ΔI$_2$*Pf*GS(F): 5'- GCAA<u>CTGCAG</u>GAACCACAAGGTATATCTTTTTCTCTTG TCG-3' and ΔI$_1$/I$_2$*Pf*GS (R): 5'- GCAA<u>GGTACC</u>CTAACATTCATAATATA AGTGATAATCATAAGC-3' to amplify the second fragment. The restriction sites used for cloning are underlined. To generate ΔI$_1$I$_2$r*Pf*GS recombinant plasmid having deletions for both the inserts, three fragments were sequentially cloned. The following forward (F) and reverse (R) primers were used: *Pf*GS (F): 5'-GCCA<u>GGATCC</u>ATG AAGTCCGTGAGTTTTTCAAATAATGC-3' and ΔI$_1$*Pf*GS (R): 5'-GCAA <u>CTCGAG</u>ACTCGATAAATCATTTTTACAAGAAAATGA-3' for the first fragment; ΔI$_1$*Pf*GS (F): 5'-GCAA<u>CTCGAG</u>ATTAATGATGATAGTAAAA AAGTAAAGAAAAAA-3' and ΔI$_2$*Pf*GS (R): 5'-GCAA<u>CTGCAG</u>CGAAAAT ATGCTTGAAATGTAGAAATGATT-3' for the second fragment; ΔI$_2$*Pf*GS (F): 5'- GCAA<u>CTGCAG</u>GAACCACAAGGTATATCTTTTTCTCTTGTCG-3' and ΔI$_1$/I$_2$*Pf*GS (R): 5'- GCAA<u>GGTACC</u>CTAACATTCATAATATAAGTGAT AATCATAAGC-3' for the third fragment. ΔI$_1$r*Pf*GS and ΔI$_2$r*Pf*GS recombinant plasmids were further subjected to site-directed mutagenesis for removing the additional amino acids that were introduced into the GS sequence due to the restriction sites used for cloning. For this, PCR reactions were performed using the following set of primers: 5'- TCATTTTCTTGTAAAAATGATTTATCGAGTTATTTAATTAATGATGA TAGTAAAAAAGTAAAGAAA-3' and 5'- TTTCTTTACTTTTTTACTATCA TCATTAATTAAATAACTCGATAAATCATTTTTACAAGAAAATGA-3' for ΔI$_1$r*Pf*GS; 5'-TCAAGCATATTTTCGGAACCACAAGGTATATCTTTTTCTC TTGTCGAAAGTTTAGATGCTTTGGA-3' and 5'-TATACCTTGTGGTTC CGAAAATATGCTTGAAATGTAGAAATGATTATCTTTACTTTCAAATGG AA-3' for ΔI$_2$r*Pf*GS. All the primers were procured from Sigma-Aldrich. The purified PCR products were then subjected to *DpnI* restriction digestion, followed by transformation. DNA sequencing was carried out to ensure the precise deletion of the peptide inserts in the respective recombinant plasmids. Recombinant protein expressions were carried out as described for r*Pf*GS.

Analytical size-exclusion chromatography

The oligomeric status of purified r*Pf*GS and ΔI$_1$r*Pf*GS was analyzed by analytical size-exclusion chromatography performed with AKTA pure protein purification system using Superose 6 10/300 GL column (Cytiva, 17-5172-01) at 4 °C. The recombinant proteins (0.15 mg) were exposed to 37 °C or 42 °C for 15 min, and subjected immediately to size-exclusion chromatography at a flow rate of 0.15 ml/min in buffer containing 25 mM Tris pH 8.0, 300 mM NaCl and 5% glycerol. Elution fractions of 300 μl volume were collected for the entire run of 3 h and the appropriate fractions showing the eluted protein peaks were analyzed by Western blot using anti-his tag antibodies.

MD simulations

To check the dynamic behavior of *Pf*GS and ΔI$_2$*Pf*GS, MD simulations were performed. Since the active site is formed between two adjacent subunits, we used four subunits - two each from upper and lower hexamers of the dodecameric structure. This strategy was preferred due to the difficulties experienced with the stability of dodecameric *Pf*GS in MD simulations. The preliminary topologies and coordinates for the protein complexes were generated in VMD 1.9.3 using CHARMM34 force field. MD simulations were done using NAMD 2.9. The structures of *Pf*GS and ΔI$_2$*Pf*GS were solvated in a rectangular water box (TIP3P) with a buffering distance of 10 Å. Ions (Na$^+$ and Cl$^-$) were added to ensure the electro-neutrality of the solvated system. Prior to the simulation, each of the system was properly minimized with a stepwise minimization protocol. The water molecules and ions were minimized first, followed by hydrogen atoms and side chains of the protein complex. The side chains were minimized for 100000 steps while the backbone atoms and the bond lengths of hydrogen atoms were kept fixed. Thereafter, all the atoms were allowed to relax freely and the whole system was energy-minimized for 100000 steps with nominal restraints on C$_\alpha$ and backbone atoms

(10 kcal/mol) to prevent any abrupt change in the structure. Subsequently, an equilibration protocol was followed where the system was heated gradually from 0–310 K in steps of 30 K with a canonical ensemble (NVT). At each step, a 20-picosecond (ps) simulation was run to allow the system to adjust to the temperature. Once the system attained 310 K, isobaric and isothermic ensemble (NPT) was applied for a period of 100 ps with a constant pressure of 1.0 bar using Langevin dynamics. Finally, the applied restraints on C_α atoms were removed and the system was equilibrated for 1 ns at 310 K using Langevin piston coupling algorithm. During the whole simulation, the Particle Mesh Ewald (PME) sum algorithm was used to calculate the long-range electrostatic interactions with fixed periodic boundary conditions. The covalent interactions involving hydrogens were constrained using SHAKE algorithm. The production run was done for a time period of 100 ns. The analyzes of the MD trajectories were performed to examine the structure and dynamic behavior of the complexes during MD. The trajectories were analyzed for RMSD, RMSF, hydrogen bonds, and SASA.

In vitro maintenance of *P. falciparum* cultures

Routine maintenance of *Pf*3D7 cultures were carried out at 37 °C in RPMI-1640 medium (Gibco, 23400-013) containing 0.5% AlbuMAX-II (Thermo Fisher Scientific, 11021037) using O^{+ve} RBCs of 5% hematocrit under 90% N_2, 5% O_2 and 5% CO_2. The parasites were subcultured with fresh RBCs when the culture parasitemia reached around 2–5%. Synchronization of *Pf* cultures was carried out with 5% D-sorbitol (w/v) (Sigma-Aldrich, 240850). Parasites were isolated by treating the infected RBC pellet with equal volume of 0.15% saponin in PBS (w/v) (Sigma-Aldrich, S4521) followed by centrifugation at 10,000 *g* for 10 min at 4 °C. The isolated parasites were washed thoroughly with ice cold PBS for four times to remove the carry-over of proteins from RBC lysates[73]. ART-resistant *Pf*Cam3.I[R539T] strain was also maintained in a similar fashion. *Pf* strains were cryopreserved by storing them under liquid nitrogen in storage medium containing 28% glycerol, 3% D-sorbitol and 0.65% NaCl and the glycerolyte stocks were revived following the standard protocol recommended by Malaria Research and Reference Reagent Resource Center (MR4). The experiments involving gametocyte formation were carried out with freshly revived glycerolyte stocks that were not passaged for more than five asexual cycles. Giemsa-stained smears were routinely prepared to examine the parasite growth and parasitemia. Parasite growth assessment for experiments was carried out by Giemsa-stained smears, flow cytometry and ^{3}H-hypoxanthine uptake[74]. Flow cytometry was performed by staining the infected RBCs with 0.5X SYBR Green I (Thermo Fischer Scientific, S7563) in HBSS buffer pH 7.4 containing 2% FBS (Gibco, 10270106) for 30 min at 37 °C. The data was acquired using BD LSRFortessa (BD). ^{3}H-hypoxanthine uptake assays were performed by adding ^{3}H-hypoxanthine (American Radiolabeled Chemicals, Inc., ART 0266) (5 µCi per ml culture volume) to the cultures. The labeled cultures were then washed with RPMI-1640 medium, lysed in water, and harvested on glass fibre filters using FilterMate cell Harvester (PerkinElmer). After washing with water, the glass fibre filters were dried and placed in Ultima Gold XR scintillation cocktail (PerkinElmer, 6013111). The radioactive counts were measured using MicroBeta^2 Microplate Counters (PerkinElmer). Glutamine-free RPMI was procured from Thermo Fisher Scientific (Gibco, 42401-018) and for experiments carried out at physiological concentrations of glutamine, glutamine-free RPMI-1640 was reconstituted with 0.5 mM glutamine (Sigma-Aldrich, G8450). Gametocyte induction for *Pf*3D7 cultures was carried out by crash method as described by treating them with 50 mM N-acetylglucosamine for 72 h when the parasitemia reached around ~6%[75].

Routine propagation of *P. berghei* in mice

Pb ANKA strain was routinely propagated in 7–8 weeks old male/female Balb/c mice. The experiments were initiated by injecting 10^5 parasites through intraperitoneal route and the parasite growth was monitored by examining the Giemsa-stained smears prepared from tail vein blood under light microscope. For cerebral malaria experiments, 7–8 weeks old C57BL/6 male/female mice were used and the infections were initiated by injecting 10^5 parasites. The sex of the mice did not alter the asexual parasite growth, gametocyte development, animal mortality, and disease pathogenesis, and the results were reproducible in both male and female mice. Balb/c and C57BL/6 mice were bred in-house and maintained at the animal house facility of the Institute of Life Sciences, Bhubaneswar, under standard conditions of 25 +/−3 °C temperature, 40–50% relative humidity, and 12 h light / 12 h dark cycle. The development of cerebral pathogenesis in mice was monitored by examining the neurological symptoms such as ataxia, paralysis, convulsion, and coma, and the associated early mortality within day 10 when the peripheral blood parasitemia was around 20%. The integrity of blood-brain barrier was assessed by quantifying the Evans blue extravasation in the brain of infected mice after one hour of injecting 200 µl of 2% Evans blue in PBS intravenously. Evans blue from the brain samples was extracted by incubating them in formamide at 37 °C for 48 h and measuring the absorbance at 620 nm[76]. The isolation of *Pb* parasites from infected RBCs was carried out by saponin lysis.

Maintenance of *Anopheles stephensi* mosquitoes

A. stephensi mosquito colony was reared under standard insectary conditions maintained at 27 °C and 75–80% humidity supported with a 12 h light and dark photo-cycle as described[8,73]. Adult female mosquitoes of 5–7 days old were blood fed on anesthetized Balb/c male/female mice of 8–12 weeks old for the production of eggs. The eggs were collected on damp filter paper and placed for hatching. The larvae were reared in water containing 0.03% (w/v) sea salt (Sigma-Aldrich, S9883), 0.01–0.02% (w/v) yeast powder and liver powder at a density of one larva/ml following the standard procedures. The pupae were separated and kept inside the cages for adult emergence. The adult mosquitoes were fed with 10% sucrose (Merck, 107687) solution containing 0.05% paraminobenzoic acid (Sigma-Aldrich, A9878).

Immunofluorescence analysis

Immunofluorescence analysis for asexual stages, gametocytes, ookinetes, and sporozoites was carried out by fixing the cells with 4% paraformaldehyde and 0.0075% glutaraldehyde, followed by permeabilization with 0.1% Triton X-100 and subsequent treatment with 0.1 M glycine. Blocking was performed with PBS containing 2% BSA for 3 h. The incubation for primary antibodies was carried out in the same blocking buffer for 6 h, followed by the addition of secondary antibodies for 3 h[77]. For the oocyst, the mosquito gut was fixed with 4% paraformaldehyde and permeabilized with 0.1% Triton-X-100, followed by blocking in 4% BSA[78]. For exo-erythrocytic stages, HC-04 cells infected with sporozoites were fixed with 4% paraformaldehyde, permeabilized with 0.01% Triton X-100 and blocked with PBS containing 1% BSA[79]. Parasite GS-specific polyclonal sera were used at 1:250 dilution. Anti-UIS4 antibody (Origene, AB0042-200) was used at 1:1000 dilution. FITC-conjugated donkey anti-mouse IgG (Thermo Fisher Scientific, A24501) was used at 1:250 dilution. Rabbit anti-goat AF594 (Thermo Fisher Scientific, A-11080) was used at 1:400 dilution. Images were captured with 20x/60x/100x objectives using Olympus IX83 microscope with DP73 high-performance camera.

Generation of *Pf*GS^{cKS} parasites and performing conditional knock sideways

For generating *Pf*GS^{cKS} parasites, C-terminal portion of *Pf*GS representing 1245–2069 bp (without stop codon at the end) was cloned into pSLI-2xFKBP-GFP plasmid for in-frame fusion with FKBP and GFP[37]. The following were the forward (F) and reverse (R) primers used: *Pf*GS^{cKS} (F): 5′-GCATG<u>CGGCCGC</u>TAAATATTCTATCATAATGATCCTTCTACTT TC-3′ and *Pf*GS^{cKS} (R): 5′-CGAT<u>CCTAGG</u>ACATTCATAATATAAGTGATA

ATCATAAGC-3' (Sigma-Aldrich). The restriction sites are underlined. 50 µg of the plasmid construct was nucleofected into purified mature schizonts of *Pf*3D7 using P3 primary cell 4D-Nucleofector™ X Kit L (Lonza, V4XP-3024), and the parasites having episomal plasmid were selected after 24 h with 4 nM WR99210 (Jacobus Pharmaceutical Company Inc.). When the parasitemia reached around 2%, the selection of the integrated parasites was carried out by the addition of 400 µg G418 per ml of culture volume (Gibco, 1181031). The in-frame fusion of GS with FKBP and GFP in the selected parasites was confirmed by genomic DNA PCR, RT-PCR, Western and fluorescence analyses. To mislocalize *Pf*GS by conditional knock sideways, *Pf*GS^cKS parasites were nucleofected with 50 µg of mislocalizer pLyn-FRB-mCherry plasmid, followed by selection with 2 µg of Blasticidin-S (Thermo Fisher Scientific, R21001) per ml of culture volume. The presence of mislocalizer plasmid was confirmed by examining the mCherry fluorescence in live parasites and its membrane localization. The mislocalization of *Pf*GS was induced by the addition of 250 nM rapamycin (Sigma-Aldrich, R0395) and verified by the translocation of GFP fluorescence from the parasite cytosol to the plasma membrane in live parasites. For experiments involving gametocytes, *Pf*GS^cKS cultures were synchronized and gametocytes were induced by the crash method. When the culture parasitemia reached around 6%, 50 mM N-acetyl-D-glucosamine (Sigma-Aldrich, A3286) was added along with 250 nM rapamycin, and continued for four days after which, the addition of N-acetyl-D-glucosamine was stopped. The mislocalization of *Pf*GS in the gametocytes was also confirmed by fluorescence analysis and the formation of different stages of gametocytes was quantified by examining morphology and counting their numbers in Giemsa-stained smears.

Generation of *Pf*GS^HA-DD parasites for conditional knockdown

For generating *Pf*GS^HA-DD parasites, C-terminal portion of *Pf*GS representing 909–2069 bp (without stop codon at the end) was amplified and cloned into pHADD plasmid[38] for in-frame fusion with HA and destabilization domain (DD). The following forward and reverse primers were used: 5'- GCCACCGCGGGGATGATAGTAAAAAAGTAAAGAA AAAATCCGG-3' and 5'-GCCCGGTACCACATTCATAATATAAGTGATA ATCATAAGCG-3' (Sigma-Aldrich). The C-terminal portion of *Pf*GS with in-frame fusion of HA and DD was then amplified with the following forward and DD-specific reverse primers: 5'-GCAAGCGGCCGCGATGA TAGTAAAAAAGTAAAGAAAAAAATCCGG-3' and 5'-GCAAGTCGACAGG TTCCGGTTTTAGAAGCTCCACA-3' (Sigma-Aldrich). The restriction sites are underlined. The resultant fragment was cloned into pSLI-TGD plasmid replacing the GFP present in the plasmid. The plasmid was then nucleofected into purified mature schizonts of *Pf*3D7. Parasites having episomes were selected after 24 h with 4 nM WR99210 (Jacobus Pharmaceutical Company Inc.), followed by selection with G418 (400 µg/ml) for parasites having proper integration. The in-frame fusion of GS with HA and DD was confirmed by genomic DNA PCR, RT-PCR and Western analyzes. *Pf*GS^HA-DD cultures were continuously maintained in the presence of 0.5 µM Shield-1 since transfection (Takara Bio, 632189) and the extent of GS degradation was examined by the removal of Shield-1.

Generation of *Pb*GSKO parasites

Deletion of GS in *Pb* ANKA parasites was carried out by double cross-over recombination. In brief, PCR was carried out to amplify the 5'- and 3'-UTRs of GS from *Pb* genomic DNA. The following were the forward (F) and reverse (R) primers used: 5'-UTR (F): 5'-GCCAGGGCCCGC ATGCTCCGAAATTGATACTCTGCATG-3'; 5'-UTR (R): 5'-GCCCAGATCT TTTGAAAAATAGGAAAAGTAAATAATATATGATGCG-3'; 3'-UTR (F): 5'-GCCAGGTACCCCAAAAGCACATACACTGTAATTTGCACTC-3'; and 3'-UTR (R): 5'-GCCCGCGGCCGCTATTCAAATGATTAAGAGGTGGCATAT AATAAATG-3' (Sigma-Aldrich). The resultant 5'- and 3'-UTR fragments were digested with *ApaI* and *BglII*, and *KpnI* and *NotI*, respectively, and

cloned into *pL0006* plasmid. The plasmid construct was then digested with *ApaI* and *NotI*, followed by the purification of linear product containing hDHFR selection marker flanked on either side by 5'- and 3'-UTRs of *Pb*GS. The linear product was nucleofected into purified mature schizonts of *P. berghei* ANKA using P5 primary cell 4D-Nucleofector™ X Kit L. (Lonza, V4XP-5024). The nucleofected parasites were injected intravenously into 7-8 weeks old naïve BALB/c mice, followed by pyrimethamine selection (70 mg/L in drinking water). The selected parasites were then subjected to limiting dilution and *Pb*GSKO phenotype was verified with two independent clones. Targeted deletion of GS in *Pb*GSKO parasites was confirmed by genomic DNA PCR and RT-PCR using *Pb*GS-specific primers, and by Southern and Western analyzes. For Southern analysis, genomic DNA isolated from *Pb*WT and *Pb*GSKO parasites were digested with *EcoRI* and *AflII*, resolved on 0.7% agarose gel and transferred to nylon membrane. Digoxigenin (DIG) labeled probe for *Pb*GS 3'-UTR was prepared by PCR amplification with 3'-UTR forward and reverse primers using DIG DNA Labeling Kit (Roche, 11093657910). Hybridization of the DIG-labeled probe and its detection were carried out using DIG Luminescent Detection Kit (Roche, 11363514910) as per the manufacturer's protocol.

Sexual and liver stage development studies of *P. berghei*

To initiate the sexual stage development of *Pb* in *A. stephensi* mosquitoes, adult female mosquitoes of 5–7 days old were allowed to feed on mice infected with *Pb*WT or *Pb*GSKO parasites on day 8 post-infection when the blood parasitemia was around 5–10% with at least two exflagellation centers per field. The fully engorged mosquitoes were segregated and maintained at 19 °C and 75–80% humidity. At 20 h post-feeding, the blood bolus was collected from the infected mosquitoes to examine the ookinete formation and quantify the number of ookinetes. On day 10 post-feeding, the infected mosquito guts were dissected out and subjected to mercurochrome staining for determining the number of oocysts formed. On day 17 post-feeding, the salivary glands of the infected mosquitoes were dissected to examine the number of sporozoites present. In vivo liver stage development was assessed by injecting sporozoites intravenously into naïve Balb/c mice and examining for the appearance of blood-stage infections. For in vitro exflagellation analysis, 2.5 µl of tail vein blood was collected in the exflagellation medium of RPMI-1640 pH 8.0 containing 100 µM xanthurenic acid (Sigma-Aldrich, D120804) and 10% heat-inactivated FBS and incubated at 19 °C for ~12 min, followed by immediate counting of exflagellation centers by light microscopy. In vitro ookinete formation analysis was performed by examining the Giemsa-stained smears prepared from the blood that was collected in exflagellation medium and incubated at 19 °C for 22 h[8,73]. For in vitro exoerythrocytic stage development studies, salivary glands were dissected under aseptic conditions and sporozoites were collected in DMEM/F-12 medium (Gibco, 12500039) containing 10% heat-inactivated FBS with penicillin-streptomycin (Gibco, 15140122). The isolated sporozoites were added to HC-04 cells (MRA-975) of 60–70% confluency, followed by the removal of culture supernatant after 3 h of sporozoite addition. The cells were then washed with medium and maintained at 37 °C for 52 h in a CO_2 incubator to examine the formation of exo-erythrocytic stages[79].

MSO and PPT inhibition studies in *Pf* and *Pb*

In vitro inhibition, studies were carried out either in RPMI-1640 lacking L-glutamine (RPMI^-gln) or RPMI-1640 medium containing physiological concentrations (0.5 mM) of L-glutamine (RPMI^Pgln). MSO/PPT treatment was carried out in synchronized *Pf* cultures containing late rings and early trophozoites and the parasite growth was monitored for 24 h and 48 h by examining Giemsa-stained smears and by performing flow cytometry and ³H-hypoxanthine uptake. ³H-hypoxanthine was added to the cultures after 3 h of MSO/PPT addition. For in vitro *Pb*

experiments, synchronized infections were initiated in naïve Balb/c mice and the infected blood was collected around 08:00 h in the morning when the parasites were predominantly in the early rings. After removing the plasma and buffy coat, the infected RBCs were washed either with glutamine-free or glutamine-containing RPMI-1640 with 10% FBS. The infected RBCs were resuspended in the respective RPMI-1640 medium to 5% hematocrit and MSO/PPT was added. ^{3}H-hypoxanthine addition was carried out after 3 h and MSO/PPT treatment was performed for 18 h at 37 °C with intermittent mixing of the cultures at 1 h intervals. Since Pb has a 24 h life cycle in comparison with 48 h of Pf and the released Pb merozoites do not efficiently invade fresh RBCs in vitro, prolonged labeling studies could not be performed. Orotic acid (Sigma-Aldrich, O2750) and D-glucosamine hydrochloride (Sigma-Aldrich, G4875) supplementations for in vitro Pf cultures were carried out by adding them along with MSO/PPT. For in vivo treatment of PbWT-infected mice with MSO/PPT, the inhibitors were dissolved in saline and injected intraperitoneally for four consecutive days at 10:00 h starting from day 4 post-infection. The parasite growth was examined by measuring the peripheral blood parasitemia in Giemsa-stained smears prepared from tail vein blood.

Protein and RNA labeling

In vitro protein labeling studies for MSO/PPT treated Pf and Pb cultures were carried out by adding 100 μCi of ^{35}S-Methionine and Cysteine mix (Invivo ProTwin Label (LCS-8), BRIT) to 4 ml culture volume at 3 h post-addition of MSO/PPT. After 9 h of radiolabelling, parasites were isolated by saponin lysis, resuspended in 50 mM Tris pH 8.0 containing 100 mM NaCl, 2% glycerol, and 0.1 % Triton X-100, and lysed by sonication. The lysates were resolved on 10% SDS-PAGE gel and phosphorimager scanning was carried out to examine the radiolabelling of proteins using Amersham Typhoon 5 Biomolecular Imager. In parallel, 10 μl of the lysates were spotted on Whatman filter paper grade I, dried and washed subsequently with hot and cold 10% (w/v) trichloroacetic acid to remove free amino acids and charged-tRNAs, followed by diethyl ether to remove lipids. The filter papers were then placed in Ultima Gold XR scintillation cocktail and the radioactive counts were measured using MicroBeta^2 Microplate Counters. For in vitro RNA-labeling studies, Pf cultures were treated with MSO/PPT followed by the addition of 100 μCi ^{32}P-orthophosphoric acid (LCP-32, BRIT) to 4 ml culture volume at 3 h post-addition of MSO/PPT. After 9 h of radiolabelling, parasites were isolated by saponin lysis, and total RNA was extracted using RNeasy Mini Kit (Qiagen, 74104) according to the manufacturer's protocol. Total RNA was then resolved on 1.2% agarose gel and transferred to a nylon membrane. The membrane was dried and phosphorimager scanning was carried out using Amersham Typhoon 5 Biomolecular Imager. In parallel, 10 μl of the RNA was spotted on glass fibre filter and placed in an Ultima Gold XR scintillation cocktail, and the radioactive counts were measured using MicroBeta^2 Microplate Counters. All these experiments were performed with identical parasitemia and hematocrit between the untreated and treated groups by equally splitting the infected cultures or infected-mouse blood.

Estimation of aspartate, glutamate, asparagine, and glutamine levels in Pf and Pb parasites

The levels of aspartate, glutamate, asparagine, and glutamine in Pf and Pb pellets treated with MSO were estimated by HPLC as well as by LC-MS/MS. 10 ml of synchronized Pf cultures having ~2% parasitemia were treated with MSO for 12 h when the parasites were predominantly in late rings and early trophozoites, followed by saponin lysis to isolate the parasites. PbWT and PbGSKO parasites were also isolated by saponin lysis from infected mice when the blood parasitemia was around 5%. Parasite pellets were then extracted with 10 volumes of 50% methanol in water (v/v), followed by lyophilisation and solubilizing the lyophilized extracts with 50 μl of water[80]. For HPLC, the extracts were

derivatized with OPA, separated on Poroshell 120 HPH-C18 column (4.6 mm × 100 mm X 2.7 μm) using Agilent 1260 Infinity HPLC System as mentioned for the recombinant protein assays. The peak areas of the MSO-treated samples with respect to the untreated controls or PbGSKO samples with respect to PbWT samples were used to measure the fold changes of aspartate, glutamate, asparagine, and glutamine. To compensate the variations that arise because of the changes in parasite yield, the data were normalized with the average fold changes of the peak areas obtained for at least five different amino acids - arginine, serine, histidine, threonine, and tyrosine that showed unambiguous separation in HPLC. For LC-MS/MS, the parasite extracts were derivatized with 6-aminoquinolyl-N-hydroxysuccinimidyl carbamate (AQC), cleaned up with SPE and dried under vacuum, followed by reconstitution with 50 μl of 0.5% acetonitrile containing 0.1% formic acid. 10 μl of the sample was used for LC-MS/MS analysis carried out in Acquity C18 column (1.8 μm, 2.1 mm × 100 mm) using Dionnex Ultimate3000 UHPLC system coupled with Q Exactive mass spectrometer (Thermo Fisher Scientific). Mobile phase consisted of Solvent A: 10 mM ammonium acetate containing 0.1% formic acid and solvent B: acetonitrile containing 0.1% formic acid. Mass spectrometry was performed under spray voltage of 4000/2500 V with vaporizer temperature of 250 °C, sheath gas, and auxillary gas flow rate of 30 and 10 Arb, respectively. The acquisition was performed in Parallel Reaction Monitoring mode at 35,000 resolution with a normalized collision energy of 25 eV. The calibration curves were prepared for the individual amino acids and the samples were spiked with internal standards containing deuterated amino acids. The fold changes of aspartate, glutamate, asparagine, and glutamine were calculated based on their relative abundances in MSO-treated and untreated controls or PbGSKO and PbWT samples, after normalizing with the average fold changes of the relative abundances obtained for arginine, serine, histidine, threonine and tyrosine.

eIF2α phosphorylation in Pf and Pb parasites

Pf3D7 cultures were subjected to two rounds of tight synchronization within a span of 3 h in the previous cycle, followed by one additional synchronization in the subsequent cycle immediately after RBC invasion. After 3 h post-invasion, ring stage parasites were treated for 6 h with 250 μM MSO in RPMI^{-gln} medium. For eIF2α phosphorylation analysis in PbWT and GSKO parasites, infected mouse blood of similar parasitemia predominantly containing the ring stages was incubated in vitro with 250 μM MSO for 6 h in RPMI^{-gln} medium. The parasite pellets were then prepared by saponin treatment and lysed with 0.5x PBS containing 0.5% Triton X-100, Halt protease inhibitor and Phos-STOP (Roche, 4906845001). Western blot analysis was performed with phosphorylated eIF2α (#3398, Cell Signaling Technology) and total eIF2α (#9722, Cell Signaling Technology) antibodies.

Proteomics analyzes

To examine the proteome of MSO-treated Pf parasites, proteins were extracted from the untreated and MSO-treated parasite pellets of two independent experiments. For each experiment, two different sets of untreated and MSO-treated cultures synchronized for late ring stages were treated with 50 μM MSO for 12 h. The untreated and MSO-treated parasite pellets isolated by saponin treatment were pooled separately during solubilization with 6 M urea in 25 mM ammonium bicarbonate buffer. The solubilized protein samples were then treated with DTT and iodoacetamide, and the urea concentration was decreased to 0.6 M by diluting with 25 mM ammonium bicarbonate. In-solution trypsin digestion was carried out overnight at 37 °C for 300 μg total protein using TPCK-treated trypsin (Sigma-Aldrich, 4352157). LC-MS/MS was performed with microflow reverse-phase LC in Eksigent Ekspert Nano LC 425 system (SCIEX) that was directly connected to a tandem quadrupole time-of-flight SCIEX TripleTOF 5600 + ESI-mass spectrometer. SCIEX Micro Trap Cartridge (Chrome XP; C18-CL, 5-μm,

120-Å pore size) was used to concentrate the samples. 0.1% (v/v) formic acid and 2% (v/v) acetonitrile in water was used to wash the trap cartridge, followed by the separation of the concentrated peptides using a SCIEX capillary reverse-phase column (ChromeXP, 3C18-CL-120, 3 μm, 120 Å and 0.3 × 150 mm). The flow rate was set at 5 μl/min and the run was carried out using the following solvents: solvent A − 98% water and 2% acetonitrile containing 0.1% formic acid (v/v), and solvent B − 98% acetonitrile and 2% water containing 0.1% formic acid (v/v). The gradient followed was 2 to 50% of solvent B for 28 min, followed by 50 to 90% of solvent B for 1 min, sustaining 90% of solvent B for 3 min, and then 90 to 5% of solvent B for 0.5 min with a final re-equilibration with 2% of solvent B for 2.5 min. Mass spectra and tandem mass spectra were recorded in positive-ion and high-sensitivity mode with a full scan resolution of 35,000 (full width at half maximum). The following parameters were used for ion source: IonSpray Voltage Floating (ISVF) = 5500; Ion Source Gas 1 (GS1) = 25; Ion Source Gas 1 (GS2) = 22; Curtain Gas Flow (CUR) = 30. The precursor ions were fragmented with nitrogen gas in a collision cell. 100 fmol beta-galactosidase digest (SCIEX) was used to calibrate TOF MS and TOF MS/MS spectra. The peptide spectra were recorded over a mass/charge (m/z) range of 350 to 1250, and MS/MS spectra were recorded over an m/z range of 150 to 1600 in data-dependent acquisition (DDA) mode. Analyst TF1.7.1. software was used for data acquisition and DDA was performed to obtain MS/MS spectra for the 15 most abundant parent ions following each survey MS1 scan (250-ms acquisition time per MS1 scan and 50-ms acquisition time per MS/MS). Dynamic exclusion features were set to an exclusion mass width of 50 mDa and an exclusion duration of 6 s. Paragon algorithm (ProteinPilot Software Version 5.0.2, SCIEX) was used to annotate MS/MS data against the reference proteomes of *Plasmodium falciparum* (UP000001450, Taxonomy: 36329; UP000030688, Taxonomy: 57266; UP000054282, Taxanomy: 57267; UP000054289, Taxonomy: 137071; UP000030673, Taxonomy: 5843; UP000019103, Taxonomy: 57270; UP000232684, Taxonomy: 5843) available at Uniprot (https://www.uniprot.org/) with the following parameters: TripleTOF 5600 instrument; alkylation of cysteines by iodoacetamide; trypsin enzyme digestion; ID Focus on biological modifications and the detected protein threshold [Conf] set at >10%. Peptides identified with ≥95 confidence were selected to calculate the fold change from the cumulative peptide intensities of the respective proteins. Cumulative peptide intensities of the identified proteins were normalized with respect to parasite actin I before determining Log_2FC values. The mass spectrometry proteomics data of LC-MS/MS have been deposited to the ProteomeXchange Consortium via the PRIDE partner repository with the dataset identifier PXD032797. Functional classification of the proteins was performed based on gene ontologies available at PlasmoDB.

Nucleotide analyzes
ATP, GTP, CTP, UTP, AMP, GMP, CMP, and UMP levels of untreated control and MSO-treated *Pf*3D7 parasites were assessed from three independent experiments. For this, 20 ml of synchronized *Pf* cultures having ~3% parasitemia were treated with 50 μM MSO for 12 h when the parasites were predominantly in the late ring stages. Parasites were isolated by saponin lysis and nucleotides were extracted by adding 10 volumes of 0.5 M perchloric acid to the parasite pellets, followed by vortexing and incubating on ice for 20 min. The extracts were neutralized with 2.5 M potassium hydroxide and incubated for 20 min in ice. The extracts were then centrifuged at 16,000 *g* for 15 min at 4 °C and the supernatants were filtered through Amicon Ultra (0.5 mL-10 kDa) centrifugal filter at 16,000 *g* for 15 min at 4 °C[81,82]. The filtrate (~100 μl) was immediately frozen in liquid nitrogen and stored at −80 °C. LC-MS analyzes were performed by injecting 10 μL of the sample into a Shimadzu Prominence-I HPLC (Shimadzu Corporation, Kyoto, Japan) interfaced with Shimadzu triple quadrupole LCMS-8045 mass

spectrometer (Shimadzu Corp.). For LC separation, samples were run on Shim-pack GIST column (C18, 75 mm × 4.6 mm, 5 μm) at a flow rate of 0.8 mL/min with slight modifications[83]. The solvents used were 0.1 % formic acid in water (A) and 100% acetonitrile (B) with a 100–80% gradient of A from 0–8 min, followed by 80–20% from 8–15 min, 20% from 15–18 min, 20–80% from 18–22 min, 80–100% from 22–24 min, and 100% from 24–26 min. The electrospray ionization (ESI) was performed in both positive and negative ion modes using following parameters: nebulizing gas flow = 3 L/min, heating gas = 10 L/min, interface temperature = 300 °C, drying gas flow = 10 L /min and DL temperature = 250 °C. Full-scan mass spectra were acquired over a mass range of m/z 50–1900. Processing, visualization, and analysis of mass spectrometry data were carried out using MZmine Version 2.53. Mass detection noise level was set to 1.0E1 in centroid mode and peak lists were generated with a minimum time span of 0.05 min and m/z tolerance of 0.01 m/z. Chromatogram deconvolution was achieved with a minimum peak height of 1.0E1, a peak duration range of 0.02 − 10 min, and a baseline level of 1.0E1. The duplicate peaks were filtered with m/z tolerance of 0.1 m/z (or 5 ppm) and a retention time tolerance of 2.0 min for the peak list. KEGG compound database (https://www.genome.jp/kegg/compound/) was used for metabolite identification of the individual peaks with m/z tolerance 0.1–0.3.

Inhibition studies with *Pf* and *Pv* clinical samples
The collection of clinical samples was carried out with the approval of the Institutional Ethics Committee (IEB)/ Institutional Review Board (IRB) (94/HEC/19; IEC:248/2019) from febrile patients who visited Ispat General Hospital, Rourkela, India, and KMC Hospital, Mangalore, India, after obtaining their informed consent. *Pf* and *Pv* infections were confirmed by examining Giemsa-stained thick and thin blood smears under the light microscope, and by performing rapid diagnostic test and PCR for *18 S rRNA*. The infected blood was collected in heparinized vacutainers and the subsequent procedures were carried out in BSL-2 facility under sterile conditions. The infected blood was centrifuged to remove the plasma and buffy coat, followed by two washes with RPMI-1640 medium containing 10% heat-inactivated human O⁺ serum. The packed cells were then resuspended in the same medium and the hematocrit was adjusted to 5%. The cultures were treated with different concentrations of MSO/PPT and ³H-hypoxanthine addition was carried out after 3 h of MSO/PPT addition to assess the parasite growth. The cultures were incubated following the standard conditions of *Pf* maintenance and the experiments were performed for each clinical isolate in RPMI⁻ᵍˡⁿ as well as in RPMI^Pgln. All these experiments were typically carried out in a final culture volume of 1.2 ml for the respective concentrations of MSO or PPT. Parasite growth assessment was also verified by examining the Giemsa-stained smears.

Ring-stage survival assays with ART-resistant *Pf*Cam3.I^R539T strain
*Pf*Cam3.I^R539T strain was maintained under standard conditions. When the parasitemia reached around 2% with predominant ring stages, the cultures were subjected to two rounds of tight synchronization within a span of 3 h in the previous cycle, followed by one additional synchronization in the subsequent cycle when they are in early rings. The parasitemia was adjusted to 0.5–1.0% in 2% hematocrit and ring-stage survival assays were carried out by the addition of 700 nM ART (Sigma-Aldrich, 361593) or DHA (Sigma-Aldrich, D7439)[84]. For the combination of ART with MSO/PPT and DHA with MSO/PPT, MSO or PPT was added along with ART/DHA. The exposure of rings to ART/DHA or ART/DHA in combination with MSO/PPT was precisely carried out for 6 h, followed by the removal of supernatant and washing the infected-RBCs twice with RPMI-1640 medium. The infected RBCs were then resuspended in RPMI-1640 medium and maintained continuously. The

medium change was carried out at 48 and 72 h, and after 96 h, the culture parasitemia was examined by Giemsa-stained smears and flow cytometry. For growth assessment by ^{3}H-hypoxanthine uptake, the label was added at 72 h and the cells were harvested at 96 h. The experiments were carried out independently in RPMI[-gln] and RPMI[Pgln] medium.

Other procedures

Western blot analyzes were carried out following the standard protocols and the blots were developed either with Pierce ECL Western blotting substrate (Thermo Fischer Scientific, 32209) for horse radish peroxidase or with 5-bromo-4-chloro-3-indolyl phosphate (MP Biomedicals, 215004283) and P-nitro blue tetrazolium chloride (MP Biomedicals, 210041690) for alkaline phosphatase. Rabbit polyclonal anti-GFP antibodies (Abcam, ab290) was used at 1:5000 dilution. The secondary antibodies - goat anti-mouse IgG H&L (HRP) (Abcam, ab97023) and goat anti-rabbit IgG H&L (HRP) (Abcam, ab97051) were used at 1:10,000 dilution, and goat anti-mouse IgG H&L (AP) (Abcam, ab97051) was used at 1:5,000 dilution. Subcellular fractionation of cytosol and membrane fraction was carried out by resuspending the *Pf*GS[cKS+Lyn] parasite pellet in 150 μl of 50 mM Tris pH 7.5 containing protease inhibitors, followed by incubation in ice for 20 min and centrifugation at 20,000 g. The supernatant (cytosol) was separated and the pellet (membrane fraction) was resuspended in the same buffer. Plasma samples from *Pb*-infected mice were collected at similar parasitemia on day 8 post-infection when the parasites were predominantly in trophozoite stages using heparin as an anticoagulant. Plasma ammonia levels were measured using an ammonia assay kit (Abcam, ab83360). Plasma ATP levels were quantified using Luminescent ATP detection kit (Abcam, ab113849). Glutathione assays with parasite pellets were carried out using Glutathione colorimetric detection kit (Thermo fisher Scientific, EIAGSHC). Polyclonal sera against r*Pf* and r*Pb* GS were raised using Freund's complete (Sigma-Aldrich, F5881) and incomplete (Sigma-Aldrich, F5506) adjuvants.

Statistical analyzes

GraphPad Prism Version 7.00 software was used to plot the graphs. Statistical analyzes were carried out using unpaired Welch's t-test (two-sided), two-way ANOVA, and log-rank (Mantel-Cox) test. Tukey test was performed for two-way ANOVA and multiple comparisons were corrected by statistical hypothesis testing. n.s - not significant, $*P < 0.05$, $**P < 0.01$, $***P < 0.001$. The non-linear regression fit for the inhibitor versus response curve was performed and R-squared values were calculated using GraphPad Prism 7.00.

Reporting summary

Further information on research design is available in the Nature Portfolio Reporting Summary linked to this article.

Data availability

Source data are provided with this paper. The raw files and extracted chromatograms of nucleotide mass spectrometry analyzes are available in figshare[85]. https://doi.org/10.6084/m9.figshare.23553822.v1. Reference proteomes of *Plasmodium falciparum* (UP000001450, Taxonomy: 36329; UP000030688, Taxonomy: 57266; UP000054282, Taxanomy: 57267; UP000054289, Taxonomy: 137071; UP000030673, Taxonomy: 5843; UP000019103, Taxonomy: 57270; UP000232684, Taxonomy: 5843) available at Uniprot (https://www.uniprot.org/) were used for proteomics analyzes. Proteomics data have been deposited to the ProteomeXchange Consortium via the PRIDE partner repository with the dataset identifier PXD032797. Structures of *Pf* (PDB ID: 6PEW), *St* (PDB ID: 1F1H), *Mt* (PDB ID: 2WGS) and *Hp* GS (PDB ID: 5ZLP) were accessed from RCSB Protein Data Bank (https://www.rcsb.org/). Source data are provided with this paper.

References

1. Gardner, M. J. et al. Genome sequence of the human malaria parasite *Plasmodium falciparum*. *Nature* **419**, 498–511 (2002).
2. Payne, S. H. & Loomis, W. F. Retention and loss of amino acid biosynthetic pathways based on analysis of whole-genome sequences. *Eukaryot. Cell.* **5**, 272–276 (2006).
3. Olszewski, K. L. & Llinás, M. Central carbon metabolism of *Plasmodium* parasites. *Mol. Biochem. Parasitol.* **175**, 95–103 (2011).
4. Krishnan, A. & Soldati-Favre, D. Amino acid metabolism in apicomplexan parasites. *Metabolites* **11**, 61 (2021).
5. Francis, S. E., Sullivan, D. J. Jr. & Goldberg, D. E. Hemoglobin metabolism in the malaria parasite *Plasmodium falciparum*. *Annu. Rev. Microbiol.* **51**, 97–123 (1997).
6. Babbitt, S. E. et al. *Plasmodium falciparum* responds to amino acid starvation by entering into a hibernatory state. *Proc. Natl Acad. Sci. USA* **109**, E3278–E3287 (2012).
7. Bannister, L. H. & Sherman, I. W. *Plasmodium*. In: Encyclopedia of Life Sciences (ELS) (John Wiley & Sons, Ltd: Chichester, 2009).
8. Nagaraj, V. A. et al. Asparagine requirement in *Plasmodium berghei* as a target to prevent malaria transmission and liver infections. *Nat. Commun.* **6**, 8775 (2015).
9. Graewe, S., Stanway, R. R., Rennenberg, A. & Heussler, V. T. Chronicle of a death foretold: *Plasmodium* liver stage parasites decide on the fate of the host cell. *FEMS Microbiol. Rev.* **36**, 111–130 (2012).
10. Cassera, M. B., Zhang, Y., Hazleton, K. Z. & Schramm, V. L. Purine and pyrimidine pathways as targets in *Plasmodium falciparum*. *Curr. Top. Med. Chem.* **11**, 2103–2115 (2011).
11. Frame, I. J., Deniskin, R., Arora, A. & Akabas, M. H. Purine import into malaria parasites as a target for antimalarial drug development. *Ann. N. Y. Acad. Sci.* **1342**, 19–28 (2015).
12. Ballut, L. et al. Active site coupling in *Plasmodium falciparum* GMP synthetase is triggered by domain rotation. *Nat. Commun.* **6**, 8930 (2015).
13. Gomes, P. S. et al. Targeting the hexosamine biosynthetic pathway prevents *Plasmodium* developmental cycle and disease pathology in vertebrate host. *Front. Microbiol.* **10**, 305 (2019).
14. MacRae, J. I. et al. Mitochondrial metabolism of sexual and asexual blood stages of the malaria parasite *Plasmodium falciparum*. *BMC Biol.* **11**, 67 (2013).
15. Cruzat, V., Macedo Rogero, M., Noel Keane, K., Curi, R. & Newsholme, P. Glutamine: metabolism and immune function, supplementation and clinical translation. *Nutrients* **10**, 1564 (2018).
16. Mack, S. R., Samuels, S. & Vanderberg, J. P. Hemolymph of *Anopheles stephensi* from uninfected and *Plasmodium berghei*-infected mosquitoes. 2. Free amino acids. *J. Parasitol.* **65**, 130–136 (1979).
17. PlasmoDB. Plasmodium Genomics Resource. https://plasmodb.org/plasmo/app.
18. Gill, H. S. & Eisenberg, D. The crystal structure of phosphinothricin in the active site of glutamine synthetase illuminates the mechanism of enzymatic inhibition. *Biochemistry* **40**, 1903–1912 (2001).
19. Janssen, P. J., Jones, W. A., Jones, D. T. & Woods, D. R. Molecular analysis and regulation of the glnA gene of the gram-positive anaerobe *Clostridium acetobutylicum*. *J. Bacteriol.* **170**, 400–408 (1988).
20. Liaw, S. H., Pan, C. & Eisenberg, D. Feedback inhibition of fully unadenylylated glutamine synthetase from *Salmonella typhimurium* by glycine, alanine, and serine. *Proc. Natl Acad. Sci. USA* **90**, 4996–5000 (1993).
21. Brown, J. R., Masuchi, Y., Robb, F. T. & Doolittle, W. F. Evolutionary relationships of bacterial and archaeal glutamine synthetase genes. *J. Mol. Evol.* **38**, 566–576 (1994).

22. Ho, C.-M. et al. Bottom-up structural proteomics: cryoEM of protein complexes enriched from the cellular milieu. *Nat. Methods* **17**, 79–85 (2020).

23. Krajewski, W. W., Jones, T. & Mowbray, S. L. Structure of *Mycobacterium tuberculosis* glutamine synthetase in complex with a transition-state mimic provides functional insights. *Proc. Natl Acad. Sci. USA* **102**, 10499–10504 (2005).

24. Mowbray, S. L., Kathiravan, M. K., Pandey, A. A. & Odell, L. R. Inhibition of glutamine synthetase: a potential drug target in *Mycobacterium tuberculosis*. *Molecules* **19**, 13161–13176 (2014).

25. Harth, G. & Horwitz, M. A. An inhibitor of exported *Mycobacterium tuberculosis* glutamine synthetase selectively blocks the growth of pathogenic mycobacteria in axenic culture and in human monocytes: Extracellular proteins as potential novel drug targets. *J. Exp. Med* **189**, 1425–1436 (1999).

26. Jeitner, T. M. & Cooper, A. J. L. Inhibition of human glutamine synthetase by L-methionine-S,R-sulfoximine - relevance to the treatment of neurological diseases. *Metab. Brain Dis.* **29**, 983–989 (2014).

27. Krajewski, W. W. et al. Crystal structures of mammalian glutamine synthetases illustrate substrate-induced conformational changes and provide opportunities for drug and herbicide design. *J. Mol. Biol.* **375**, 217–228 (2008).

28. Lea, P. J. & Ridley, M. Glutamine synthetase and its inhibition. *Soc. Exp. Biol. Semin. Ser.* **38**, 137–170 (1989).

29. Tian, Y.-S. et al. Identification of a phosphinothricin-resistant mutant of rice glutamine synthetase using DNA shuffling. *Sci. Rep.* **5**, 15495 (2015).

30. Franco, A. R., Lopez-Siles, F. J. & Cardenas, J. Resistance to Phosphinothricin (Glufosinate) and Its Utilization as a Nitrogen Source by *Chlamydomonas reinhardtii.Appl. Environ. Microbiol* **62**, 3834–3839 (1996).

31. Woolfolk, C. A. & Stadtman, E. R. Regulation of glutamine synthetase. III. Cumulative feedback inhibition of glutamine synthetase from *Escherichia coli. Arch. Biochem. Biophys.* **118**, 736–755 (1967).

32. Deuel, T. F. & Prusiner, S. Regulation of glutamine synthetase from *Bacillus subtilis* by divalent cations, feedback inhibitors, and L-glutamine. *J. Biol. Chem.* **249**, 257–264 (1974).

33. Tate, S. S. & Meister, A. Regulation of rat liver glutamine synthetase: activation by α-ketoglutarate and inhibition by glycine, alanine, and carbamyl phosphate. *Proc. Natl. Acad. Sci. USA* **68**, 781–785 (1971).

34. Joo, H. K., Park, Y. W., Jang, Y. Y. & Lee, J. Y. Structural Analysis of Glutamine Synthetase from *Helicobacter pylori. Sci. Rep.* **8**, 11657 (2018).

35. Okano, H., Hwa, T., Peter Lenz, P. & Yan, D. Reversible adenylylation of glutamine synthetase is dynamically counterbalanced during steady-state growth of *Escherichia coli. J. Mol. Biol.* **404**, 522–536 (2010).

36. Theron, A. et al. Differential inhibition of adenylylated and deadenylylated forms of *M. tuberculosis* glutamine synthetase as a drug discovery platform. *PLoS One* **12**, e0185068 (2017).

37. Birnbaum, J. et al. A genetic system to study *Plasmodium falciparum* protein function. *Nat. Methods* **14**, 450–456 (2017).

38. Armstrong, C. M. & Goldberg, D. E. An FKBP destabilization domain modulates protein levels in *Plasmodium falciparum. Nat. Methods* **4**, 1007–1009 (2007).

39. Riggle, B. A. et al. MRI demonstrates glutamine antagonist-mediated reversal of cerebral malaria pathology in mice. *Proc. Natl Acad. Sci. USA* **115**, E12024–E12033 (2018).

40. Kimoloi, S. & Rashid, K. Potential role of *Plasmodium falciparum*-derived ammonia in the pathogenesis of cerebral malaria. *Front. Neurosci.* **9**, 234 (2015).

41. Salles, É. M. et al. P2X7 receptor drives Th1 cell differentiation and controls the follicular helper T cell population to protect against *Plasmodium chabaudi* malaria. *PLoS Pathog.* **13**, e1006595 (2017).

42. Meins, F. Jr. & Abrams, M. L. How methionine and glutamine prevent inhibition of growth by methionine sulfoximine. *Biochim. Biophys. Acta* **266**, 307–311 (1972).

43. Peters, T. J., Jambekar, A. A. & Brusilow, W. S. A. In vitro suppression of inflammatory cytokine response by methionine sulfoximine. *J. Inflamm.* **15**, 17 (2018).

44. Takano, H. K., Beffa, R., Preston, C., Westra, P. & Dayan, F. E. Physiological factors affecting uptake and translocation of glufosinate. *J. Agric. Food Chem.* **68**, 3026–3032 (2020).

45. Muralidharan, V., Oksman, A., Iwamoto, M., Wandless, T. J. & Goldberg, D. E. Asparagine repeat function in a *Plasmodium falciparum* protein assessed via a regulatable fluorescent affinity tag. *Proc. Natl Acad. Sci. USA* **108**, 4411–4416 (2011).

46. Muralidharan, V. & Goldberg, D. E. Asparagine repeats in *Plasmodium falciparum* proteins: Good for Nothing? *PLoS Pathog.* **9**, e1003488 (2013).

47. Matz, J. M. et al. A lipocalin mediates unidirectional heme biomineralization in malaria parasites. *Proc. Natl Acad. Sci. USA* **117**, 16546–16556 (2020).

48. Nagaraj, V. A., Arumugam, R., Prasad, D., Rangarajan, P. N. & Padmanaban, G. Protoporphyrinogen IX oxidase from *Plasmodium falciparum* is anaerobic and is localized to the mitochondrion. *Mol. Biochem. Parasitol.* **174**, 44–52 (2010).

49. Prommana, P. et al. Inducible knockdown of *Plasmodium* gene expression using the glmS ribozyme. *PLoS One* **8**, e73783 (2013).

50. Mok, S. et al. Artemisinin-resistant K13 mutations rewire *Plasmodium falciparum*'s intra-erythrocytic metabolic program to enhance survival. *Nat. Commun.* **12**, 530 (2021).

51. Kumada, Y. et al. Evolution of the glutamine synthetase gene, one of the oldest existing and functioning genes. *Proc. Natl Acad. Sci. USA* **90**, 3009–3013 (1993).

52. Eisenberg, D., Gill, H. S., Pfluegl, G. M. & Rotstein, S. H. Structure-function relationships of glutamine synthetases. *Biochim. Biophys. Acta* **1477**, 122–145 (2000).

53. Krugliak, M., Zhang, J. & Ginsburg, H. Intraerythrocytic *Plasmodium falciparum* utilizes only a fraction of the amino acids derived from the digestion of host cell cytosol for the biosynthesis of its proteins. *Mol. Biochem. Parasitol.* **119**, 249–256 (2002).

54. Teng, R. et al. Metabolite profiling of the intraerythrocytic malaria parasite *Plasmodium falciparum* by ¹H NMR spectroscopy. *NMR Biomed.* **22**, 292–302 (2009).

55. Simon, A., Cobbold, S. A., Martin, R. E. & Kirk, K. Methionine transport in the malaria parasite. *Plasmodium falciparum. Int. J. Parasitol.* **41**, 125–135 (2011).

56. Dalal, S. & Klemba, M. Amino acid efflux by asexual blood-stage *Plasmodium falciparum* and its utility in interrogating the kinetics of hemoglobin endocytosis and catabolism in vivo. *Mol. Biochem. Parasitol.* **201**, 116–122 (2015).

57. Ke, H. et al. Genetic investigation of tricarboxylic acid metabolism during the *Plasmodium falciparum* life cycle. *Cell Rep.* **11**, 164–174 (2015).

58. Steiner, T. M. et al. Substrate usage determines carbon flux via the citrate cycle in *Helicobacter pylori. Mol. Microbiol.* **116**, 841–860 (2021).

59. Tintó-Font, E. et al. A heat-shock response regulated by the PfAP2-HS transcription factor protects human malaria parasites from febrile temperatures. *Nat. Microbiol.* **9**, 1163–1174 (2021).

60. Bushell, E. et al. Functional profiling of a *Plasmodium* genome reveals an abundance of essential genes. *Cell* **170**, 260–272 (2017).

61. Stanway, R. R. et al. Genome-scale identification of essential metabolic processes for targeting the *Plasmodium* liver stage. *Cell* **179**, 1112–1128 (2019).

62. Kudyba, H. M., Cobb, D. W., Vega-Rodríguez, J. & Muralidharan, V. Some conditions apply: Systems for studying *Plasmodium falciparum* protein function. *PLoS Pathog.* **17**, e1009442 (2021).

63. Bunditvorapoom, D. et al. Fitness loss under amino acid starvation in artemisinin-resistant *Plasmodium falciparum* isolates from Cambodia. *Sci. Rep.* **8**, 12622 (2018).

64. Nair, S. et al. Nutrient limitation magnifies fitness costs of antimalarial drug resistance mutations. *Antimicrob. Agents Chemother.* **66**, e01529–21 (2022).

65. Kim, G. W. et al. Glutamine synthetase as a therapeutic target for cancer treatment. *Int. J. Mol. Sci.* **22**, 1701 (2021).

66. Zhu, W. et al. High-resolution crystal structure of human asparagine synthetase enables analysis of inhibitor binding and selectivity. *Commun. Biol.* **2**, 345 (2019).

67. van der Pluijm, R. W., Amaratunga, C., Dhorda, M. & Dondorp, A. M. Triple artemisinin-based combination therapies for malaria - a new paradigm? *Trends Parasitol.* **37**, 15–24 (2021).

68. Gawronski, J. D. & Benson, D. R. Microtiter assay for glutamine synthetase biosynthetic activity using inorganic phosphate detection. *Anal. Biochem.* **327**, 114–118 (2004).

69. Gonzalez-Romo, P., Sanchez-Niet, S. & Gavilanes-Ruiz, M. A modified colorimetric method for the determination of orthophosphate in the presence of high ATP concentrations. *Anal. Biochem.* **200**, 235–238 (1992).

70. Agilent Biocolumns Application Compendium- Amino Acid Analysis. https://www.agilent.com/cs/library/applications/compendium-%20aminoacid-advancebio-5994-0033EN-us-agilent.pdf (2021).

71. Kerby, N. W. & Vincent, W. F. Development of a field assay for glutamine synthetase, the primary ammonium-assimilating enzyme of cyanobacteria. *N. Z. J. Mar. Freshw. Res.* **21**, 535–536 (1987).

72. Hopfner, D. et al. Monoclonal anti-AMP antibodies are sensitive and valuable tools for detecting patterns of AMPylation. *iScience* **23**, 101800 (2020).

73. Nagaraj, V. A. et al. Malaria parasite-synthesized heme is essential in the mosquito and liver stages and complements host heme in the blood stages of infection. *PLoS Pathog.* **9**, e1003522 (2013).

74. Desjardins, R. E., Canfield, C. J., Haynes, J. D. & Chulay, J. D. Quantitative assessment of antimalarial activity in vitro by a semi-automated microdilution technique. *Antimicrob. Agents Chemother.* **16**, 710–718 (1979).

75. Saliba, K. S. & Jacobs-Lorena, M. Production of *Plasmodium falciparum* gametocytes in vitro. *Methods Mol. Biol.* **923**, 17–25 (2013).

76. Chandana, M. et al. Malaria parasite heme biosynthesis promotes and griseofulvin protects against cerebral malaria in mice. *Nat. Commun.* **13**, 4028 (2022).

77. Tonkin, C. J. et al. Localization of organellar proteins in *Plasmodium falciparum* using a novel set of transfection vectors and a new immunofluorescence fixation method. *Mol. Biochem. Parasitol.* **137**, 13–21 (2004).

78. Itsara, L. S. et al. PfCap380 as a marker for *Plasmodium falciparum* oocyst development in vivo and in vitro. *Malar. J.* **17**, 135 (2018).

79. Mendes, A. M. et al. Inhibition of *Plasmodium* liver infection by ivermectin. *Antimicrob. Agents Chemother.* **61**, e02005–e02016 (2017).

80. Armenta, J. M. et al. A sensitive and rapid method for amino acid quantitation in malaria biological samples using AccQ•Tag UPLC-ESI-MS/MS with multiple reaction monitoring. *Anal. Chem.* **82**, 548–558 (2010).

81. Laourdakis, C. D., Merino, E. F., Neilson, A. P. & Cassera, M. B. Comprehensive quantitative analysis of purines and pyrimidines in the human malaria parasite using ion-pairing ultra-performance liquid chromatography-mass spectrometry. *J. Chromatogr. B Anal. Technol. Biomed. Life Sci.* **967**, 127–133 (2014).

82. Straube, H., Niehaus, M., Zwittian, S., Witte, C.-P. & Herde, M. Enhanced nucleotide analysis enables the quantification of deoxynucleotides in plants and algae revealing connections between nucleoside and deoxynucleoside metabolism. *Plant Cell* **33**, 270–289 (2021).

83. He, L. et al. Simultaneous quantification of nucleosides and nucleotides from biological samples. *J. Am. Soc. Mass. Spectrom.* **30**, 987–1000 (2019).

84. Witkowski, B. et al. Novel phenotypic assays for the detection of artemisinin resistant *Plasmodium falciparum* malaria in Cambodia: in-vitro and ex-vivo drug response studies. *Lancet Infect. Dis.* **13**, 1043–1049 (2013).

85. Nagaraj, V. A. Nucleotide analyses of control and MSO-treated *Plasmodium falciparum* cultures. *figshare* https://doi.org/10.6084/m9.figshare.23553822.v1 (2023).

Author contributions

S.G., R.K., M.Chandana, R.D., A.A., S.B., R.C.B., S.R.P., A.R.S., and V.A.N. performed the experiments. V.J. and A.D. performed GS modeling and MD simulation studies. S.G., P.K.B., A.K.M., S.R.P., M.Chakrapani, and K.S. collected clinical samples. S.G., R.K., M.Chandana, A.A., A.R.S., A.D., G.P., and V.A.N. analyzed the data. S.G., A.D., G.P., and V.A.N. wrote the manuscript. V.A.N. conceived and designed the study.

Competing interests

The authors declare no competing interests.

Additional information